Runoff, discharge and flood occurrence in a poorly gauged tropical basin

The Mahakam River, Kalimantan

Hidayat

Thesis committee

Promotor
Prof. Dr R. Uijlenhoet
Professor of Hydrology and Quantitative Water Management
Wageningen University

Co-promotor
Dr A.J.F. Hoitink
Associate professor, Hydrology and Quantitative Water Management Group
Wageningen University

Other members
Prof. Dr A.K. Bregt, Wageningen University
Prof. Dr P. Molnar, ETH Zurich, Switzerland
Prof. Dr A. Montanari, University of Bologna, Italy
Prof. Dr S. Uhlenbrook, UNESCO-IHE, Delft, The Netherlands

This research was conducted under the auspices of the SENSE Research School.

Runoff, discharge and flood occurrence in a poorly gauged tropical basin

The Mahakam River, Kalimantan

Hidayat

Thesis

submitted in fulfillment of the requirements for the degree of doctor
at Wageningen University
by the authority of the Rector Magnificus
Prof. Dr M.J. Kropff, in the presence of the
Thesis Committee appointed by the Academic Board
to be defended in public
on Wednesday 23 October 2013
at 4 p.m. in the Aula.

Hidayat
Runoff, discharge and flood occurrence in a poorly gauged tropical basin - The Mahakam River, Kalimantan, xviii+114 pages

Thesis, Wageningen University, Wageningen, NL (2013)
With references, with summaries in English and Bahasa Indonesia

ISBN 978-94-6173-743-4

Abstract

Tidal rivers and lowland wetlands present a transition region where the interests of hydrologists and physical oceanographers overlap. Physical oceanographers tend to simplify river hydrology, by often assuming a constant river discharge when studying estuarine dynamics. Hydrologists, in turn, generally ignore the direct or indirect effects of tides in water level and discharge records. This thesis aims to improve methods to monitor, model and predict discharge dynamics in tidal rivers and lowland wetlands, by focussing on the central and lower reaches of the River Mahakam (East Kalimantan, Indonesia), and the surrounding lakes area. The 980-km long river drains an area of about 77100 km^2 between 2°N - 1°S and 113°E - 118°E. Due to its very mild bottom slope, a significant tidal influence occurs in this river. The middle reach of the river is located in a subsiding basin, parts of which are below mean sealevel, featuring peat swamps and about thirty lakes connected to the river via tie channels.

Upstream of the lakes area, at about 300 km from the river mouth, an acoustic Doppler current profiler (H-ADCP) has been horizontally deployed at a station near the city of Melak (Chapter 2). The H-ADCP profiles of velocity are converted to discharge adopting a new calibration methodology. The obtained time-series of discharge show the tidal signal is clearly visible during low flow conditions. Besides tidal signatures, the discharge series show influences by variable backwater effects from the lakes, tributaries and floodplain ponds. The discharge rate at the station exceeds 3250 m^{3}s^{-1} with a hysteretic behaviour. For a specific river stage, the discharge range can be as high as 2000 m^{3}s^{-1}. Analysis of alternative types of rating curves shows this is far beyond what can be explained from kinematic wave dynamics. Apart from backwater effects, the large variation of discharge for a specified river stage can be explained by river-tide interaction, impacting discharge variation especially in the fortnightly frequency band.

A second H-ADCP station has been setup in the lower reach of the Mahakam, near the city of Samarinda, where the tidal discharge amplitude generally exceeds the discharge related to runoff (Chapter 3). Conventional rating curve techniques are inappropriate to model river discharge at this tidally influenced station. As an alternative, an artificial neural network (ANN) model is developed to investigate the degree to which tidal river discharge at Samarinda station can be predicted from an array of level gauge measurements along the tidal river, and from tidal level predictions at sea. The ANN-based model produces a good discharge estimation, as established from a consistent performance during both the training and the validation periods, showing the discharges can be predicted from water levels only, once that a trained model is available. The ANN models perform well in predicting discharges up to two days in advance.

Chapter 4 addresses the role of backwater effects and tidal influences on discharge time-series used to calibrate a rainfall-runoff model. The HBV rainfall-runoff model is implemented for the Mahakam sub-catchment upstream of Melak (25700 km^2). In a first approach, the model is calibrated using a discharge series derived from the H-ADCP measurements from Melak station. In a second approach, discharge estimates derived from a rating curve are used to calibrate the model. Adopting the first approach, a comparatively low model efficiency is obtained, which is attributed to the backwater and tidal effects that are not captured in the model. The second approach produces a relatively higher model efficiency, since the rating

curve filters the backwater effects out of the discharge series. Seasonal variation of terms in the water balance is not affected by the choice for one of the two calibration strategies, which shows that backwaters do not have a systematic seasonal effect on the river discharge.

To allow for investigation of the causes of backwater effects, satellite radar remote sensing is employed to monitor water levels in wetlands (Chapter 5). A series of Phased Array L-band Synthetic Aperture Radar (PALSAR) images is used to observe the dynamics of the Mahakam River floodplain. To analyze radar backscatter behavior for different land cover types, several regions of interest are selected, based on land cover classes. Medium shrub, high shrub, fern/grass, and degraded forest are found to be sensitive to flooding, whereas peat forest, riverine forest and tree plantation backscatter signatures only slightly change with flood inundation. An analysis of the relationship between radar backscatter and water levels is carried out. For lakes and shrub covered peatland, for which the range of water level variation is high, a good water level-backscatter correlation is obtained. In peat forest covered peatland, subject to a small range of water level variation, water level-backscatter correlations are poor, limiting the ability to obtain a floodplain-wide water surface topography from the radar images.

Chapter 6 continues to investigate the degree in which satellite radar remote sensing can serve to distinguish between dry areas and wetlands, which is a difficult task in densely vegetated areas such as peat domes. Flood extent and flood occurrence information are successfully extracted from a series of radar images of the middle Mahakam lowland area. A fully inundated region is easily recognized from a dark signature on radar images. Open water flood occurrence is mapped using a threshold value taken from radar backscatter of the permanently inundated areas. Radar backscatter intensity analysis of the vegetated floodplain area reveals consistently higher backscatter values, indicating flood inundation under forest canopy. Those observations are used to establish thresholds for flood occurrence mapping in the vegetated area. An all-encompassing flood occurrence map is obtained by combining the flood occurrence maps for areas with and without vegetation.

Chapter 7 synthesizes the findings from the previous chapters. It is concluded that the backwater effects and subtle tidal influences may prevent the option to predict river discharge using rating curves, which can best be interpreted as a stage-runoff relationship. H-ADCPs offer a promising alternative to monitor river discharge. For a tidal river, an ANN model can be used as a tool for data gap filling in an H-ADCP based discharge series, or even to derive discharge estimates solely from water levels and water level predictions. Discharge can be predicted several time-steps ahead, allowing water managers to take measures based on forecasts. The stage-runoff relationship derived from a continuous series of H-ADCP based discharge estimates may be expected to be much more accurate than a similar rating curve derived from a small number of boat surveys. The flood occurrence map derived from PALSAR images can offer a detailed insight into the hydroperiod, the period in which a soil area is waterlogged, and flood extent of the lowland area, illustrating the added value of radar remote sensing to wetland hydrological studies. In future work, radar-based floodplain observations may serve to calibrate hydrodynamic models simulating the processes of flooding and emptying of the lakes area.

Contents

List of Figures

List of Tables

Chapter 1

General Introduction

1.1 Motivation

Tidal rivers and lowland wetlands present regions under the influence of both catchment hydrological processes and forcing conditions imposed by the ocean. Figure 1 presents a global elevation map that highlights regions located less than 10 m above mean sea level in red, pointing to the low elevation coastal zones where tidal effects may occur. In general, these regions coincide with densely populated areas where economic activity is concentrated. Regions upstream of the limit of salinity intrusion, beyond the estuarine part of a coastal lowland but still under the influence of the tidal motion and mean sealevel variation, have received relatively little attention in the literature. The extent of these regions can be considerable, since the length of tidal intrusion may reach up to an order of magnitude further than that of salinity intrusion. Hydrologists rarely recognize the effect of tides and storm surges in streamflow records. They tend to employ rating curves in lowlands in which the tidal influence is apparent as a source of error. In physical oceanography, in turn, little attention is paid to the effect of tides on rivers and inland wetlands. The oceanographic scope rarely reaches inland from the estuarine part of a coastal lowland, and existing studies on river tides often simply assume a constant river discharge. Tidal rivers and lowland wetlands present a transition region where the joint effort of hydrologists and physical oceanographers potentially may reveal new insights.

This thesis aims to improve methods to monitor, model and predict discharge dynamics and flood occurrence in tidal rivers and lowland wetlands, by focussing on the central and lower reaches of the River Mahakam (East Kalimantan, Indonesia). The 980-km long river drains an area of about 77100 km^2 between 2°N - 1°S and 113°E - 118°E. Due to its very mild bottom slope, a significant tidal influence occurs in this river (Allen et al., 1977). The middle reach of the river is located in a subsiding basin, parts of which are below mean sealevel, featuring peat swamps and about thirty lakes connected to the river via tie channels (Fig 1.2). The middle and lower Mahakam areas provide a unique geographical setting to test methods in studying the hydrology of lowland rivers in a humid tropical environment. The study presented in this thesis is a combination of a relatively short but intensive field campaign and satellite remote sensing.

This introduction continues to describe the thematic background in Section 1.2, introducing tropical hydrology, rainfall-runoff modeling, hydraulics of lowland wetlands and flood monitoring using radar. Section 1.3 then offers an introduction to the field site and Section 1.4 specifies

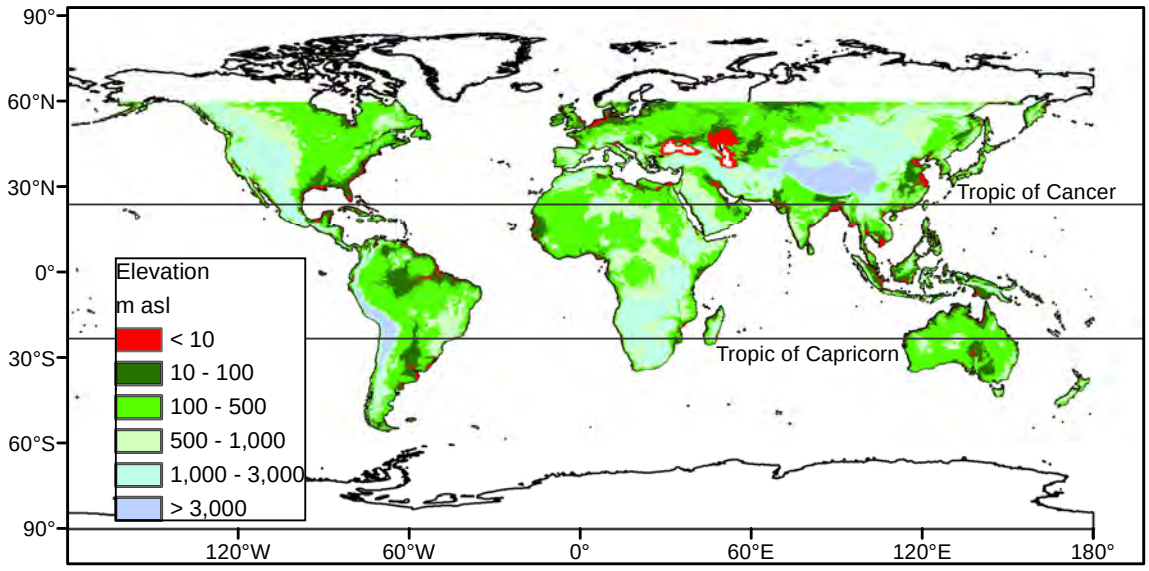

Figure 1.1: World map highlighting the tropical region and elevation from Shuttle Radar Topographic Mission (SRTM) data. Data source: CGIAR-CSI. The elevation is sub-divided into five categories: coastal plain (<100 m), lowland (100-500 m), highland (500-1000 m), mountain (1000-3000 m) and high mountain (>3000 m) based on the river basin classification of Milliman and Syvitski (1992). The elevation of <10 m is added to show areas, where the inland rivers are likely to be affected by tidal influences.

the research questions. Section 1.5 elaborates on the methods adopted in this study, and Section 1.6 gives an overview of the remainder of this thesis.

1.2 Thematic background

1.2.1 Tropical hydrology

Geographically, the tropical regions are roughly bounded by the Tropics of Cancer and Capricorn at a latitude of 23° 27' North and South (Fig 1.1). Over this region, temperature has a consistent variation from day to night and throughout the seasons (Latrubesse et al., 2005). One of the important features of the tropics that determines the seasons is rainfall. The rainfall pattern in this region is largely determined by large-scale atmospheric wind patterns, known as the Hadley circulation (Seidel et al., 2008). The Hadley Cell involves air rising in equatorial regions, flowing toward the North and South Poles, returning to the surface of the Earth at the edges of the tropical belts, and flowing back toward the equator at the surface of the Earth. The ascending branch of the Hadley circulation carries moisture into the air, promoting rainfall, whereas the descending branches are drier. Within this circulation, evaporation is intensively concentrated around the equator along the Inter Tropical Convergence Zone (ITCZ), characterized by accumulation of clouds in the area. The ITCZ, that moves up and down following the pseudo-motion of the Sun within the zone between the Tropics of Cancer and Capricorn,

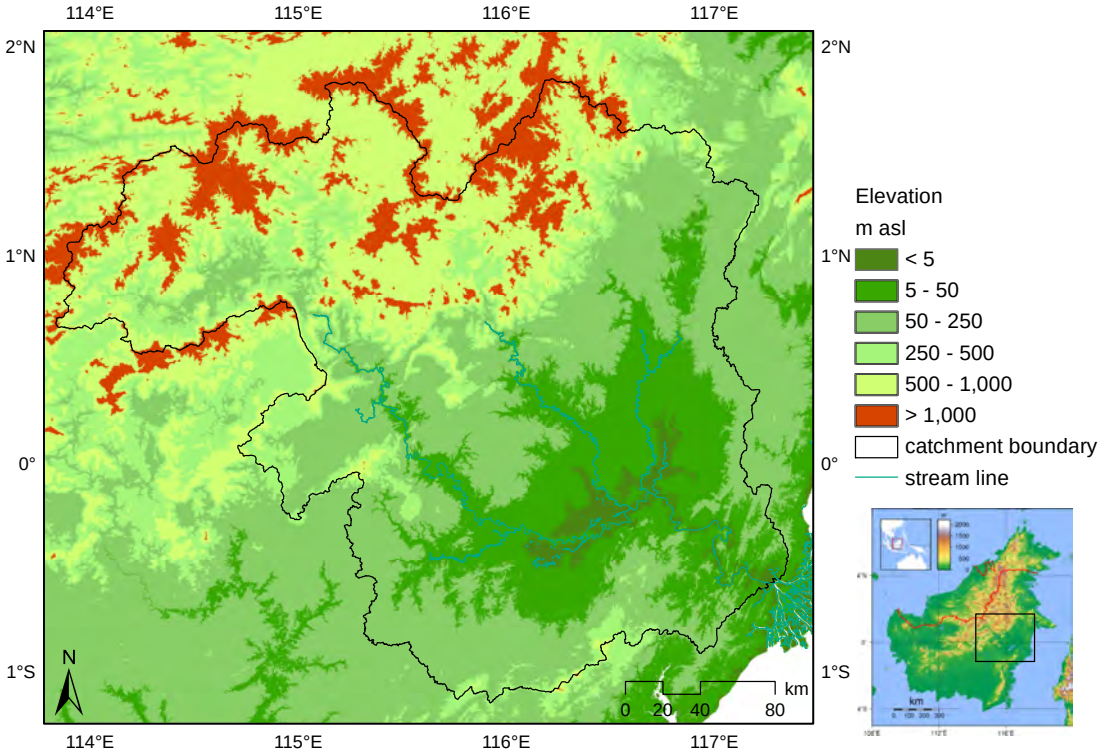

Figure 1.2: Digital elevation map of the Mahakam catchment from SRTM data.

drives the Indo-Australian monsoon, which influences the tropical regional climate particularly in Indonesia, and South-East Asia in general.

Another large-scale phenomenon that is related to inter-annual variations in precipitation in the region is the coupled ocean-atmosphere oscillation in the Pacific Ocean, known as the El Niño-Southern Oscillation (ENSO). ENSO events, which are associated with a disturbance of the Walker circulation over the equatorial Pacific Ocean (Ward et al., 2010), spread through the entire tropical belt and influence the global climate on time scales of years to decades (Amarasekera et al., 1997). The warm El Niño phase is characterized by elevated temperatures throughout the tropics. During this phase, warming of surface waters in the central and eastern equatorial Pacific occurs, causing enhanced convection and rainfall in this region, while the western Pacific is relatively cool, leading to reduced convection and drier conditions over Indonesia and Australia (Ward et al., 2010). Conversely, La Niña events are episodes of suppressed temperatures throughout the tropics. During this phase, heavy rains are generally intensified over the Indonesian archipelago. River systems may act as comprehensive integrators of precipitation over well-defined catchments. Better characterization of river discharge patterns can lead to an increased understanding of regional and global atmospheric dynamics (Amarasekera et al., 1997). Since the catchment areas of major rivers are quite extensive, river discharge is a useful index of the precipitation characteristics over areas where extensive direct measurements of rainfall are impractical. Therefore, taking discharge measurements will not only promote the understanding of the land phase of the hydrological cycle, but may also benefit that of the atmospheric phase.

Rivers draining tropical rainforests generally have high but variable peak discharges during the rainy season and a period of low flow when rainfall decreases (Latrubesse et al., 2005). Their discharge patterns usually follow the rainfall depths over the catchments with time lags. Therefore, tropical river regimes are also generally affected by the recurrence of ENSO with different effects across the region. Amarasekera et al. (1997) found that annual discharge of the Amazon and Congo Rivers are respectively weakly and negatively correlated with the equatorial Pacific sea surface temperature anomalies, one of the ENSO indices, whilst river discharge in the Parana basin shows a positive relation.

1.2.2 Rainfall-runoff modeling

Rainfall-runoff models have been extensively used in hydrological studies. Milestones of the model development were initiated by the elaboration of the rational method by Mulvany in 1850 (Stephenson, 1981), the introduction of the unit hydrograph concept on direct runoff response to rainfall excess by Sherman in 1932 (Jakeman and Kokkonen, 2001), the development of the stream flow generation concept by Horton in 1945 (Beven, 2004), the introduction of the instantaneous unit hydrograph theory by Nash in 1957 and the development of kinematic wave theory for flow routing by Lighthill and Whitham in 1955 (Singh and Woolhiser, 2002). The digital revolution in 1960s accelerated the model development by enabling catchment-scale integration of models of different components of the hydrologic cycle, using lumped, semi-distributed, or distributed hydrological models.

Building hydrological models in poorly gauged, or ungauged basins is a timely challenge, since the number of permanent gauge locations is declining worldwide (Vörösmarty, 2002). Over the past decade, modelling approaches based on existing and new theories and datasets have been developed under the International Association of Hydrological Sciences' initiative 'Prediction in Ungauged Basins' (PUB) (Sivapalan et al., 2003). Runoff prediction in ungauged basins is generally based on different data acquisition strategies, from global/regional data sets to local data sources including field observations of local system characteristics. While global or regional data are useful for annual runoff prediction, more intensive local data are needed for hydrograph prediction (McGlynn et al., 2013). For the purpose of PUB, the measurement of discharge is the most direct way of gaining insight into the hydrologic behaviour of catchments, combined with insights from a calibrated rainfall-runoff model using the obtained discharge data. The establishment of focus drainage basins that cover a wide range of scales and climatic conditions, and that contain state-of-the-art instrumentation to measure a wide variety of variables required to characterize the hydrologic system is crucial in the modeling focus of PUB (Wagener et al., 2004a). Generally, runoff prediction in ungauged basins is based on different data acquisition strategies, ranging from global data sets of typically low resolution to local and regional data sources of varying availability and accuracy, followed by field observations of local system characteristics. While global or regional data are useful for annual runoff prediction, more intensive local data are needed for hydrograph prediction (McGlynn et al., 2013).

1.2.3 Hydraulics of lowland wetlands

Lowland regions are characterized by specific properties, such as a flat topography, small hydraulic gradients, shallow groundwater, and a high potential for water retention in wetlands

(Schmalz et al., 2008). Shallow groundwater conditions in these areas results in intensive groundwater-stream water interactions. In a study using a semi-distributed hydrological model in a rural lowland catchment, Schmalz et al. (2008) found that the dominating hydrological processes are mainly controlled by groundwater dynamics and storage, drainage, wetlands and ponds.

The hydraulics of lowland regions is complicated by, among others, backwater effects, lake-river interaction and possible tidal effects. Backwater effects cause a non-unique stage-discharge relation (Petersen-Overleir and Reitan, 2009; Herschy, 2009), i.e. falling river stages to be much higher than rising stages at any given discharge. As will be discussed later on in the subsequent chapters of this thesis, lake filling and emptying mechanisms also affect stages and discharges upstream. In lowland regions, tides have a significant impact on the river flow farther away from the river mouth, which is caused by subtidal water level variations controlled by river-tide interactions (Buschman et al., 2009). Consequently, without a proper adaptation, hydrological tools such as rating curves, rainfall-runoff models and flood prediction may fail to produce adequate results. Novel measurement techniques and modelling approaches such as continuous flow measurements (Sassi et al., 2011; Hoitink et al., 2009) and neural networks (Corzo et al., 2009) can be a possible means of coping with the complex interactions of runoff, tides, peat areas, and lakes in lowland regions.

Wetlands, including lakes, swamps, and peatlands are typical landscapes of a lowland region. Natural tropical peatlands play an important ecological role and are important reservoirs of biodiversity, carbon and water (Wösten et al., 2006a). Rivers draining from tropical peatlands and peat swamp forests are home to fish, reptile, bird, and mammalian fauna, including those listed as endangered species (Wösten et al., 2006b). In terms of carbon sink functioning, Jaenicke et al. (2008) estimated that at least 5510 Gt of carbon are stored in Indonesia's peatlands. However, changes in the hydrological regime might turn this carbon sink into a source. Tropical peatlands have a high porosity and a high water-holding capacity, due to the low bulk density of most of the peat that provides them with an important water regulation function with respect to the downstream lowlands. Under natural conditions, tropical peatlands serve as reservoirs of fresh water. They moderate water levels, reduce storm-flows, level down peak discharges and prevent low flow events, and buffer against saltwater intrusion (Wösten et al., 2008).

Hydrology is often the most poorly described aspect of any wetland due to cost, time, and technical constraints of field measurements in this area (Cole et al., 1997). Subsequently, determining an average or characteristic hydroperiod, i.e. the period in which a soil area is waterlogged, a major technical challenge for wetland sites remains. In studies at the plot scale, piezometers are commonly used to analyze water levels in peatlands, which are labor intensive to maintain (Devito et al., 1996; Baird et al., 2004; Fraser et al., 2001). One approach to address this scarcity of information is the application of satellite remote sensing techniques.

1.2.4 Radar technology in flood mapping

Flood maps are an important source of input for integrated assessment of flood dynamics, ecological processes, and vulnerability required in planning, designing, and operating flood works, nature reserves, and land management policies (Qi et al., 2009). Regular acquisition of

remotely sensed inundation extents allows for mapping flood occurrences over a large area. In areas with less cloud cover, data from optical sensors such as Landsat imagery can be used for this purpose (e.g. Qi et al., 2009; Ran and Lu, 2012). Ran and Lu (2012) noted that images with a cloud cover of less than 5 % are preferred. However, for the humid tropics, the preferred limit of cloud cover is hard or even impossible to be satisfied.

Radar imagery is useful for the identification, mapping, and measurement of streams, lakes, and wetlands in humid tropical areas, as it is unconstrained by cloud cover (Romshoo, 2006; Henderson and Lewis, 2008; Hoekman, 2009). Most surface water features are detectable on radar imagery because of the contrast in returns between the smooth water surface and the rough land surface (Lewis, 1998). The advantages of using space-borne radar in environmental monitoring in these areas are that radar measurements can remotely acquire data in poorly accessible areas with 24 h per day functioning, and to a certain extent, that radar can penetrate vegetation cover. The latter functionality allows to observe flooding under a closed forest canopy. Detection of flooded forest is enabled by the bright appearance of the inundated forest on radar images as a result of double bounce reflections between water surfaces and tree trunks or branches (Hess et al., 1990).

The Phased Array L-band Synthetic Aperture Radar (PALSAR) is one of the remote sensing instruments onboard of the Advanced Land Observing Satellite (ALOS). PALSAR is a polarimetric instrument operating at a wavelength of 23.6 cm with a 46-day satellite cycle period for global environmental monitoring (Rosenqvist et al., 2007). The modes of observation include Fine Beam Single Polarization (FBS), Fine Beam Dual Polarization (FBD), Polarimetric (POL), and ScanSAR (Fig. 1.3). FBS and FBD are designed for land cover changes and forest monitoring. POL is dedicated to research related to polarimetry and polarimetric interferometry. ScanSAR is intended for seasonal phenomena studies, such as inundation extent monitoring and rice-field mapping. All land areas on the globe are covered at least once every year by the FBS, FBD, and ScanSAR modes. The typical repetition frequency for most areas is three to five times per year (Rosenqvist et al., 2007). In the last part of this thesis, Chapters 4 and 5, the PALSAR time series will play a central role.

1.3 Study area

This thesis is based on observations that were carried out in the Mahakam river basin (Fig. 1.2), in East Kalimantan, Indonesia. The river originates from the Cemaru (1680 m) in the center of Kalimantan, flows south-eastwards through the pre-tertiary rocks, reaches the tertiary basin of Kutai and then meets the River Kedang Pahu in the middle Mahakam area (van Bemmelen, 1949). From there on, the river meanders eastward through quarternary alluvium in the Mahakam lakes region. This area is an extremely flat tropical lowland area surrounded by peatlands. Some forty shallow lakes are located in this area and are connected to the Mahakam through small channels. During high flows, vast areas in the Mahakam lakes region are inundated. Downstream of the lakes region, the Mahakam meets three other main tributaries (River Belayan, Kedang Kepala, and Kedang Rantau) and flows south-eastward through the Mahakam delta distributaries towards the Makassar Strait (see Fig. 1.2).

Due to its very mild bottom slope, the river system is not only influenced by runoff, but also by marine conditions that can propagate farther away from the estuarine environment.

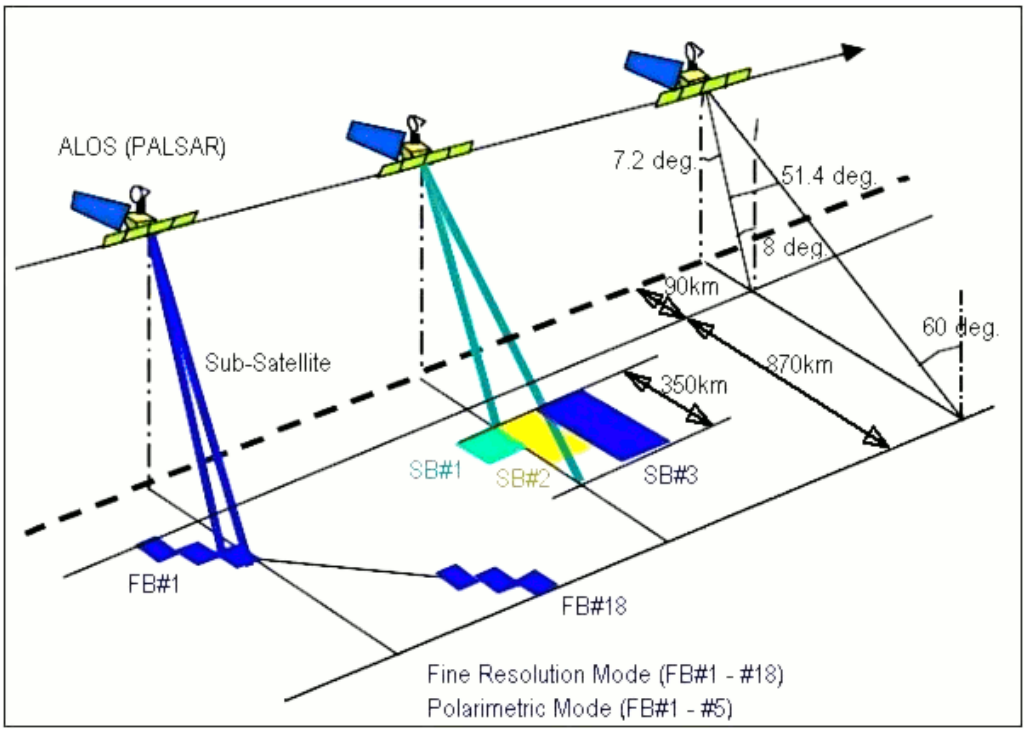

Figure 1.3: PALSAR observation characteristics (FB: fine resolution beam, SB: ScanSAR beam; image credit: Japan Aerospace Exploration Agency).

At the first glance, tides may seem a periodic perturbation of the river flow. However, the interactions of tides with the river flow are not all periodic (Buschman et al., 2009). River-tide interaction drives the co-oscillation of the subtidal (averaged over a diurnal period) water level with varying tidal amplitudes. The tidal regime in the River Mahakam is mixed mainly semidiurnal (Hoitink, 2008). Therefore, the spring-neap cycle has contributions due to tropical (about 27,13 days) and synodic (about 29.53 days) months, complicating the periodicities in the tidal amplitudes. River-tide interaction controls the admittance of river discharge waves into the downstream reaches of the River Mahakam since the subtidal water level is driven by a combination of river discharge and river-tide interaction (Sassi and Hoitink, 2013). The intensity of river-tide interaction depends non-linearly on the magnitude of river flow, which results from the dynamical interplay between climatic forcing and topography in the upstream areas.

According to the Köppen-Geiger climate classification, the catchment area belongs to type Af (tropical rain forest) that has a minimum temperature of 18°C and precipitation of the driest month in normal years exceeding 60 mm (Peel et al., 2007). The Indo-Australian monsoon driven by the ITCZ and ENSO phenomena influence the regional climate of Kalimantan (Meehl and Arblaster, 1998; Seidel et al., 2008). In December through February, the concentration of high pressure in Asia and low pressure in Australia causes Westerly winds in Indonesia (West monsoon). In June through August, the concentration of low pressure in Asia and high pressure in Australia causes Easterly winds in Indonesia (East monsoon). Due to the global circulation and the regional climate, the central and northern parts of Kalimantan, in which the Mahakam

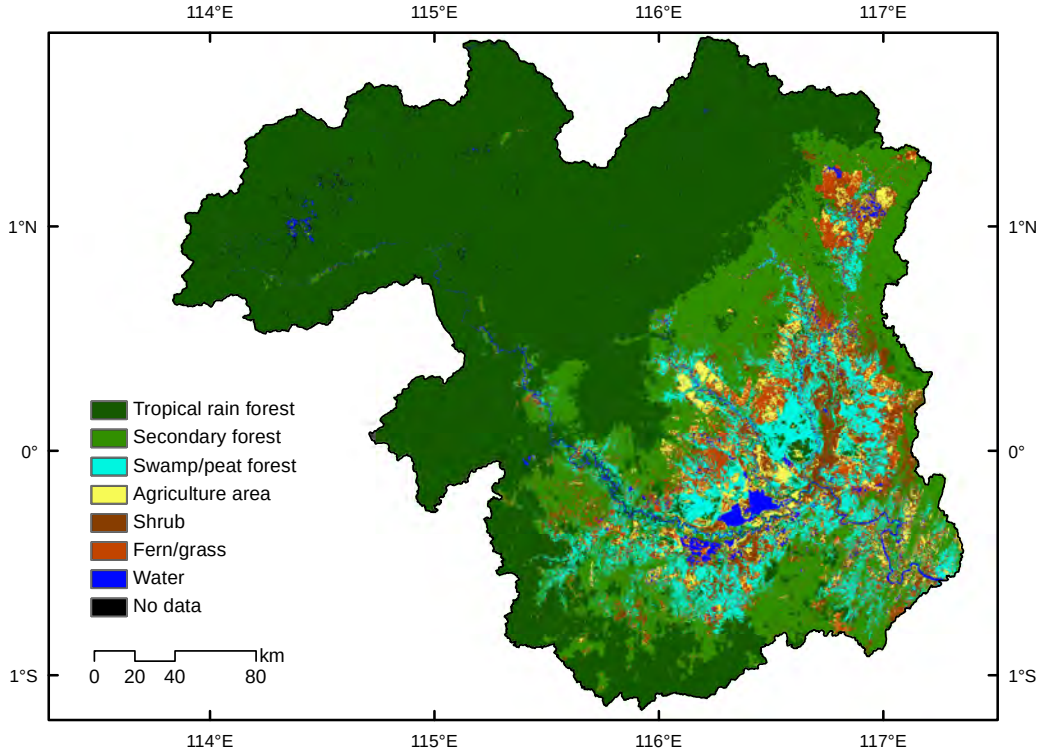

Figure 1.4: Land cover of the Mahakam catchment (reclassified from the Hoekman et al. (2010) land cover map of Borneo).

catchment is situated, has a bimodal rainfall pattern with two peaks of rainfall. Those peaks generally occur in October through November and March through April (Aldrian and Susanto, 2003).

Land cover of the Mahakam catchment comprises 56% tropical rain forest, 20% degraded forest, 8% swamp and peat forest, 8% shrub, 3% fern and grass, and 3% agriculture area (Fig. 5.2; recalculated from the land cover map of Borneo by Hoekman et al. (2010)). Land cover changes to agricultural area have mainly occurred since the 1970s, when the Indonesian government program on transmigration started. Forest fires also cause land cover changes in the catchment. Chokkalingam et al. (2005) found that 72-85% of the middle Mahakam peatlands were burned between 1997 and 2000. Within this period, fires mostly occurred during the 1997/1998 El Niño-induced extreme dry period. Other causes of land cover changes that were observed during the field campaign were open coal mining and land clearing for plantation.

The Mahakam River runs to the Makassar Strait through Samarinda, the capital of the province with 610,000 inhabitants in 2009, and the Mahakam delta, an economically important area for its oil reserves. Predictions of floods and droughts are important with respect to urban inundations, shipping related to the inland coal and timber industry, safety of oil rigs, and drinking water supply. Hydrometric records are vital data to study the hydrological processes, to perform runoff simulations and to make predictions. The recent collapse of the bridge in Tenggarong and a coal loading facility in an area downstream of Tenggarong exemplify the importance of understanding the hydraulic-hydrologic characteristics of the river, to better design and maintain water structures and public facilities in the vicinity of the river.

1.4 Research questions

This thesis aims at understanding the discharge dynamics of the central and lower reaches of the River Mahakam. Four objectives corresponding to the subsequent chapters are listed below, which are each followed by related research questions.

Chapter 2: Reveal discharge dynamics of a poorly gauged catchment from H-ADCP measurements

- Which are the main factors influencing discharge in the middle Mahakam area?
- How do factors controlling discharge dynamics affect the stage-discharge relation for Melak station?
- How does the interaction among these factors affect the downstream region?

Chapter 3: Predict discharge from water levels at a tide-dominated site

- What is the benefit of adding water level data from upstream locations and tidal predictions to establishing a hindcast discharge prediction?
- What is the forecast lead time for discharge predictions in a tide-dominated region?

Chapter 4: Quantify the discrepancies between the use of a rating curve and continuous discharge estimates from an H-ADCP monitoring station

- How can a discharge dataset from a rating curve and discharge estimates from H-ADCP measurements improve the performance of a rainfall-runoff model?
- How do quality differences in discharge estimation methods affect water balance estimation and long-term hydrological simulations?

Chapters 5 and 6: Extract flood extent and flood occurrence information from a series of radar images of the middle Mahakam lowland area

- How are different land cover types represented in radar images and how does this representation relate to inundation?
- What is the spatio-temporal pattern of inundation in the Mahakam lowland area?

1.5 Methodology

Data was gathered both from existing sources and from an elaborate field measurement campaign. The field campaign was started in February 2008 and completed in August 2009. ADCP discharge measurement stations were operational in Melak for the middle Mahakam area and near the city of Samarinda for the lower reach of the Mahakam. Boat surveys were carried out at the cross-sections where the H-ADCP was deployed, to establish water discharge through the river section at the monitoring site. The surveys consisted of transects in front of the H-ADCP for determining hydraulic parameters and for calibrating and validating the discharge computation method. To derive discharge estimates from the H-ADCP data, a newly developed method (Sassi et al., 2011) was applied. River and lake bottom soundings were carried out using a single-beam echo-sounder to obtain bathymetry data. Surface water level measurements were carried out using pressure sensors, at stations along the river and in the three main lakes.

To model river discharge at a tidally influenced site, artificial neural networks (ANN) were applied to investigate the benefit of adding data from upstream and downstream locations and tidal predictions at sea, in establishing prediction hindcast and forecast model for discharge, using water level information from various stations. The complexity of the ANN model input was gradually increased by adding one dataset in each experiment. Field measurement data with predicted tidal levels at the Mahakam outer delta region were combined to hindcast and forecast the discharge at the city of Samarinda. Multi-layer perceptron neural networks trained with the Levenberg-Marquardt optimization algorithm were used.

The water balance of the Mahakam upstream of Melak is established by means of a rainfall-runoff model driven by rainfall estimates from the Tropical Rainfall Measuring Mission (TRMM). The HBV light model version (Seibert, 1997; Seibert et al., 2000; Seibert and McDonnell, 2010) was used for this purpose. HBV is a simple conceptual model which is widely used and relatively easy to parameterize (Driessen et al., 2010). Figure 1.5 shows a simplified schematisation of the HBV Light model. The principal components of the model are precipitation, evapotranspiration, storage and runoff. These components are related to each other in a given period of time through the water balance equation given as:

$$P - E_A - \Delta S/\Delta t = Q \tag{1.1}$$

where: P = precipitation ($\mathrm{mm\,d^{-1}}$), E_A = actual evapotranspiration ($\mathrm{mm\,d^{-1}}$), Q = runoff ($\mathrm{mm\,d^{-1}}$), ΔS = change in basin storage (mm), per time step Δt (d).

Radar is suitable for the identification, mapping, and measurement of tropical wetlands, for its cloud unimpeded sensing and night and day operation. Field measurements and satellite radar data were incorporated to study wetland hydrology of the middle Mahakam as one of the storage components of the catchment. Groundwater measurements were taken using pressure sensors. The approach for flood occurrence mapping is to evaluate radar backscatter values of each pixels in PALSAR images. Lake depth data and (ground)water level measurements are used to validate the map.

1.6 Thesis outline

Five chapters on the four main objectives follow the path from the measurement and prediction of river discharge, rainfall-runoff modelling, and remote sensing observations of floods. Each of

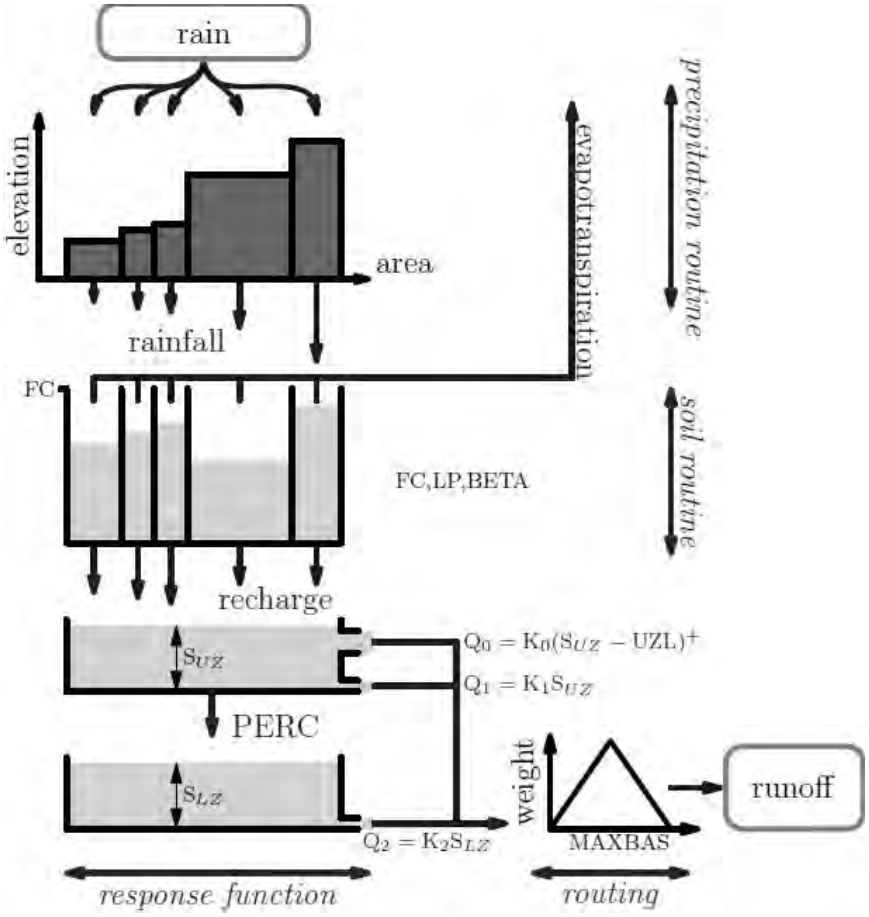

Figure 1.5: The HBV Light model schematisation (adapted from Driessen et al., 2010). FC: maximum soil storage capacity, LP: threshold for evaporation reduction, $BETA$: shape coefficient. The response routine has three recession coefficients, viz. $K0$, $K1$ and $K2$, a reservoir threshold UZL, and a constant percolation rate $PERC$. S_{UZ}: upper groundwater box, S_{LZ}: lower groundwater box, $MAXBAS$: routing parameter.

these chapters can be read independently. Chapter 2 discusses the discharge dynamics in the middle Mahakam, which are subject to backwater effects from lakes, tributaries and floodplains, and to tidal effects. Chapter 3 presents discharge prediction at tidally affected sites using neural networks. Chapter 4 describes a rainfall-runoff relation of the main upstream sub-catchment of the Mahakam, using a hydrological model calibrated using the measured discharge. Chapters 5 and 6 describe the application of radar technology to gain insights into flood (and drought) occurrence in the middle Mahakam region. Finally, chapter 7 presents an extended summary of the main results by providing answers to research questions and concludes this thesis with an outlook.

Chapter 2

Discharge estimation in a backwater affected meandering river

Abstract: Variable effects of backwaters complicate the development of rating curves at hydrometric measurement stations. In areas influenced by backwater, single-parameter rating curve techniques are often inapplicable. To overcome this, several authors have advocated the use of an additional downstream level gauge to estimate the longitudinal surface level gradient, but this is cumbersome in a lowland meandering river with considerable transverse surface level gradients. Recent developments allow river flow to be continuously monitored through velocity measurements with an acoustic Doppler current profiler (H-ADCP), deployed horizontally at a river bank. This approach was adopted to obtain continuous discharge estimates at a cross-section in the River Mahakam at a station located about 300 km upstream of the river mouth in the Mahakam delta. The discharge station represents an area influenced by variable backwater effects from lakes, tributaries and floodplain ponds, and by tides. We applied both the standard index velocity method and a recently developed methodology to obtain a continuous time-series of discharge from the H-ADCP data. Measurements with a boat-mounted ADCP were used for calibration and validation of the model to translate H-ADCP velocity to discharge. As a comparison with conventional discharge estimation techniques, a stage-discharge relation using Jones formula was developed. The discharge rate at the station exceeded 3250 m^3s^{-1}. Discharge series from a traditional stage-discharge relation did not capture the overall discharge dynamics, as inferred from H-ADCP data. For a specific river stage, the discharge range could be as high as 2000 m^3s^{-1}, which is far beyond what could be explained from kinematic wave dynamics. Backwater effects from lakes were shown to be significant, whereas the river-tide interaction may impact discharge variation in the fortnightly frequency band. Fortnightly tides cannot easily be isolated from river discharge variation, which features similar periodicities.

This chapter is a slightly modified version of: Hidayat, H., Vermeulen, B., Sassi, M. G., Torfs, P. J. J. F., and Hoitink, A. J. F.: Discharge estimation in a backwater affected meandering river, Hydrol. Earth Syst. Sci., 15, 2717–2728, doi:10.5194/hess-15-2717-2011, 2011.

2.1 Introduction

Discharge is the phase in the hydrological cycle in which water is confined in channels, allowing for an accurate measurement compared to other hydrological phases (Herschy, 2009). Reliable discharge data is vital in research focusing on a broad range of topics related to water management, including water allocation, navigation, and the prediction of floods and droughts. Also, it is crucial in catchment-scale water balance evaluations. Hydrological studies relying on rainfall-runoff models require continuous discharge series for model calibration and validation (e.g. Beven, 2012; McMillan et al., 2010).

Discharge estimates are conventionally obtained from a rating curve model, using water level data as input, and a limited number of discharge measurements for calibration. Despite a number of techniques available to account for unsteady flow conditions, water agencies often assume an unambiguous relation between stage and discharge. Both steady and unsteady rating curve models are prone to uncertainties, related to interpolation and extrapolation errors and seasonal variations of the state of the vegetation (Di Baldassarre and Montanari, 2009). Changes in the stage-discharge relations frequently occur due to variable backwater effects, rapidly changing discharge, overbank flow, and ponding in areas surrounding the channel (Herschy, 2009). From discharge uncertainty assessment for the River Po, Di Baldassarre and Montanari (2009) showed that the use of a rating curve can lead to an error in discharge estimates averaging 25.6%.

Single-valued rating curves can produce biased discharge estimates, especially in highly dynamic rivers and streams. In terms of the momentum equation, this bias is the result of temporal and spatial acceleration terms, and the pressure gradient term, which all have to be neglected to justify an unambiguous relation between stage and discharge. River waves featuring such unambiguous relation are termed kinematic. When the pressure gradient term is retained, but the acceleration terms can be neglected, the momentum balance appears as a convection-diffusion equation that can be solved to yield a non-inertial wave as a special type of diffusion wave (Yen and Tsai, 2001). Several formulas have been developed aiming to obtain discharge from parameters that can readily be derived from water level time-series. Among these, the Jones formula (Jones, 1916) is the most well-known, in which the surface level gradient term is approximated using the kinematic wave equation. The Jones' formula has been subject to many investigations since its publication (see Schmidt (2002) and Dottori et al. (2009) for a review). Strictly speaking, it may be more correct to refer to the formula as the Jones-Thomas formula, as it was Thomas who replaced the spatial derivative term by a temporal derivative term, in order to enable estimating the discharge from at-a-station stage measurements (A.D. Koussis, pers. comm.).

Variable backwater is one of the principle factors that cause an ambiguous stage-discharge relation. Backwater from one or several downstream elements such as tributaries, lakes, ponds or dams, complicates rating curve development at hydrometric gauging stations (Petersen-Overleir and Reitan, 2009). Tides superimposed on river discharge can produce subtidal water level variations (Buschman et al., 2009), with periods of a fortnight or longer, which may not immediately be recognized as phenomena controlled by the tidal motion. Potentially, water level setup by river-tide interactions can cause backwater effects beyond the point of tidal extinction (Godin and Martínez, 1994).

Recently, approaches have been developed to account for backwater effects, using a twin gauge approach to obtain estimates of the longitudinal water level gradient. Such ratings are

developed based on records of stage at a base gauge and the fall of the water surface between the base gauge and a second gauge downstream (Herschy, 2009). Considering the water level gradient to be a known variable, the terms representing the pressure gradient and spatial acceleration in the momentum equation can be resolved (Dottori et al., 2009). The application of formulas using simultaneous stage measurements was criticised by Koussis (2010). Dottori and Todini (2010) refuted most of the criticism by Koussis (2010), but acknowledged that in lowland areas with a small bed level gradient, the occurring water level gradient can drop below the measuring accuracy of the level gauge. Dottori and Todini (2010) estimate the minimum distance between the gauges to be in between 2000 and 5000 m when the bed slope is 1×10^{-5}. Since cross-profiles of the water level are not taken into consideration in one dimensional river hydraulics, neither Koussis (2010) nor Dottori and Todini (2010) considered the drawback that arises from lateral water level gradients, which can be considerable especially in meandering rivers characterised by a high sinuosity. In high-curvature river reaches, level gauges on opposite sides of each of the two cross-sections would be needed to infer the longitudinal water surface gradient. We conclude that the twin gauge approach to discharge measurements is suboptimal in lowland meandering rivers, which are most susceptible to backwater effects.

Discharge can be estimated from flow velocity, which bears a much stronger relation to discharge than the water surface. Gordon (1989) was among the first to estimate discharge from a boat-mounted acoustic Doppler current profiler (ADCP), which soon after became a standard means of estimating discharge accurately. ADCP surveys are costly and are carried out merely occasionally. Recent developments allow horizontal profiles of flow velocity to be continuously monitored by a horizontal acoustic Doppler current profiler (H-ADCP). The H-ADCP is typically deployed at a river bank, measuring a horizontal velocity profile across a channel. The acquired data can then be used to estimate discharge, predicting cross-section integrated velocity from the array data of flow velocity.

Several methods are available to convert H-ADCP data to discharge. In the Index Velocity Method (IVM), H-ADCP velocity estimates are averaged and linearly regressed with those obtained from boat-mounted ADCP measurements, then discharge is obtained from the area-velocity relation (Simpson and Bland (2000); Le Coz et al. (2008)). Nihei and Kimizu (2008) adopted a deterministic approach, assimilating H-ADCP data with a two-dimensional model of the velocity distribution over a river cross-section. In the velocity profile method (VPM) described by Le Coz et al. (2008), total discharge is inferred from theoretical vertical velocity profiles, made dimensional with the H-ADCP velocity measurements across the section, extrapolated over the river width. Hoitink et al. (2009) combined elements of the IVM and VPM methods, using a boundary layer model to calculate specific discharge from a point measurement of velocity, and a regression model to relate specific discharge to total discharge. Sassi et al. (2011) elaborated on the work of Hoitink et al. (2009) by embedding a more sophisticated boundary layer model that accounts for side wall effects in the methodology, and letting model coefficients be stage dependent instead of constant. Whereas both Hoitink et al. (2009) and Sassi et al. (2011) focused on tidal rivers, this chapter presents an H-ADCP deployment in a backwater affected inland river.

The remainder of this chapter is organized as follows. Section 2.2 describes the field site and data gathering. Section 2.3 presents flow structure and the techniques adopted to convert H-ADCP velocity data to total discharge, applying the method by Sassi et al. (2011). Also,

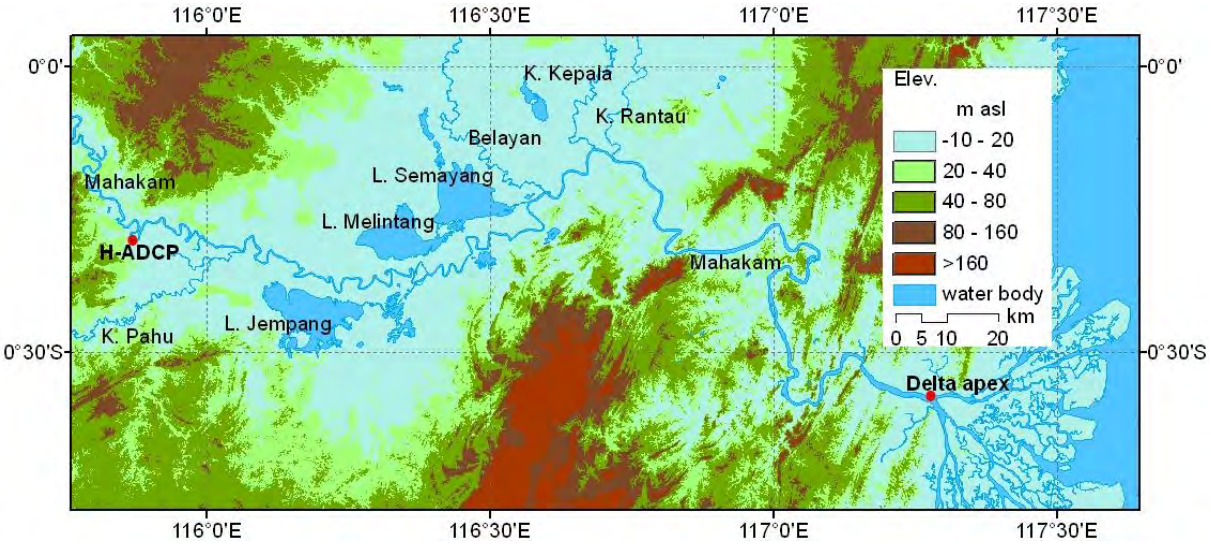

Figure 2.1: Location of H-ADCP discharge station in the Mahakam River, plotted on a digital elevation model obtained from Shuttle Radar Topographic Mission (SRTM) data.

traditional rating curve techniques used for comparison are described. Section 2.4 presents the results and a discussion and in Sect. 2.5 conclusions are drawn.

2.2 Study area and data gathering

This study is based on measurements carried out in the River Mahakam in East Kalimantan. The H-ADCP measurement station is located in Melak in the middle Mahakam area about 300 km from the delta apex (Fig. 2.1). The middle Mahakam area is an extremely flat tropical lowland with some thirty shallow lakes connected to the Mahakam through small channels. It can be considered a remote, poorly gauged region. A tributary, River Kedang Pahu, meets the Mahakam about 30 km downstream of Melak. Downstream of the lakes region, the Mahakam is tied to three other main tributaries (River Belayan, Kedang Kepala, and Kedang Rantau) and flows south-eastwards until the discharge is divided over delta distributaries debouching into the Makassar Strait.

The H-ADCP discharge measurement station was operational at a 270 m wide cross section of the Mahakam river in Melak (Fig. 6.8) between March 2008 and August 2009. A 600 kHz H-ADCP manufactured by RD Instruments was mounted on a solid jetty in the concave side of the river bend. Riverbanks at this particular location are quite steep, leading to a cross-section with a relatively confined flow, except at very high and unusual discharges. The H-ADCP was mounted at about 2.5 m below the lowest recorded water level and about 2 m from the bottom. Pitch and roll of the instrument remained relatively constant during the measuring period, amounting to 0.3° and 0.01°, respectively. The measurement protocol for the H-ADCP consisted in 10 min bursts at 1 Hz every 30 min.

The H-ADCP used in this study is a three-beam instrument with angles between beams of 25° and an acoustic beam width ϕ of 1.2°. The H-ADCP was installed at a distance $d = 7.9$ m

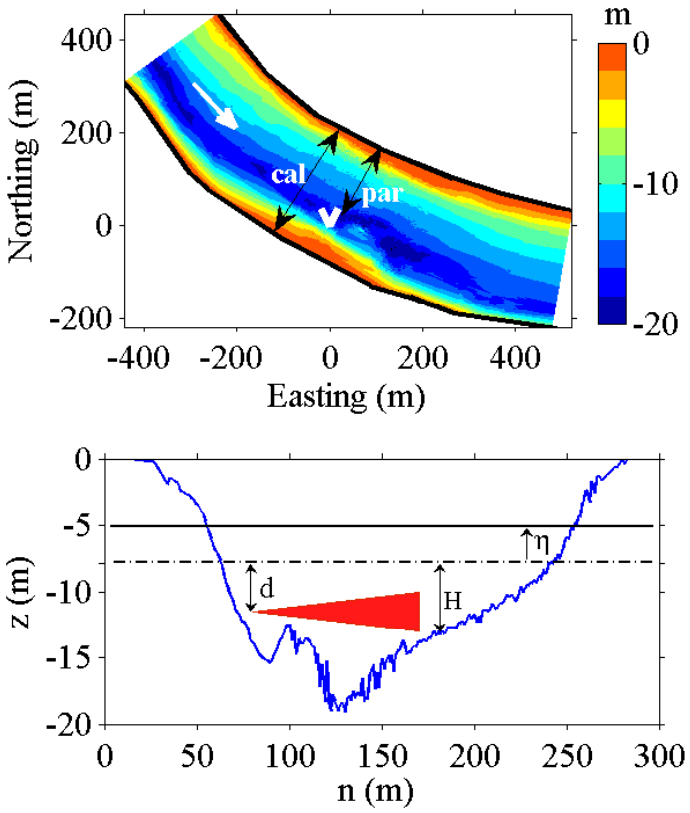

Figure 2.2: Top: bathymetry at Melak discharge gauging station. The arrow indicates flow direction, V indicates the location where the H-ADCP was deployed, double arrows indicate locations of boat-mounted ADCP transects. Bottom: channel cross-sectional profile at the station. The shaded area indicates cross-section of the H-ADCP conical measuring volume, d is the distance of the H-ADCP below the mean water level, H is mean water depth, η is water level variation, and z is normal distance from the bed.

below the mean water level, with the transducer head at $x = 74.4\,\mathrm{m}$ from the shore. The lowest recorded water level was used as the reference water level. Because the H-ADCP was deployed looking slightly upward, the H-ADCP measured a volume-averaged velocity at elevation z_c, which is calculated from:

$$z_c = \begin{cases} -d + \tan(\theta)(n-x) \text{ if } d + \eta > \tan(\phi/2 + \theta)(n-x) \\ -d + \tan(\theta)(n-x) + \Delta z \quad \text{otherwise} \end{cases} \tag{2.1}$$

where θ is pitch, n is cross-channel coordinate, with the origin at the river bank and η is water level variation. Δz is the level difference between the centroid of the ensonified water area and the central beam axis. This correction accounts for the lowering of the centroid of the ensonified water volume if the main lobe intersects with the water surface at low water (Hoitink et al., 2009).

Conventional boat-mounted ADCP measurements were periodically taken at the cross-section where the H-ADCP was deployed to establish water discharge through the river section. Six surveys were carried out spanning low and high flow conditions. The survey consisted of transects in front of the H-ADCP for determining hydraulic parameters (referred to as "par") and transects carried out about 20 m upstream to cover the whole river section for calibrating and validating the discharge computation (referred to as "cal" and "val", respectively). Each transect measurement spanned over about two hours. The boat was equipped with a 1.2 MHz RDI Broadband ADCP measuring in mode 12, a DGPS compass and an echosounder. The ADCP measured a single ping ensemble at approximately 1 Hz with a depth cell size of 0.35 m. Each ping was composed of 6 sub-pings, separated by 0.04 s. The range to the first cell center was 0.865 m. The boat speed ranged between 1 and $3\,\mathrm{m\,s^{-1}}$.

Recently, Moore et al. (2010) found that H-ADCP data can be flawed by the effect of acoustic side lobe reflections from the water surface or from the bed. Fig. 2.3 investigates data quality from a comparison between H-ADCP velocity estimates with corresponding boat-mounted ADCP data (top panel), and profiles of H-ADCP backscatter, averaged over the three beams (bottom panel). The agreement between H-ADCP and boat-mounted velocity estimates is not as good as reported by Hoitink et al. (2009) and Sassi et al. (2011), which is caused by substantial horizontal velocity shears related to the jetty protruding over 30% of the river width. Since the sampling volume of the horizontal cells of the H-ADCP do not exactly match with the vertical cells of the boat-mounted ADCP, discrepancies as observed can be expected in a shear flow. In addition, as argued by Hoitink et al. (2009), the quality of the conventional ADCP measurement from a boat that turns may be lower than that of a H-ADCP, explaining the discrepancies in the field near the transducer. The uniformity of the H-ADCP velocity profiles, and the gradual decrease of the H-ADCP backscatter profiles with distance from the transducer, confirm that the H-ADCP velocity estimates are based on reflections from the acoustic main lobes. Side lobes would raise the backscatter profile and lead to underestimation of the velocity magnitude, which is not the case.

Depth estimates from the ADCP bottom pings were used to construct a local depth map. The range estimation from the four acoustic beams was corrected for pitch, roll, and heading of the ADCP, and referenced to the mean water level. Bathymetry data were also collected using a single beam echosounder for validation. Water levels were measured using pressure transducers in Melak at the H-ADCP station, in Lake Jempang, and in Muara Kaman at the confluence of River Kedang Rantau with the Mahakam, downstream of the Makaham lakes area.

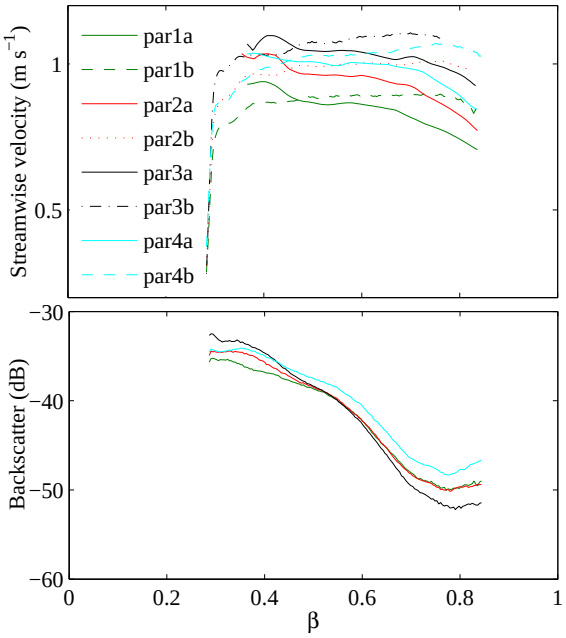

Figure 2.3: Top panel: Comparison of streamwise velocity profiles estimated from boat-mounted ADCP measurements (index a) and H-ADCP data (index b) during the surveys used for parameter assessment. Bottom panel: H-ADCP backscatter profiles, averaged over the three beams, for the surveys corresponding to the top panel.

2.3 Methods to estimate discharge

2.3.1 Flow structure

The design of an appropriate discharge estimation method requires information about the local flow structure, which is discussed in the present section based on the boat-mounted ADCP surveys. The ADCP velocity measurements were projected onto normalized (β, σ) coordinates. The normalized spanwise coordinate β was obtained by normalizing the distance from the bank to the maximum width within that survey. The total width value to normalize β is 270 m. The normalized vertical coordinate σ was obtained from:

$$\sigma = \frac{H + z}{H + \eta} \tag{2.2}$$

where H is mean water depth, z is normal distance from the bed. The mesh size of the coordinate was $\Delta\beta = 0.025$ and $\Delta\sigma = 0.05$. Turbulence fluctuations were removed by taking the mean over the repeated velocity recordings for each grid cell within a survey. Velocity

profiles from boat-mounted ADCP measurements were then averaged over depth according to:

$$\vec{U} = \int_0^1 \vec{u}(\sigma, \beta, t)\mathrm{d}\sigma \tag{2.3}$$

$$\vec{V} = \int_0^1 \vec{v}(\sigma, \beta, t)\mathrm{d}\sigma \tag{2.4}$$

where $\vec{u}$ and $\vec{v}$ are mean velocity components in streamwise and spanwise directions, respectively.

Flow velocity in the Mahakam River varied between moderate and high during the calibration and validation surveys. Figure 2.4 shows the spatial structure of velocity during each ADCP survey. Velocity patterns among different surveys show similar spatial characteristics. Relatively low velocity is observed in the upstream area behind the jetty, where the H-ADCP was deployed. High velocity is distributed from the middle section toward the opposite bank and decreases to a zone of null velocity at $\beta > 0.9$. Due to technical problems, the ADCP transects covering the whole cross section were not taken during the extremely low flow condition. We did navigate the cross-river transect in front of the jetty at low flow. Figure 2.5 shows the vertical velocity profile obtained from averaging between $\beta = 0.35$ and 0.65, for each survey. Within the latter range for β, velocity profiles are relatively stable during different stream flow conditions. The vertical velocity profiles are shown to be largely logarithmic, except for a small region near the surface where a velocity dip can be observed, especially during high flow conditions.

We applied the methods described by Sassi et al. (2011) and the IVM to obtain a continuous discharge estimate from H-ADCP data. As a comparison with conventional discharge estimation technique, a stage-discharge relation using Jones formula is developed.

2.3.2 Semi-deterministic semi-stochastic method

The semi-Deterministic semi-Stochastic Model (DSM) developed by Hoitink et al. (2009) and Sassi et al. (2011) consists of the following parts:

Deterministic part

Time-series of single point velocity $\vec{u}_c$, measured at the relative height σ_c, are translated into depth-mean velocity $\vec{U}$ according to:

$$\vec{U} = F\vec{u}_c \tag{2.5}$$

where

$$F = \frac{\ln\left(\frac{H+\eta}{\exp(1+\alpha)}\right) - \ln(z_0)}{\ln(\sigma_c(H+\eta)) + \alpha\ln(1-\sigma_c) - \ln(z_0)} \tag{2.6}$$

Herein, α accounts for sidewall effects that retard the flow near the surface by means of secondary circulations and z_0 is the apparent roughness length. The value of α is obtained from:

$$\alpha = \frac{1}{\sigma_{\max}} - 1 \tag{2.7}$$

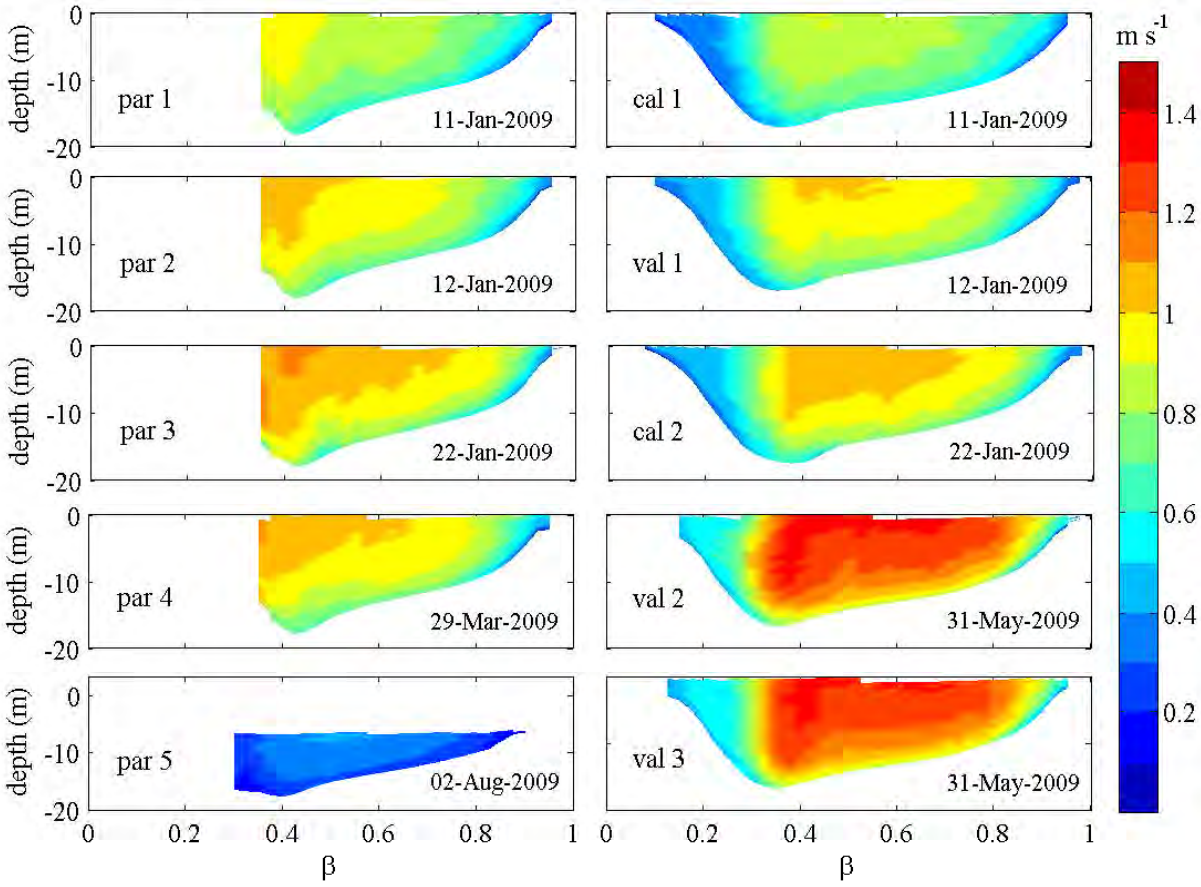

Figure 2.4: Streamwise velocity spatial structure over the cross-section during boat-mounted ADCP surveys. Transects labelled "par" were taken in front of the H-ADCP to obtain hydraulic parameters, while the ones labelled "cal" and "val" were taken 20 m upstream to cover the whole channel width for calibration and validation.

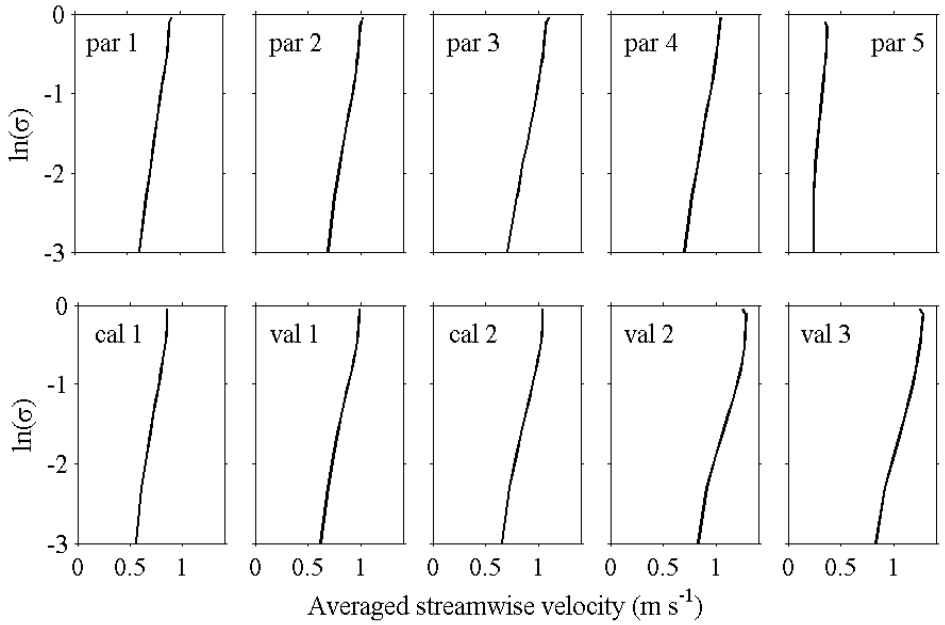

Figure 2.5: Velocity profiles averaged over the middle part of the river section ($\beta = 0.35 - 0.65$) during the ADCP surveys.

where $\sigma_{\max}$ is the relative height where the maximum velocity occurs. To estimate $\sigma_{\max}$ we closely followed the approach of Sassi et al. (2011) by repeatedly fitting a logaritmic profile starting with the lowermost three ADCP cells, adding successively a velocity cell from the bottom to the top for each fit. $\sigma_{\max}$ is determined from the development of the goodness of fit which decreases once the cell above $\sigma_{\max}$ is included. Figure 2.6 illustrates that cross-river profiles of α do not show a systematic variation between $0.2 < \beta < 0.9$. We adopt a constant value of $\alpha = 0.28$, which results in $\sigma_{\max} = 0.78$.

The determination of the effective hydraulic roughness length z_0 is fundamental in the approaches by both Hoitink et al. (2009) and Sassi et al. (2011). The value of z_0 is obtained as:

$$z_0 = \frac{H + \eta}{\exp\left(\frac{\kappa \vec{U}}{\vec{u}_*} + 1 + \alpha\right)} \tag{2.8}$$

where κ is the Von Karman constant and $\vec{u}_*$ is the shear velocity. Values of u_* coincide with the slope of the linear regression line of $u(\sigma)$ against $(\ln(\sigma) + 1 + \alpha + \alpha \ln(1 - \sigma))/\kappa$ (Sassi et al., 2011). Figure 2.7 shows that values of z_0 change over width and are consistent at each β location for each ADCP surveys in the range $\beta > 0.4$. The geometric mean of z_0 at each β location over all boat-mounted transects in front of the H-ADCP (par) were taken for further computation, processing only the H-ADCP data in the range $\beta > 0.4$.

Stochastic part

In the stochastic part of the method, a regression model is developed to translate specific discharge to total discharge, which renders the need for the H-ADCP to cover the full width of

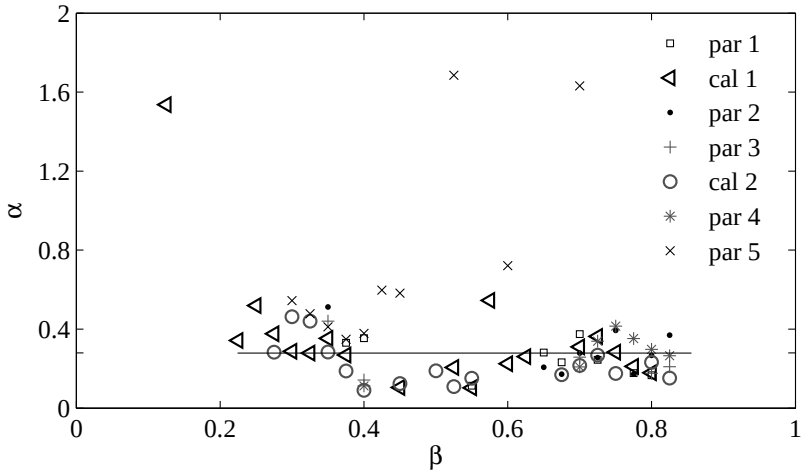

Figure 2.6: Profiles of α across the river section for boat-mounted ADCP parameter and calibration surveys. In the conversion model $\alpha = 0.28$ is taken for $\beta > 0.35$.

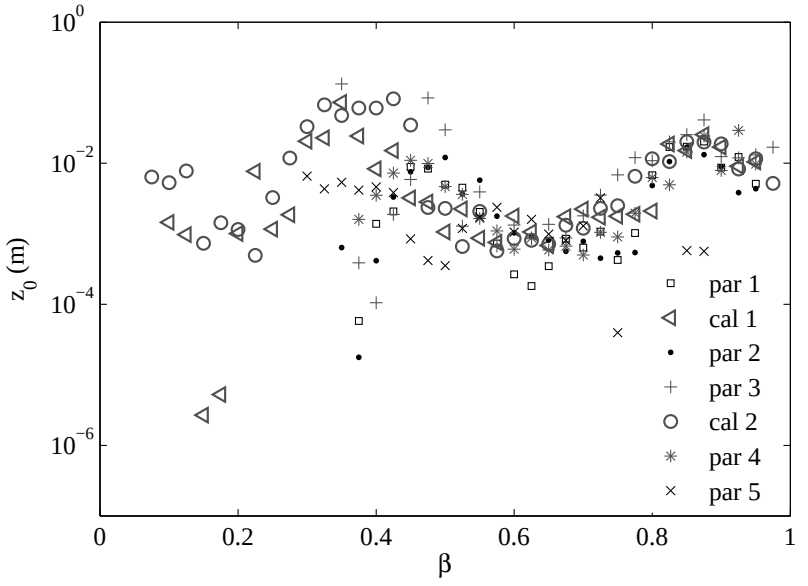

Figure 2.7: Cross-river profiles of z_0 for boat-mounted ADCP parameter and calibration surveys.

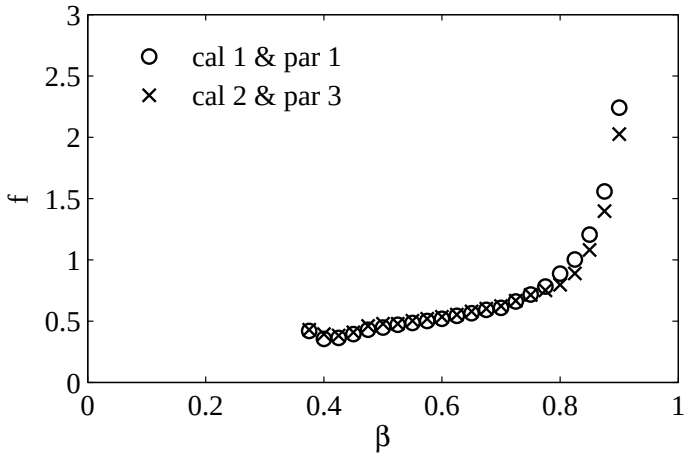

Figure 2.8: Amplification factor f obtained for quasi-simultaneous boat-mounted ADCP parameter and calibration surveys.

the profile superfluous. Specific discharge $\vec{q}$ is obtained from $\vec{q} = \vec{U}(H + \eta)$, where $\vec{U}$ is depth mean velocity estimates from H-ADCP measurements. The regression model to estimate total discharge $\vec{Q}$ from $\vec{q}$, uses an amplification factor f that depends only on the position in the cross-section:

$$\vec{Q}(t) = f(\beta)B\vec{q}(\beta, t) \tag{2.9}$$

where B is the river width, $f(\beta)$ is obtained from the total discharge of each boat-mounted ADCP "cal" survey divided by the product $B\vec{q}$ from the corresponding "par" surveys. Hoitink et al. (2009) discusses the independence of $f(\beta)$ from time and the rationale to include this constant amplification factor in the linear model to estimate $\vec{Q}$. Profiles of f remain constant up to $\beta = 0.8$ during the two calibration surveys (Fig. 2.8), which shows how $\vec{q}$ times B relates to $\vec{Q}$. From the two f profiles, the mean value of f at each beta location was taken and multiplied by q at a single beta position to compute discharge. Hence, from each of the discrete ranges to the H-ADCP velocity cells, a time-series of total discharge was obtained. Time-series of $\vec{Q}$ were finally obtained by averaging up to $\beta = 0.7$ yielding accurate discharge estimates at any moment in time.

2.3.3 Index velocity method

We also estimated discharge from the H-ADCP data based on the IVM approach (Le Coz et al., 2008). We compute discharge by regressing the H-ADCP index velocity with cross-section averaged velocity, yielding discharge after multiplying it with the cross-section area. We used the more representative and accurate part of the HADCP velocity profile data from $\beta = 0.5$ to 0.7 for computing the index velocity. The IVM discharge was computed as:

$$\vec{Q}_{IVM} = f(\vec{u})A \tag{2.10}$$

where $\vec{u}$ is the index velocity and A is river cross sectional area calculated from the bathymetry profile and the measured water level. The reference mean velocity $\vec{U}_H$ at the H-ADCP section

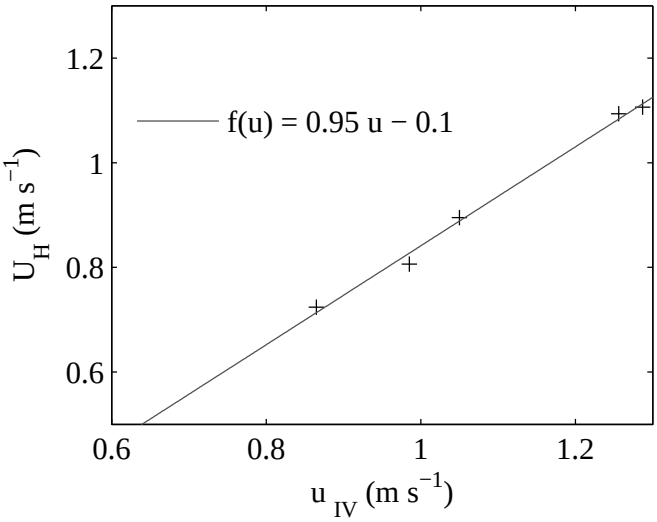

Figure 2.9: IVM rating fitted by linear regression over five boat surveys covering the whole channel width.

is obtained from: $\vec{U}_H = \vec{Q}_{ref}/A$, herein $\vec{Q}_{ref}$ is the reference discharge measured by ADCP. The linear regression over five ADCP surveys covering the whole channel cross section yielded $f(\vec{u}) = 0.95\vec{u} - 0.1$ (Fig. 2.9).

2.3.4 Stage-discharge relation

To investigate the degree in which discharge at Melak station can be captured by a rating curve, Jones' formula was applied, which reads:

$$\vec{Q} = \vec{Q}_{\text{kin}} \left\{ 1 + \frac{1}{\vec{c} S_0} \frac{\partial h}{\partial t} \right\}^{1/2} \tag{2.11}$$

where $\vec{Q}_{\text{kin}}$ is the kinematic or equilibrium discharge, $\vec{c}$ is the wave celerity, S_0 is the bed slope, and $\partial h/\partial t$ is the rate of water level change in time t all measured at the same location (Petersen-Overleir, 2006). The celerity $\vec{c}$ was estimated from $c = \frac{dQ}{dA} = B^{-1}\frac{dQ}{dh}$ (Henderson, 1966) based on the steady flow rating curve obtained for Melak. Herein, A is river cross sectional area and B is river width. The bed slope of 10^{-4} was estimated from the Mahakam River bed level profile derived from SRTM data by van Gerven and Hoitink (2009). $\vec{Q_{\text{kin}}}$ was calculated using the Manning formula:

$$\vec{Q}_{\text{kin}} = \frac{1}{n} S_0^{1/2} A R^{2/3} \tag{2.12}$$

where n is Manning roughness coefficient and R is hydraulic radius obtained from the ratio between A and the wetted perimeter of the river cross-section. The Manning coefficient was estimated based on an evaluation of the river geometry and composition, following a standard empirical technique provided by Gore (2006). The details of channel evaluation to determine n are presented in Table 1.

Table 2.1: Evaluation of channel conditions at Melak station to estimate the Manning coefficient.

Factor (index)	Description (value)
Additive factors	
– Material involved (n_0)	Earth (0.02)
– Degree of irregularity (n_1)	Minor (0.005)
– Var. in location of thalweg (n_2)	Gradual (0.00)
– Effect of obstruction (n_3)	Negligible (0.00)
– Riparian vegetation (n_4)	Medium (0.01)
Multiplicative factors	
– Degree of meandering (m)	Appreciable (1.15)
$n = (n_0 + n_1 + n_2 + n_3 + n_4)m = 0.04025$	

We used the rating curve discharge estimate from Eq. 2.11 in most of the discussion in Sect. 4. Eq. 2.12, however, is used with the assumption that the river reach (Fig. 6.8, top panel) has a uniform channel geometry. The presence of the jetty and boats resulted in irregularity in the channel cross-section (Fig. 6.8, bottom panel) locally at the station. In the original version of the Jones formula, the discharge taken from the currently available steady flow rating curve (Q_0) is used instead of using Eq. 2.12. For a comparison, we also computed discharge using the Jones' formula based on Q_0.

2.4 Results and discussion

Table 4.2 shows the validation results. Discharge estimates obtained by applying the method by Sassi et al. (2011) and IVM differed less than 5% from the accurate estimates obtained from the boat surveys. Figure 2.10 shows time-series of the absolute and relative difference between Q_{DSM} and Q_{IVM}, which indicate that the validation results represent the medium to high flows well. During low flows, Q_{DSM} and Q_{IVM} can deviate much more, both in a relative and in an absolute sense. Unfortunately, a planned validation survey during the low flow condition was cancelled due to technical problems, which could have shed more light on the validity of the low-flow discharge estimates. Regarding high flows, the larger difference between Q_{DSM} and Q_{IVM} could be due to the fact that the H-ADCP is monitoring flow at a relative depth that changes with the river stage, which challenges the constancy of the conversion factor to calculate discharge from the index velocity. The IVM is heavily dependent on the degree in which the velocity measurements within the H-ADCP range unambiguously covary with the cross-section averaged velocity and on the degree in which the calibration surveys cover extreme conditions. The obtained results highlight the merits of applying the more elaborate procedure advocated by Hoitink et al. (2009) and Sassi et al. (2011) particularly in a remote poorly-gauged area. Compared to the IVM, the DSM is more physically based, which provides a better resilience to cope with a lack of discharge measurements during high flows and low flows. Even in the case of an equal performance, as established from a small number of validation surveys in our study, the DSM is to be preferred because the IVM can be right for the wrong reasons. The IVM is

Table 2.2: Results of the three validation surveys of the DSM and the IVM methods. Q_{BS} denotes the discharge calculated from the boat survey, which can be considered truth.

Val.	Q_{BS}	Q_{DSM}	Q_{IVM}	Q_{DSM}/Q_{BS}	Q_{IVM}/Q_{BS}
1	1823	1875	1889	1.03	1.04
2	2438	2439	2465	1.00	1.01
3	2387	2417	2382	1.01	1.00

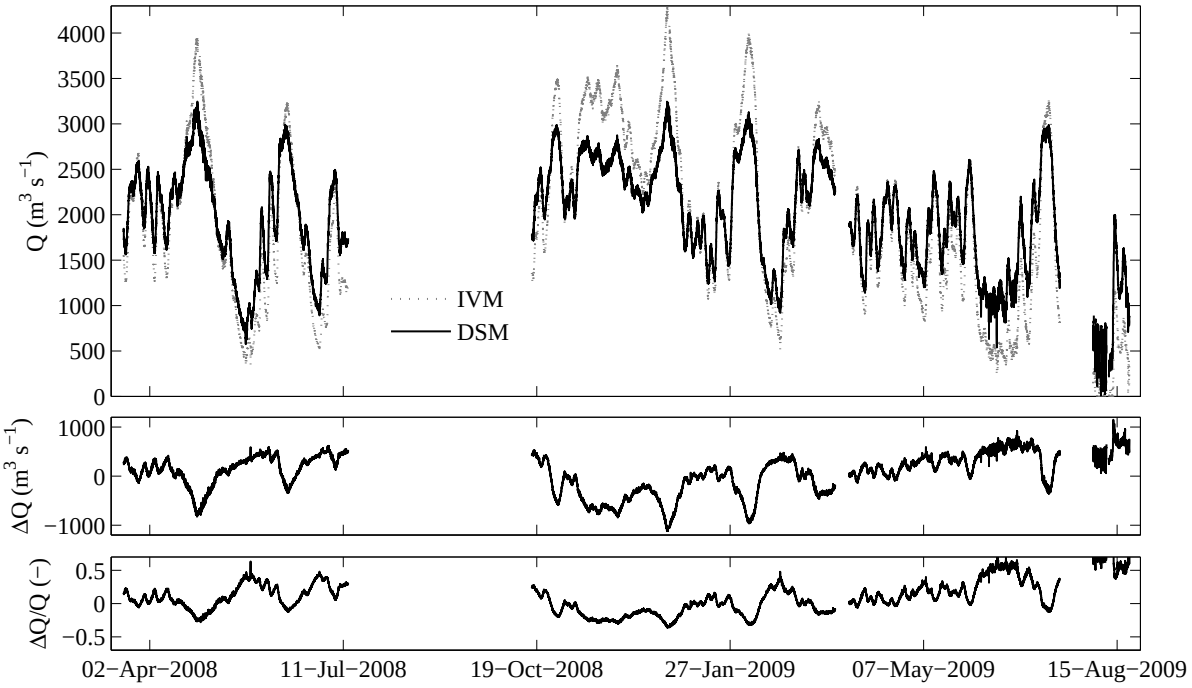

Figure 2.10: Continuous series of discharge estimates derived from H-ADCP data with the DSM and the IVM. Central and bottom panels offer a comparison between DSM and the IVM to convert H-ADCP data to discharge, where $\Delta Q = Q_{DSM} - Q_{IVM}$.

only to be preferred over the DSM when calibration data cover the full range of conditions and there are no inertial effects, which create a time lag between local flow velocity and cross-section averaged flow velocity.

H-ADCP measurements at Melak station revealed a complex stage-discharge relation that was highly hysteretic (Fig. 2.11). Hysteresis is generally related to flood wave propagation affected by transient flow. For the same water level, discharge is typically higher than average during rising stage and lower than average during falling stage, resulting in distinctive loops in stage-discharge relations (Petersen-Overleir, 2006). Backwater effects that cannot be isolated completely from nonlinear wave effects complicate this relation. Figure 2.12 shows that variable backwater effects were likely to occur within the hysteresis loop. At Melak station, the range of discharges that can occur for a specific stage can span over more than $2000\,m^3\,s^{-1}$, which is exceptionally large in comparison with the maximum discharge of $3250\,m^3\,s^{-1}$ from the DSM. Such variation can be considered far beyond the rising stage and falling stage expla-

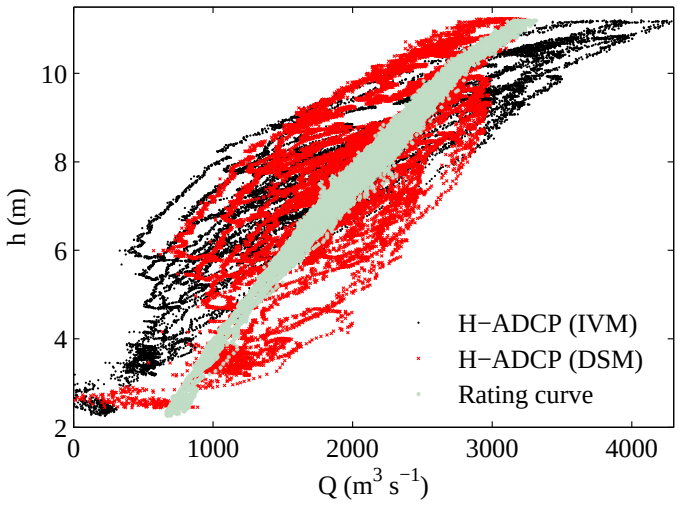

Figure 2.11: Water stage and discharge estimates at Melak station, obtained from a rating curve (Jones' formula) and from H-ADCP measurements. Water stage is with respect to the position of a pressure gauge about 9 m from the deepest part of the river cross-section.

nation. Compared to standard rating curves for different hydraulic conditions (Herschy, 2009), the stage-discharge relation in Fig. 2.11 will reflect the presence of variable backwater effects, looping due to changing discharge, and multiple looping due to overbank flow and ponding. Radar images showed vast areas in the Mahakam Lakes Region to become inundated during high flows (Hidayat et al., 2011a). Part of the complexity in the stage-discharge relation can be explained from the subharmonics generated by river-tide interactions (Buschman et al., 2009). It is striking that tidal influence can reach the site, which is located 300 km upstream of the river mouth in the Mahakam delta. At low discharges in August 2009, the tidal signal is clearly visible in the discharge series. Due to the flat terrain of the middle and lower Mahakam, tidal energy propagates up to the Mahakam lakes area, where much of the tidal energy is dissipated. Subharmonics such as the MSf, an oceanographic term for the fortnightly constituent of the tide created by nonlinear interaction of the tides induced by the Moon and the Sun with the river discharge, may extend beyond the lakes region. However, this effect cannot be readily isolated from river discharge variation as discharge variation features fortnightly variation both in the presence and in absence of a tidal influence.

The wide loops in the stage-dischage plot are the result of the geographical complexity of the region where Melak station is located, experiencing a flashy discharge from upstream and backwater effects from downstream. The flashy discharge regime relates to high rainfall rates in large parts of the catchment upstream of Melak, which dominates the moderating effect of the rain forest. The backwater effects are caused both by the lakes and a number of tributaries, all affecting the water level profile. Lake emptying and filling processes contribute to retarding and accelerating the river flow velocity. Figure 2.13 illustrates the lake emptying and lake filling influencing water levels and discharge upstream. At the start of lake emptying, when the lake level was still high, water stage in Melak was relatively high for a relatively low discharge. When the lake level dropped, the backwater effect was reduced and discharge increased while water stage kept decreasing until the point that discharge was sufficiently high to make water stage

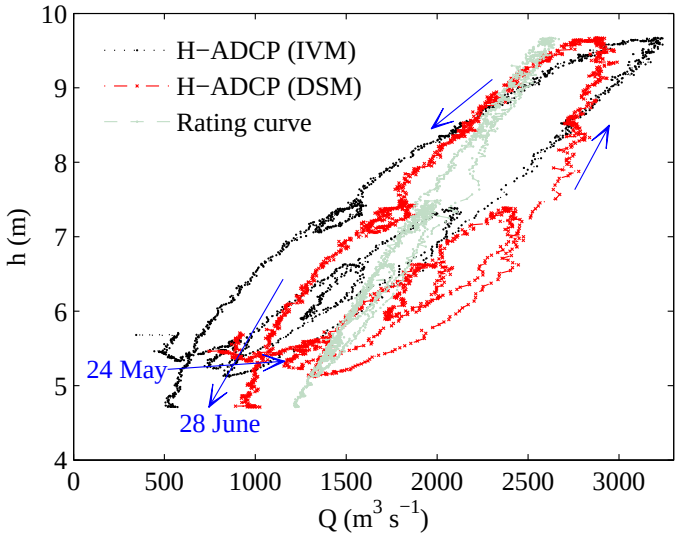

Figure 2.12: Water stage versus discharge for the period between 24 May – 28 June 2008. Multiple loops and discharge oscillations indicate variable backwater effects also occurred within the hysteresis loop.

follow the trend in the discharge time-series. The opposite mechanism took place during lake filling as shown in Fig. 2.13 (bottom panel). Water stage records downstream of the Mahakam lake area (Muara Kaman) indicate that some peaks of water level were shaved by the lake filling and emptying mechanism.

The discharge obtained from the stage-discharge relation using Jones formula is merely a rough estimate of discharge at Melak station, indicating the range of discharge variation. It did not capture the detailed discharge dynamics as revealed by the H-ADCP measurements. This can be related to a wide variety of reasons. The Froude number takes a value around 0.01, which likely indicates the inertial term in the momentum equation to be negligible. A non-dimensional version of the St. Venant equations directly shows that the inertial terms drop out for small values of the Froude number (Pearson, 1989). The key assumption used to derive the Jones formula is the applicability of the kinematic wave equation to deal with the surface gradient term in the non-inertial wave equation. Although this approach can be successful under certain bed slope and flow conditions (Pearson (1989); Perumal et al. (2004); Dottori et al. (2009)), the kinematic wave equation cannot capture discharge dynamics in backwater affected river reaches (e.g. Tsai, 2005). The stage-discharge relation is only expected to be applicable if the channel geometry is uniform. The top panel in Fig. 6.8 shows there is some irregularity in the cross-section, related to the low flow velocities beneath the jetty. Therefore, the complexity of the stage-discharge plot can be partly explained from the non-uniformity of the channel geometry. Figure 2.14 shows the comparison of discharge estimates obtained using the Jones formula based on Q_{kin} (uniform channel geometry assumption) and those based on Q_0 (discharge taken from the steady flow rating curve). During peak discharges, the use of Q_0 instead of Q_{kin} can result in slightly different rating curve-based estimates of the discharge. Out-of-bank spills and return flows from flood plains occurring in the study area during the period of flood peak could also be among possible reasons for the failure of the Jones formula

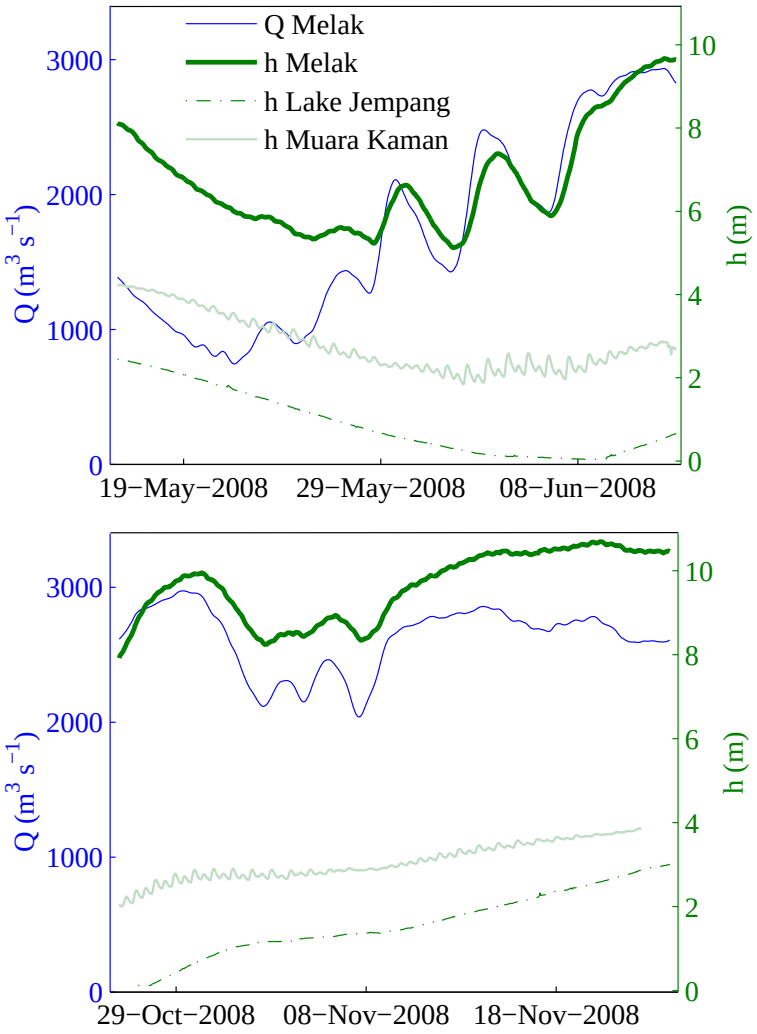

Figure 2.13: Water stage and discharge during lake emptying (top) and during lake filling (bottom). Muara Kaman, where the tidal signal was observed during most of the measurement period, is located downstream of the Mahakam lakes area about 170 km from Melak.

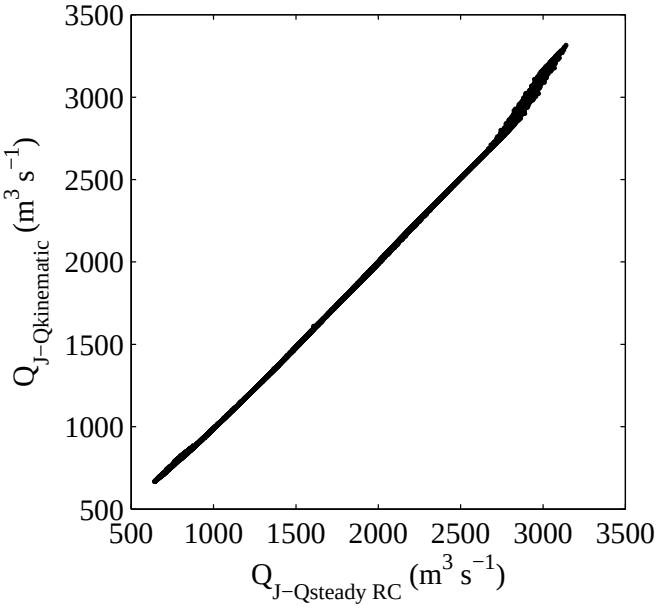

Figure 2.14: Comparison of discharge estimates obtained using the Jones formula based on Q_{kin} (uniform channel geometry assumption) and those based on Q_0 (discharge taken from the steady flow rating curve $Q_0 = 125.98*(h+1.5)^{1.256}$) for the whole observation period. The small deviation confirms that the two approaches yield similar results. Only during peak discharges, the use of Q_0 instead of Q_{kin} can result in slightly different rating curve-based estimates of the discharge.

to adequately predict flood dynamics. The Jones formula is just one of a series of formulas available to predict discharge from time-series of a single level gauge (Henderson, 1966; Di Silvio, 1969; Fread, 1975; Lamberti and Pilati, 1990; Perumal and Ranga Raju, 1999), all aiming to improve the original Jones' formula. Dottori et al. (2009) explicitly mentions that they are best applicable when flow conditions are quasi kinematic. Backwater effects render the kinematic wave assumption invalid, hence none of these approaches will be capable of reproducing the wide loops occurring at Melak station, which underlines the importance of monitoring additional information besides stage at a single section. Considering the ease of deployment of H-ADCPs, they offer a promising alternative to measure discharge.

2.5 Conclusions

Flow measurements using a 600 kHz H-ADCP were carried out at a 300 m wide cross section of the Mahakam River in Melak, 40 km upstream of the Mahakam lakes area. Conventional boat-mounted ADCP measurements were periodically taken to establish water discharge through the cross section. We followed a recently developed semi-deterministic, semi-stochastic method (DSM) to convert the H-ADCP to discharge, and compared the results with those obtained from the index-velocity method (IVM) and a rating curve model. The DSM method was found to be comparable with the IVM, the difference with discharge estimates from the boat-mounted

ADCP surveys was less than 5% based on three validation surveys. The continuous time-series of discharge showed that the validation data were representative for medium to high flows. A stage-discharge model based on Jones's formula captured only a small portion of the discharge dynamics, which was attributed to the invalidity of the kinematic wave assumption due to backwater effects. A discharge range of about $2000\,\mathrm{m^3\,s^{-1}}$ was established for a particular stage in the recorded discharge series, which is about 60% of the peak discharge and therefore exceptionally large. The large range of discharge occurring for a given stage was attributed to multiple backwater effects from lakes and tributaries, floodplain impacts and effects of river-tide interaction, which generate subharmonics that cannot readily be isolated from river discharge oscillations.

Chapter 3

Discharge prediction in a tidal river using artificial neural networks

Abstract: Discharge predictions at tidally affected river reaches are currently still a great challenge in hydrological practices. In tidal rivers, conventional rating curves fail to model stage-discharge relationships, as water levels are not uniquely a function of streamflow. Here, we explore the possibility to predict discharge from water level information from gauge stations at sea and in the river. A hindcast model has been established for a tide-dominated lowland site along the Mahakam River (East Kalimantan, Indonesia), using an artificial neural network (ANN) model. The input data for the ANN was gradually increased, by adding new input data in each step. The results show that the inclusion of data from tide predictions at sea leads to improved model performance. The optimized ANN-based hindcast model produces a good discharge estimation, as shown by a consistent performance during both the training and validation periods. Using this model, discharge can be predicted from astronomical tidal predictions at sea plus water level measurements from a single station at an upstream location. Alternatively, the ANN model can be used as a tool for data gap filling in a disrupted discharge time-series, estimated from horizontal acoustic Doppler current profiler (H-ADCP) data. A single level gauge can thus provide a backup for an H-ADCP monitoring station. In a second line of the work, a forecast model was developed for the same site near the city of Samarinda, using water level data, predicted tide levels, and at-site historical data. The discharge time-series derived from H-ADCP data were used for calibration and validation of the multi-step ahead discharge predictions. A good model performance was obtained when predicting discharge up to 2-days ahead.

This chapter is based on: Hidayat, H., Hoitink, A.J.F., Sassi, M.G., Torfs, P.J.J.F.: Prediction of discharge in a tidal river using artificial neural networks. Submitted to J. Hydrol. Eng.

3.1 Introduction

Many large cities in the world lie on coastal lowlands that need reliable streamflow data and predictions to cope with environmental issues, public safety, and water management. Mitigation of disasters (floods, droughts) and water allocations (drinking water, irrigation, etc) are among water-related issues that require such data. Similar to many other hydrological processes that exhibit a high degree of nonlinearity, conflicting spatial and temporal scales, and uncertainty in parameter estimates (Govindaraju, 2000), streamflow estimation and prediction at tidally affected river reaches is currently still a great challenge. One of the computational tools that is suitable to deal with this is the artificial neural network (ANN).

Originally studied in the framework of artificial intelligence, ANN has now become one of the primary technologies in machine learning, and is a mainstream technology for data-driven modelling (Solomatine and Ostfeld, 2008). A neural network is a universal function approximation method (Govindaraju, 2000). It includes a large number of unknown parameters that are identified by solving an optimization problem. The purpose of an ANN is to generalize a relationship of the form (Govindaraju, 2000):

$$Y^m = f(X^n) \tag{3.1}$$

where X^n is an n-dimensional input vector consisting of variables x_1,...,x_i,...,x_n; and Y^m is an m-dimensional output vector consisting of resulting variables of interest y_1,...,y_i,...,y_m. The functional form of $f(\cdot)$ in Eq. 3.1 will not be revealed explicitly, but will be represented by the network parameters (Govindaraju, 2000). The particular advantage of ANNs is that the network can be trained to learn an input-output relationship even if the exact relationship between sets of input and output data is unknown, but is acknowledged to exist (Minns and Hall, 1996).

Over the last two decades, ANNs have proven to be useful tools for modelling many aspects of the hydrological cycle (see e.g. Govindaraju, 2000; Abrahart and See, 2007; Maier et al., 2010). Applications include rainfall-runoff modelling (Minns and Hall, 1996; Chen and Adams, 2006), radar rainfall estimation (Vulpiani et al., 2006), rainfall forecasting (El-Shafie et al., 2012), streamflow forecasting (Toth and Brath, 2007; Corzo et al., 2009), stage-discharge relation modelling (Supharatid, 2003; Sudheer and Jain, 2003; Bhattacharya and Solomatine, 2005), water level prediction (Chiang et al., 2010; Chen et al., 2012), tidal predictions (Lee, 2004; Liang et al., 2008), sediment transport modelling (Yitian and Gu, 2003), and estimation of groundwater abstraction impact on river flows (Parkin et al., 2007). However, despite the superior performance of ANNs reported in most studies, ANNs are seen as a black-box modelling approach and they are not considered to be useful for providing insights into, or understanding of, watershed processes (Govindaraju, 2000; Chen et al., 2012). Wilby et al. (2003) attempted to answer these concerns by exploring the internal behaviour of an ANN in a rainfall–runoff model. They found that hidden nodes in the neural network correspond to dominant processes within a conceptual model.

In this study, we aim to establish a model to predict discharge in a tidal river from water level information. Unlike the approach that is commonly adopted to obtain stage-discharge relationships based on ANNs (see e.g. Sudheer and Jain, 2003; Bhattacharya and Solomatine, 2005), we establish a relationship between discharge and level gauge information from several

sites, instead of only a single site at the target location. First, we will focus on hindcast discharge predictions, and subsequently on forecasting. We use ANNs for streamflow prediction using data from upstream and downstream locations and water level predictions at sea. We gradually add the complexity of the ANN model input by adding one dataset in each experiment. The object of research is the Mahakam river in East Kalimantan, Indonesia. Discharges will be predicted for a site near the city of Samarinda, which is the capital of East Kalimantan. In the entire lower Mahakam region, predictions of floods and droughts are important with respect to urban inundations, shipping related to the inland coal and timber industry, safety of oil rigs, and drinking water supply. Urban inundations occur almost every year in the cities of Tenggarong and Samarinda, when high rainfall coincides with high tide. Disruptions of drinking water supply due to saltwater intrusion occasionally occur in Samarinda during extreme low-flow conditions, induced by extended drought events. The present study is motivated by problems with both high and low flow events. This chapter continues with the study area and data collection in Section 3.2. Section 3.3 describes the model structure. Section 3.4 presents the results and discussion. In Section 3.5 conclusions are drawn.

3.2 Study area and data collection

3.2.1 A brief description of the study area

The Mahakam river has a catchment area of about 77100 km^2. Figure 3.1 shows the Mahakam catchment with its main sub-catchments. The Mahakam River runs to the Makassar Strait through Samarinda, a provincial capital with 610000 inhabitants in 2009, and the Mahakam delta, an economically important area for its oil reserves. The middle part of the Mahakam mainly consists of lowlands with some forty shallow lakes. Lakes Jempang, Semayang, and Melintang are the three largest lakes in this area. Lake filling and emptying mechanisms play a role in regulating water levels downstream (Hidayat et al., 2011b). Vast areas of the middle Mahakam lowlands are inundated during high water periods (Hidayat et al., 2012) that normally occur in November through December and in March through April, which cover the two periods of rainfall peaks in the region. Rainfall and river discharge in the Mahakam are affected by El Niño-Southern Oscillation (ENSO). Warm El Niño phases lead to reduced convection and drier conditions over Indonesia. Conversely, during La Niña events, an episode of suppressed temperatures afflicts throughout the tropics, which generally leads to intensified heavy rains over the Indonesian archipelago (Ward et al., 2010).

3.2.2 Data collection

From March 2008 through August 2009, horizontal acoustic Doppler current profiler (H-ADCP) measurements were taken at a site near the city of Samarinda. The discharge estimation method at this station is reported in Sassi et al. (2011). The discharge rates in Samarinda exceed 8000 m^3s^{-1}. Intratidal variations were obvious during bidirectional flow conditions, which occurred only during conditions of low river discharge. The tidal wave propagates upriver, reaching the middle Mahakam lakes area, and further upstream. Numerical simulations show that tides are damped when entering the lakes, whereas the fortnightly tidal constituent forces water level

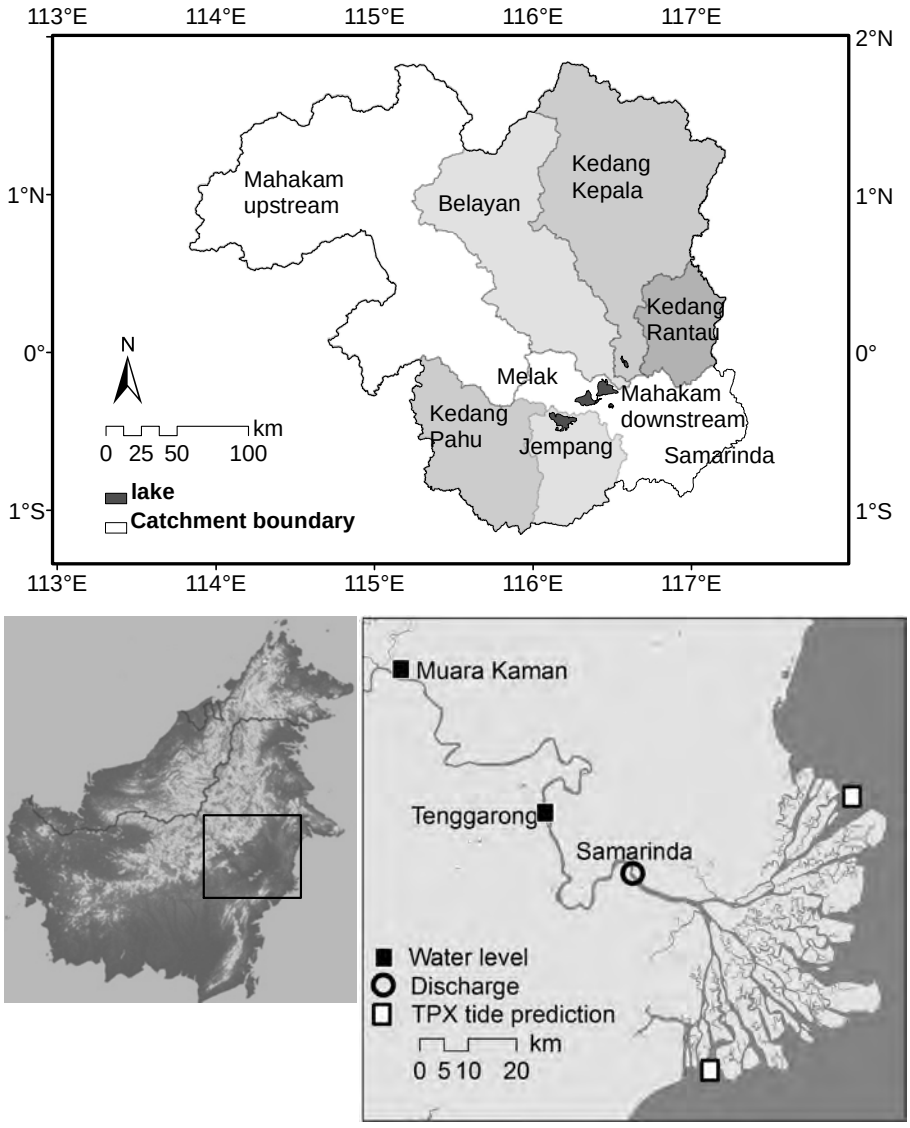

Figure 3.1: Top panel: the Mahakam catchment with a delineation of the main sub-catchments. Bottom left: geographical location. Bottom right: measurement stations used in this study.

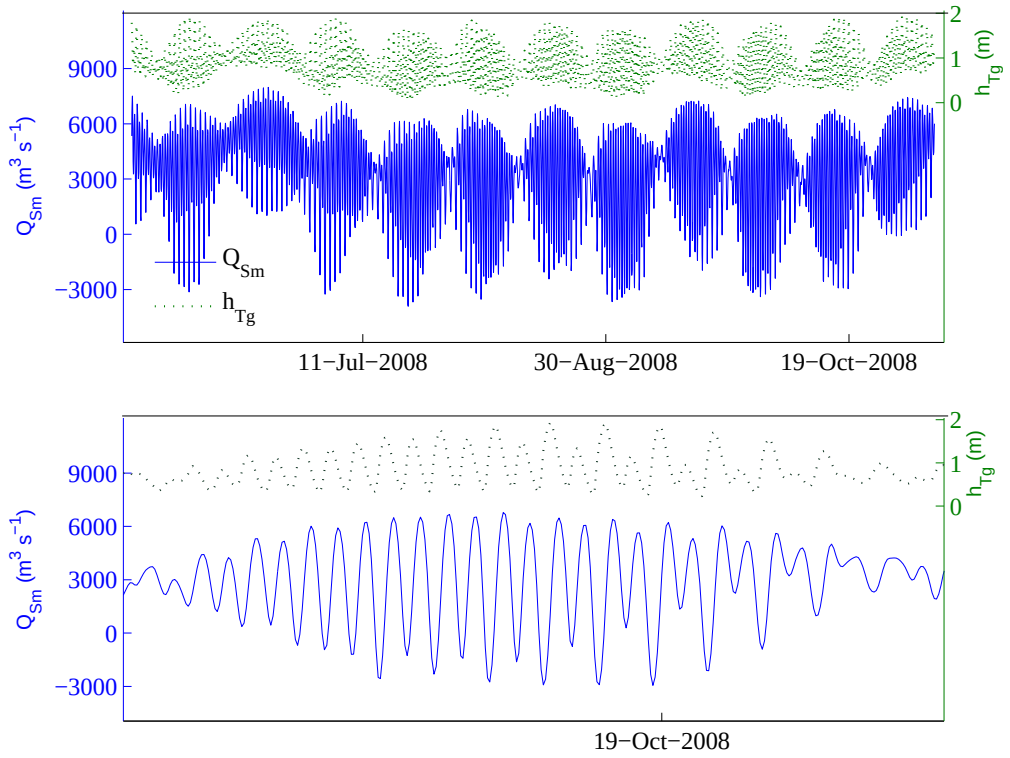

Figure 3.2: Top panel: water levels in Tenggarong (h_{Tg}) and discharge in Samarinda (Q_{Sm}) in hourly time-steps used for model calibration. Bottom: zoom in on a neap-spring cycle.

variation in the lake at specific frequencies (Sassi et al., 2010). However, during discharge peaks, the fortnightly oscillations are damped due to increased river discharge. Water levels were measured using pressure transducers in the middle Mahakam lake area (Lake Jempang), in Muara Kaman, and in the city of Tenggarong (see Fig 3.1). Unfortunately, the pressure transducer installed at the H-ADCP station in Samarinda was malfunctioning, presumably due to clogging of the sensor. Figure 3.2 shows water level records in Tenggarong and discharge series in Samarinda, indicating a high correlation between the two data series. We also used discharge data series from an H-ADCP station upstream of the middle Mahakam lakes area, near the city of Melak. The methods of discharge estimation from continuous H-ADCP data at this station is reported in Hidayat et al. (2011b).

Tide predictions at the Northern and Southern points of outer Mahakam delta were obtained from the TPXO global tidal solution, which is described in Egbert and Erofeeva (2002). Inside the tidal river, a harmonic analysis is inappropriate because the river discharge interacts with the tidal motion, causing the astronomical tides to depend on the river discharge (Jay and Flinchem, 1997; Buschman et al., 2009; Sassi and Hoitink, 2013), which results in an inverse relation between river discharge and tidal amplitudes. Following the wavelet analysis method described in Buschman et al. (2009), time-series of tidal phases and amplitudes were obtained for the diurnal, semidiurnal and quarterdiurnal tides. These phases and amplitudes capture the effect of the tidal motion on the river discharge in six values per day.

3.3 Model structure

3.3.1 ANN models

Multi-layer perceptron (MLP) neural networks were trained with the Levenberg-Marquardt optimization algorithm (Levenberg, 1944; Marquardt, 1963). An MLP, which consists of several layers of mutually interconnected nodes, receives several inputs, calculates the weighted sum of them, and then passes the result to a non-linear function (Solomatine and Ostfeld, 2008). The Levenberg-Marquardt algorithm, which is a modification of the classical Newton algorithm, is often considered as the fastest supervised back propagation algorithm (Chen et al., 2012; Supharatid, 2003). The learning rate was set to 0.1, one hidden layer with sigmoid function was chosen, and a maximum epoch of 1000 was adopted. Previous studies have shown that minimal networks with one hidden layer can offer better generalized performance than more complex networks (Minns and Hall, 1996). The number of nodes in the hidden layer can be determined by a stepwise method, starting with one hidden node and continuing to more complex configurations, with a stepwise addition of hidden nodes. The optimal number of hidden nodes depends on the use of input data, as shown in the next section. The following formula can be used as an initial value of the number of nodes in the hidden layer (NH) (Liang et al., 2008):

$$NH = \frac{NI + NO}{2} \tag{3.2}$$

where NI is the number of neurons in the input layer, and NO is the number of neurons in the output layer.

The selection of input variables forms an important component in ANN modelling. We used the linear correlation along with the average mutual information (AMI) analysis for investigating the dependency between variables and the corresponding lag effect. AMI, which is based on Shannon's entropy theory and belongs to non-linear statistical dependence measures, is more appropriate for determining inputs to ANN models (Maier et al., 2010). The AMI of two random variables taking values in the sets A and B (respectively), is defined by (Bhattacharya and Solomatine, 2005):

$$I_{AB} = \sum_{a_i b_j} P_{AB}(a_i, b_j) log_2 \frac{P_{AB}(a_i, b_j)}{P_A(a_i) P_B(b_j)} \tag{3.3}$$

where $P_{AB}(a_i, b_j)$ is the joint probability density function for the datasets A and B resulting in values a and b, and $P_A(a_i)$ and $P_B(b_j)$ are the individual probability density functions for datasets A and B (respectively). Figure 3.3 shows the correlation and AMI of water levels and discharge datasets at the H-ADCP station in Samarinda. The trend of both measures is in agreement, i.e. the peaks of AMI and correlation values for upstream water levels in Tenggarong and discharge in Samarinda are both at the third lag time. To incorporate the dynamics of tidally affected water levels and discharge into the model, we include the first cycle in the AMI lag time function in the input, which coincides with positive correlation values. For example, to hindcast discharge we include water level data in Tenggarong with time lags between 0 and 6.

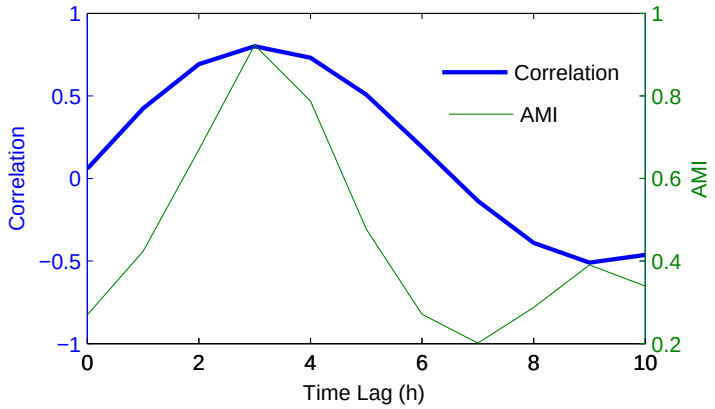

Figure 3.3: Average mutual information (AMI) of the water level in Tenggarong and discharge in Samarinda, and the corresponding correlations.

ANN for hindcast prediction of discharge

Table 3.1 shows the configuration of ANN models for hindcast prediction of discharge, which features a step-by-step increase of input data complexity. The model labelled hQ_0 uses the water level record in Tenggarong, lagged up until the time period with the lowest positive correlation in the AMI analysis. In the hQ_1 model, we added the downstream tide level at the outer delta, obtained from the astronomical tidal prediction at two locations, at the Northern and at the Southern tip of the Mahakam delta. Although the vertical water level fluctuations due to tides at these outer delta locations are included as two model components, they are denoted by a single symbol (ζ_{Od}) for a simpler model representation. In hQ_2, we added upstream water level data pertaining to Muara Kaman station. In model hQ_3 the same data is used as in model hQ_2, complemented with amplitudes of the diurnal (A_1), semi-diurnal (A_2) quarter-diurnal (A_4) tidal components obtained from water level data in Tenggarong. In model hQ_4, we used similar input data as in hQ_3 with the addition of tidal components of water level data in Muara Kaman.

Figure 3.4 shows a schematic diagram of the model configuration for hQ_1. A similar representation applies for the other ANN models, except for the different input datasets. Data from 24 May through 5 November 2008 (3900 data points) were used for calibration, while those from 28 January through 19 March 2009 (1100 data points) were used for validation of the hourly ANN water stage-discharge models.

Forecasting discharge

Table 3.2 shows the configuration of ANN models for predicting discharge in Samarinda ahead in time, again with increasing complexity of the input data. Similar to the hindcast procedure, we used upstream water level data in Tenggarong and astronomical tide predictions for water levels at the outer delta. In the final configuration, water level data from Lake Jempang in the middle Mahakam area and discharge from the upstream station in Melak were added. The time-lagged data of stations to be included in the model were determined by the AMI analysis, based on the measured discharge in Samarinda. Data from 24 May through 30 September 2008

Table 3.1: ANN model input configuration for hindcast prediction of discharge at the station near the city of Samarinda, using water level records at upstream stations in Tenggarong (h_{Tg}), in Muara Kaman (h_{Mk}), predicted tide level at the outer delta (ζ_{Od}), and amplitudes of the diurnal (A_1), semi-diurnal (A_2) and quarter-diurnal (A_4) tidal components of h_{Tg} and h_{Mk}. t is the time (hour).

Model name	model structure
hQ_0	$Q = f\{h_{Tg(t-0...t-6)}\}$
hQ_1	$Q = f\{h_{Tg(t-0...t-6)} + \zeta_{Od(t-0...t-5)}\}$
hQ_2	$Q = f\{h_{Mk(t-0...t-7)} + h_{Tg(t-0...t-6)} + \zeta_{Od(t-0...t-5)}\}$
hQ_3	$Q = f\{h_{Mk(t-0...t-7)} + h_{Tg(t-0...t-6)} + \zeta_{Od(t-0...t-5)} + A_{1Tg(t-2...t-8)} + A_{2Tg(t-1...t-4)} + A_{4Tg(t-7...t-9)}\}$
hQ_4	$Q = f\{h_{Mk(t-0...t-7)} + h_{Tg(t-0...t-6)} + \zeta_{Od(t-0...t-5)} + A_{1Tg(t-2...t-8)} + A_{2Tg(t-1...t-4)} + A_{4Tg(t-7...t-9)} + A_{1Mk(t-0...t-10)} + A_{2Mk(t-0...t-4)} + A_{4Mk(t-0...t-10)}\}$

were used in the model calibration (3900 instances). A dataset covering the period between 28 January through 21 June 2009 served for validation (3300 instances). This relatively longer validation dataset could be used because the water level record in Muara Kaman, which is shorter, was not included in this forecasting part of the work.

3.3.2 Evaluation criteria

The coefficient of determination (R^2), Nash–Sutcliffe coefficient of Efficiency (NSE), and Root Mean Square Error (RMSE) were used to evaluate the model. Values of R^2 quantify how good a predictor can be constructed from the modeled values. The NSE measures the ability to predict variables different from the mean, and gives the proportion of the initial variance accounted for by the model (Nash and Sutcliffe, 1970):

$$NSE = 1 - \frac{\Sigma_{t=1}^{n}[Q_{obs}(t) - Q_{sim}(t)]^2}{\Sigma_{t=1}^{n}[Q_{obs}(t) - \bar{Q}_{obs}]^2} \tag{3.4}$$

where $Q_{obs}(t)$ and $Q_{sim}(t)$ correspond to observed and calculated discharge at time t, $\bar{Q}_{obs}$ is the average observed discharge, and n is the total number of time steps. The RMSE evaluates how closely predictions match observations, based on the relative range of the data:

$$RMSE = \sqrt{\frac{\Sigma_{t=1}^{n}[Q_{sim}(t) - Q_{obs}(t)]^2}{n}} \tag{3.5}$$

3.4 Results and discussion

3.4.1 Discharge hindcasting

The number of nodes in the hidden layer was optimized for each model configuration. Figure 3.5 shows that for a discharge hindcast relationship based on model hQ_0, adopting 5 hidden

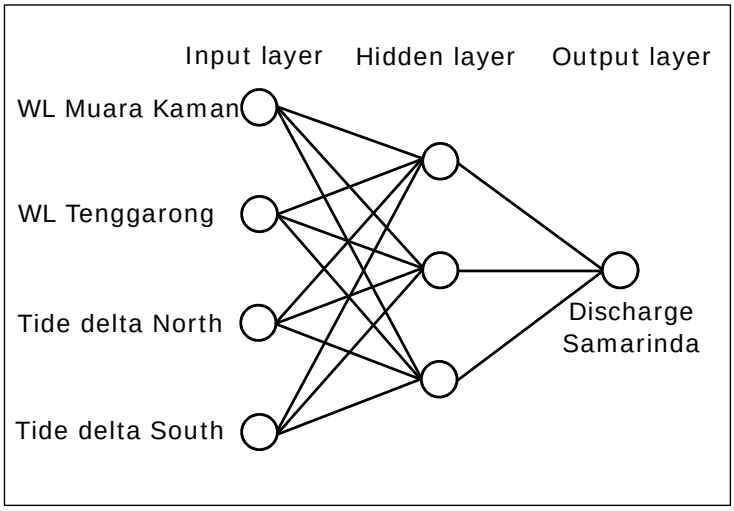

Figure 3.4: Schematic representation of water stage-discharge relationship at the H-ADCP station in Samarinda using upstream water level (WL) records and predicted tide levels at the Northern and at the Southern delta region.

nodes produces the highest correlation and the lowest error. The initial estimate from Eq. 3.2 was 4, confirming the formula can be used as a first guess.

Table 3.3 shows the performance of the alternative ANN-based hindcast models. Model hQ_3, using water level data from Tenggarong and Muara Kaman, predicted tide levels at the outer delta, and amplitudes of the diurnal, semi-diurnal quarter-diurnal tidal components of water level data in Tenggarong, produces the best model output with R^2 and NSE values amounting to 0.962 and 0.961, respectively. The RMSE value of 375 m^3s^{-1} is about 3% of the discharge range, exceeding 12200 m^3s^{-1}. Figure 3.6 shows scatter plots of the output of this model during the training and validation periods. Model hQ_3 produces a relatively consistent model performance during the two periods. Figure 3.7 shows the observed and modelled discharge during the validation period. The model fit is nearly perfect during average discharge conditions. During high- and low-flow conditions, however, several under- and over-estimations can be observed. The addition of the amplitude of tidal components of water level data for the upstream station in Muara Kaman results in a deterioration of the model performance in the validation, although the model performed well during the training period. Similar results were obtained when adding phases of the tidal components (not shown), indicating that too many input data can reduce the predictive skill of an ANN model.

These results show the application of neural networks in stage-discharge relationships in-tide dominated regions is promising, when water level data from multiple upstream and downstream stations are available. It is likely that an even better result would have been obtained with the use of water level data at the discharge station of interest, which was lacking due to malfunctioning of a pressure transducer. A potential application of this technique is that water agencies can install and maintain an H-ADCP for a limited amount of time, after which discharge can be obtained with an ANN model using only a small number of water level gauges. In the present case, a single level gauge and astronomical predictions at sea are sufficient.

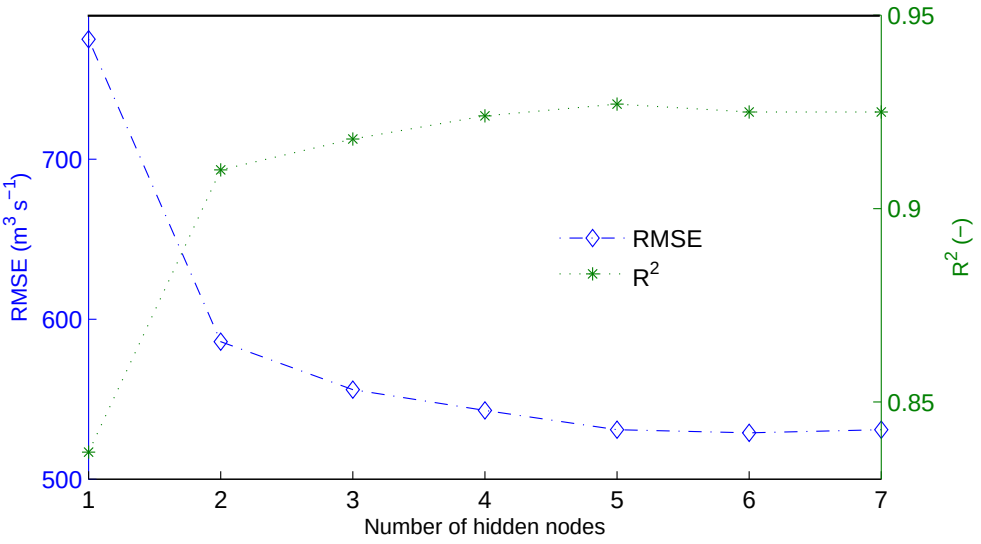

Figure 3.5: R^2 and RMSE (validation set) of model hQ_0 as a function of the number of hidden nodes.

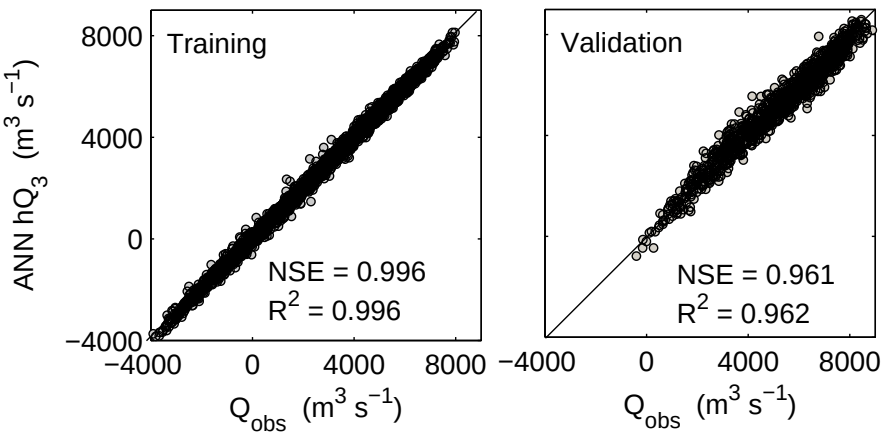

Figure 3.6: Scatter plots of the ANN model hQ_3 and observed data during training and validation periods.

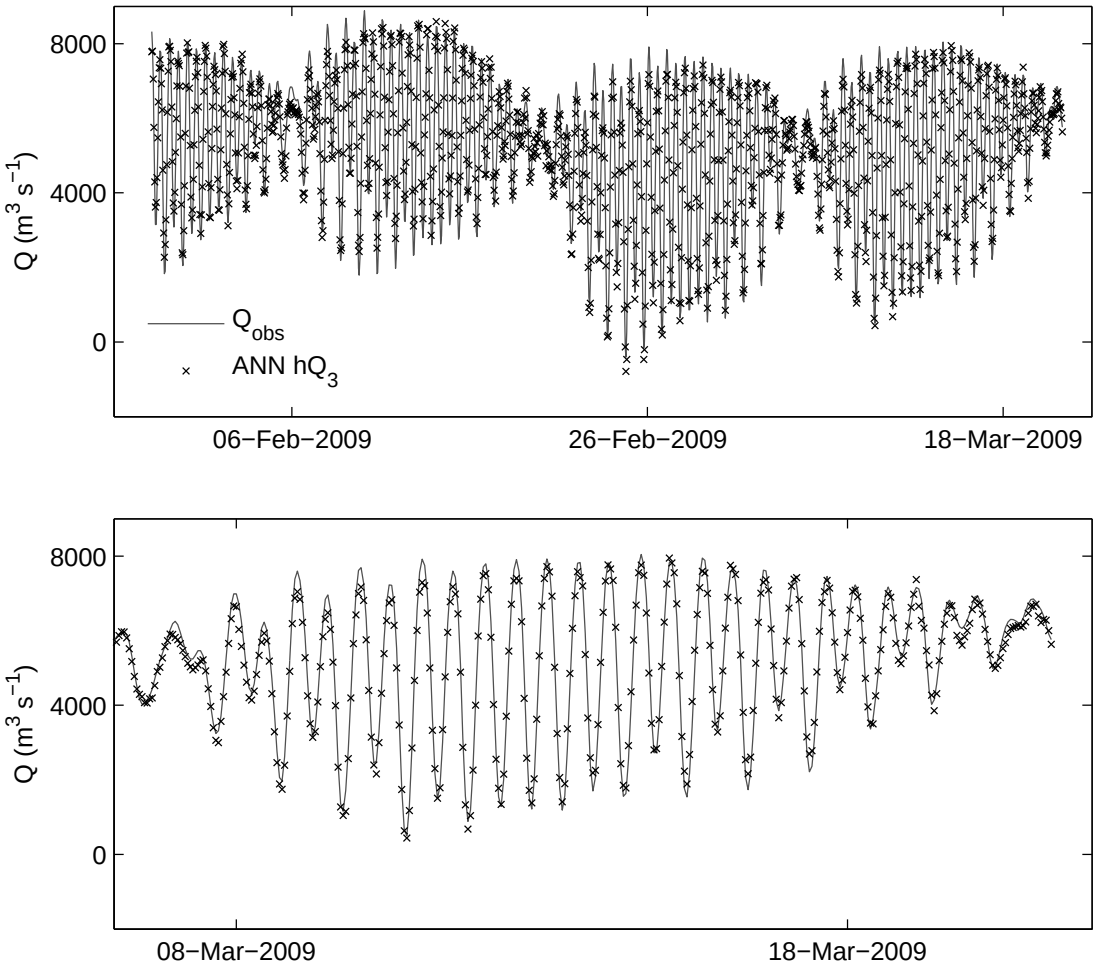

Figure 3.7: Observed and modeled discharge by the ANN model hQ_3 during the validation period (top). The same series zoomed into one neap-spring cycle (bottom).

Table 3.2: ANN model input configuration for discharge forecasting at Samarinda station, using at-site historical discharge data (Q_{Sm}), water levels at the upstream site in Tenggarong (h_{Tg}), TPXO predicted tide levels at the Northern and at the Southern outer delta (ζ_{Od}), water level of Lake Jempang (h_{Lj}), and discharge at the upstream site in Melak (Q_{Ml}). t is the time (hourly).

Model name	model input
Q_0	$Q = f\{Q_{Sm(t-1...t-3)}\}$
Q_1	$Q = f\{Q_{Sm(t-1...t-3)} + h_{Tg(t-1...t-6)}\}$
Q_2	$Q = f\{Q_{Sm(t-1...t-3)} + h_{Tg(t-1...t-6)} + \zeta_{Od(t-0...t-2)}\}$
Q_3	$Q = f\{Q_{Sm(t-1...t-3)} + h_{Tg(t-1...t-6)} + \zeta_{Od(t-0...t-2)} + h_{Lj(t-1)}\}$
Q_4	$Q = f\{Q_{Sm(t-1...t-3)} + h_{Tg(t-1...t-6)} + \zeta_{Od(t-0...t-2)} + h_{Lj(t-1)} + Q_{Ml(t-1)}\}$

Table 3.3: Performance of different ANN-based hindcast models for the validation dataset. R^2 (-) is the squared correlation coefficient, NSE (-) is Nash-Sutcliffe coefficient of Efficiency, RMSE (m^3s^{-1}) is Root Mean Square Error.

Model structure	R^2	NSE	RMSE
hQ_0	0.927	0.922	531
hQ_1	0.956	0.954	410
hQ_2	0.960	0.958	395
hQ_3	0.962	0.961	375
hQ_4	0.949	0.946	446

Similar to the case of traditional rating curve techniques, caution should be taken when physical changes in the river occur, such as a change in geometry because of sand mining or bank erosion. In this respect, regular updating with new H-ADCP measurements is required. Another possible application regards data gap filling of disrupted discharge time-series. Disruptions of continuous measurements due to, for instance, a technical failure or maintenance of the instruments may last for a period of days or weeks, in case of a remote area. A reliable continuous discharge data series can be assured by adding one or more water level gauge stations.

3.4.2 Discharge forecasting

Table 3.4 shows the performance of each of the alternative model configurations evaluated for predicting discharges ahead in time. Adding predicted tidal levels at the outer delta clearly improves model performance. The inclusion of lake water level data resulted in only a minor improvement. The predictive skills of the ANN models are highly dependent on the range of data provided in the model training. In experiments using shorter training datasets (not shown), the model failed to adequately predict water levels during the validation period.

Model Q_2, which is a relatively parsimonious model, produces a very low error (Fig. 3.8) with an RMSE value of 97 m^3s^{-1} , i.e. less than 1% of the discharge range. The inclusion of

Table 3.4: Performance of different models (validation set) using at-site historical discharge data as the main ANN model input. R^2 (-) is the coefficient of determination, NSE (-) is Nash-Sutcliffe coefficient of Efficiency, RMSE (m^3s^{-1}) is Root Mean Square Error.

Model structure	R^2	NSE	RMSE
Q_0	0.996	0.998	132
Q_1	0.997	0.997	121
Q_2	0.998	0.998	97
Q_3	0.998	0.998	97
Q_4	0.998	0.998	98

lake water levels and a more upstream discharge data set did not yield an appreciable effect on the model performance, reflecting the dominance of tides in the time-series.

We used the best performing model for a multi-step ahead prediction of discharge in Samarinda. Figure 3.9 shows scatter plots of discharge predictions for 1-day , 2-days, 3-days, and 4-days ahead in time. The ANN model produces good results over a relatively long prediction time horizon, as compared to previous studies (Supharatid, 2003; Sudheer and Jain, 2003; Bhattacharya and Solomatine, 2005). Figure 3.9 shows that the Q_2 model performs well up to 3-days ahead in time. For predictions exceeding 4-days ahead in time, the output becomes more scattered, especially under low discharge conditions.

3.5 Conclusions

Artificial neural networks (ANNs) can be employed to predict discharge from water level information in a lowland river where the tidal influence is apparent far inland. An ANN-based model was established to hindcast discharge at a station in Samarinda, using upstream water level data and astronomical predictions of tidal elevation at two locations at sea. The processing of the water level data based on a wavelet analysis, which yields diurnal, semidiurnal and quarter diurnal amplitudes and phases is included in the approach. The addition of the diurnal, semidiurnal and quarter diurnal amplitudes slightly improves model performance. With water levels from readily available predictions at sea, and those from a single station upstream of the target location, the ANN model produces consistent discharge estimations, even without at-site water level records. Next to hindcast predictions, discharge can be forecasted from ANNs. The added value of different sources of information was evaluated, including at-site historical discharges and water levels from lakes that are known to buffer the river discharge. Tidal elevation at sea, historical discharges and water levels from a single upstream station contributed significantly to the ability to forecast the discharge. Adding water level information from the lakes did not lengthen the prediction horizon, which may reflect the dominance of the tidal motion at the target site. A good performance was achieved for discharge predictions up to two days ahead, with NSE values exceeding 0.9.

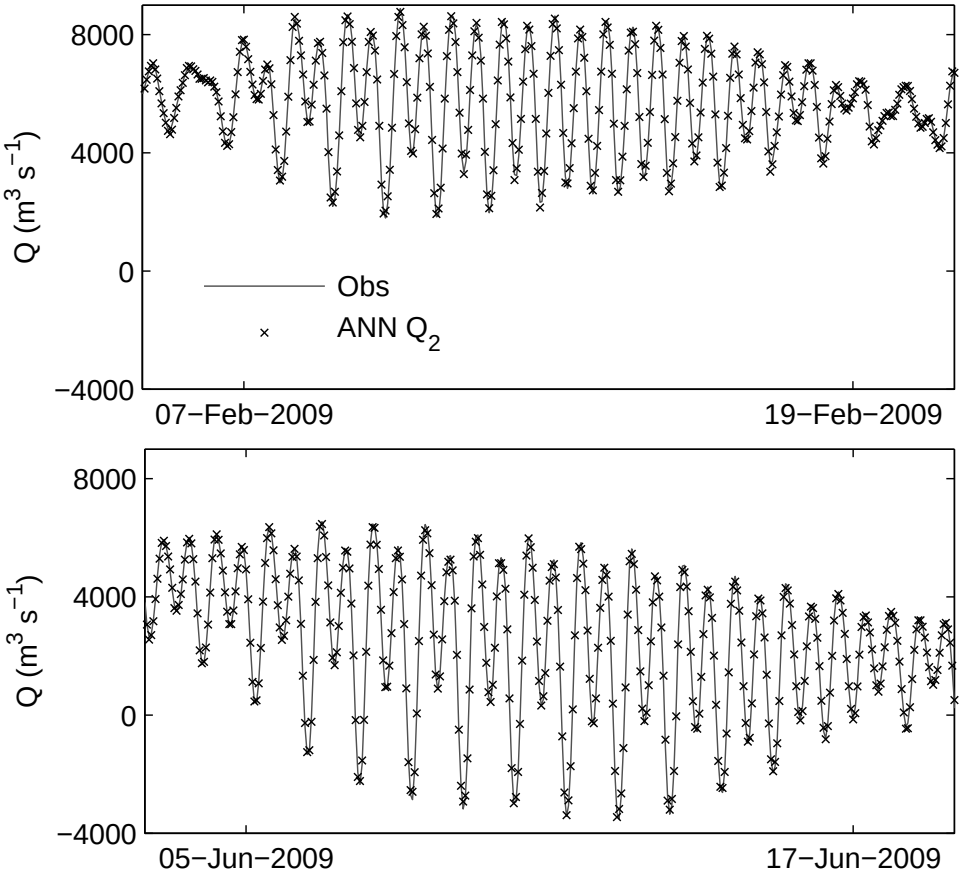

Figure 3.8: Discharge prediction by the Q_2 model during the validation period zoomed into one neap-spring cycle in February 2009 (top) and in June 2009 (bottom).

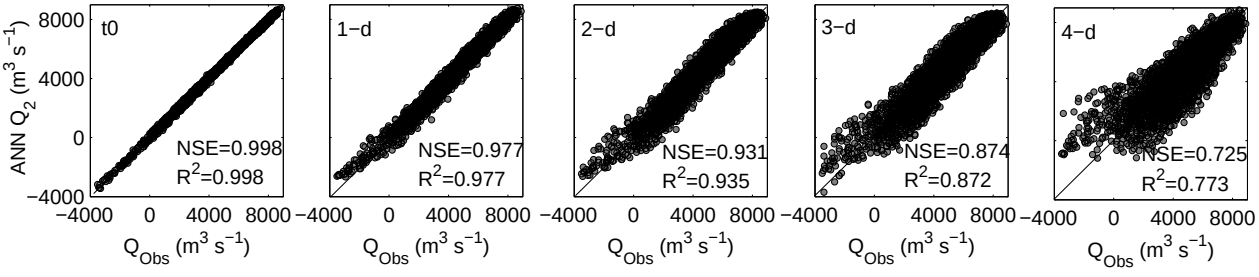

Figure 3.9: Performance of the discharge forecasts for 1-day, 2-days, 3-days, and 4-days ahead by the Q_2 model during the validation period. Diagonal lines indicate a 1:1 relation.

Chapter 4

Rainfall-runoff modeling of a poorly gauged tropical catchment

Abstract: Despite the importance of hydrological records, large regions of the world remain ungauged and the number of permanent gauge locations tends to decline worldwide. Therefore, building hydrological models in poorly gauged basins is a timely challenge. Discharge monitoring stations needed to calibrate a rainfall-runoff model cannot always be installed in headwaters where downstream controls on discharge are absent. The objective of this chapter is to quantify and discuss the discrepancies between alternative approaches to calibrate a rainfall-runoff model using discharge data subject to backwater effects. In the first approach, the model is calibrated using a continuous series of discharge derived from measurements with a horizontal acoustic Doppler current profiler (H-ADCP). In the second approach, the discharge estimates inferred from the H-ADCP data are used to derive a rating curve, which is in turn used to calibrate the rainfall-runoff model. The conceptual rainfall-runoff model, implemented on the basis of HBV, represents the Mahakam sub-catchment upstream of Melak (25700 km^2), which marks the transition of a lowland area with the central rainforest of Kalimantan. The HBV model was forced by Tropical Rainfall Measuring Mission (TRMM) rainfall estimates. We find a comparatively low model efficiency adopting the first calibration approach using the original discharge time-series, which is attributed to the backwater effects that are not captured by the rainfall-runoff model. The calibration approach using the rating curve produces a relatively higher model efficiency, since the rating curve filters the backwater effects from the discharge series. Discharge simulations from an ensemble mean of the model output using the 20 best parameter sets selected based on a fuzzy measure show a consistent performance during both the calibration and validation periods. The model was then used to simulate discharge outside the calibration and validation periods. Seasonal variation of terms in the water balance were not affected by the choice of one of the two calibration strategies, which shows that backwaters do not have a systematic seasonal effect on the river discharge.

This chapter is based on: Hidayat, H., Hoitink, A.J.F., Sassi, M.G., Vermeulen, B., Torfs, P.J.J.F., Uijlenhoet, R.: Rating curve for the Mahakam River relates river stage to runoff rather than to discharge, To be resubmitted to Water Resour. Res.

4.1 Introduction

Rainfall-runoff models are being extensively used in hydrological studies, becoming standard tools to study the water balance, to forecast stream flow, and to predict how scenarios of climate change and land use development will impact river discharge (e.g. Wagener et al., 2004b; Todini, 2007; Seibert and Beven, 2009; Beven, 2012). Singh and Woolhiser (2002), among others, provided a comprehensive review of the development of mathematical modelling of watershed hydrology, discussing over 70 popular models. In rainfall-runoff modelling studies, discharge is generally treated as a variable that, when available, is known with a relatively high degree of accuracy. Indeed, discharge monitoring techniques have improved over the past decades (Le Coz et al., 2008; Hauet et al., 2008; Hoitink et al., 2009; Sassi et al., 2011; Bechle et al., 2012; Kawanisi et al., 2012), such that discharge estimates can be accurate even without an expensive discharge measurement structure. Discharge monitoring stations are not always located in headwaters where backwater effects are absent. The outlets of catchments are often located in lowland areas, where backwater effects of lakes, tributaries and floodplains, as well as tidal effects may be present. A discharge monitoring location closer to the outlet has the advantage that it represents a larger part of the catchment all at once, whereas at locations further upstream, discharge variations can be easier related to rainfall. Hydrological models calculate runoff, i.e. the amount of water ending up in the river, usually by including only a simple routing scheme. The actual hydraulic conditions may be much more complex, for instance, due to backwater effects, that may generate a difference between the calculated runoff and the measured discharge.

Discharges in a river differ from runoff because runoff is not instantaneously being discharged by the river. The causes of spatial and temporal lags can be subdivided into nonlinear wave effects and interactions between elementary units in a surface water systems, which include tributaries, lakes, ponds and floodplains. The consequences of the latter interactions for discharges, which are particularly relevant in lowland regions, are generally being referred to as backwater effects. Whereas nonlinear wave effects can be captured in a single-spot rating curve using Jones's formula, accounting for backwater effects requires either an array of monitoring stations, or the use of a hydraulic model. Hidayat et al. (2011b) showed that rating curves may fail even after accounting for nonlinear wave effects using Jones' formula. Here we address the issue of rainfall-runoff modelling based on discharge data which are influenced by backwater effects. We show that under such circumstances, it may be better to train the model with discharge series derived from a rating curve, since rating curves do not capture the backwater effects and therefore may better reflect the discharge variation in response to rainfall.

Among many model options, the HBV (Hydrologiska Byrans Vattenbalansavdelning) model (Bergstrom, 1995) is one of those suitable for water balance studies and predictions in ungauged basins. It is a conceptual rainfall-runoff model, which simulates discharge using rainfall, temperature and estimates of potential evaporation (Seibert, 1997). The model has been widely used for stream flow simulation, flow forecasting, and hydrological process studies (e.g. Driessen et al., 2010; Hazenberg et al., 2011). The present study uses the HBV model for rainfall-runoff modelling of the Mahakam in East Kalimantan (Fig. 4.1).

The River Mahakam exemplifies a data poor environment in the tropics, with a catchment that comprises an extensive area of tropical rain forest. Despite the river's importance to people

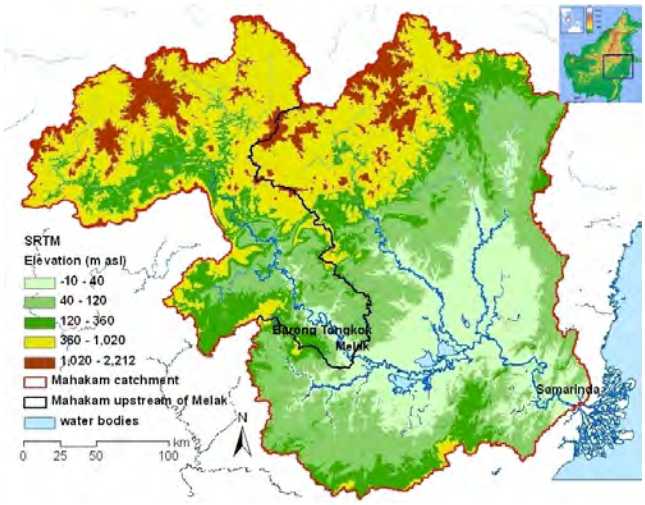

Figure 4.1: The Mahakam catchment in East Kalimantan delineated using the SRTM digital elevation model.

and the environment, few hydrological studies have been conducted in this region. One option for enabling predictions at an ungauged site starts by taking discharge measurements, exploiting the new generation of acoustic Doppler velocity measurements (Seibert and Beven, 2009). Using monitored catchments as hypothetical ungauged basins by initially constraining a simple catchment model with no runoff data, and then adding different sub-sets of the available data, Seibert and Beven (2009) found that ensemble prediction outperformed predictions using single parameter sets. Only a short time-series of discharge was necessary to identify model parameters that produced good results for the test period treated as ungauged. To enable setting up a rainfall-runoff model of the Mahakam catchment, an H-ADCP discharge monitoring station was established in Melak, to become operational in the period between April 2008 and August 2009. Melak can be considered the most upstream city along the Mahakam River accessible by road, marking the transition to the pristine tropical rain forest of central part of Kalimantan. Hidayat et al. (2011b) showed that the monitoring station is severely impacted by backwater effects. The objective of this chapter is to quantify and discuss the discrepancies between the use of a rating curve and continuous discharge estimates from the H-ADCP monitoring station with regard to rainfall-runoff modelling of the headwaters of the Mahakam River.

The recent trend in the availability of remotely-sensed data has led in large parts of the globe to a change from a data-poor to a data-rich environment (Bates, 2004). Climate forcing data from satellite remote sensing provides alternative solutions in filling the gaps in data-scarce regions. Spaceborne radar and radiometers provide a potential means of obtaining rainfall estimates with a large coverage area. The availability of satellite-based rainfall estimates provides useful information for a sparsely gauged area such as Kalimantan. TRMM-based precipitation estimates have been available to the research community since the satellite was launched in November 1997. TRMM multi-satellite precipitation analysis (TMPA) rainfall estimates have been reported to be valuable as an alternative source of rainfall information in hydrological studies (Wilk et al., 2006; Huffman et al., 2007; Su et al., 2007; Villarini and Krajewski, 2007; Collischonn et al., 2008).

The remainder of the chapter is arranged as follows. Section 4.2 describes the field site and data gathering in the Mahakam catchment. Section 4.3 describes the setup and calibration of the rainfall-runoff model. Section 4.4 presents a TRMM data analysis. Section 4.5 presents results from model evaluation and discharge simulations beyond the calibration and validation periods. In Sections 4.5, results obtained using H-ADCP discharge estimates or alternatively a rating curve are being presented in parallel, which is followed by a discussion in Section 4.6. Finally, in Section 4.7, conclusions are drawn.

4.2 Data Collection

Data collection was carried out by taking field measurements and by collecting available data from different sources. From March 2008 to August 2009, we carried out horizontal acoustic Doppler current profiler (H-ADCP) measurements in Melak, just upstream of the lakes region. Discharge estimation from continuous H-ADCP data for Melak as well as those obtained using the rating curve method based on a number of ADCP discharge surveys are reported in Hidayat et al. (2011b). Temperature, wind speed, and relative humidity data (available nearly continuously for the period between 2001 and 2008) were obtained from an existing automatic weather station in Barong Tongkok, a sub-district upstream of Melak. The mean air temperature slightly fluctuates around a mean value of 25.7°C during the whole year (Fig. 4.2). Therefore, it is reasonable to use a constant mean air temperature value as an approximation for the period with no available temperature data. The evapotranspiration rate was estimated using the Penman-Monteith method (see e.g. Ventura et al., 1999). Rainfall records from previously installed rain gauges were also collected. The TRMM data were acquired from NASA's Goddard Earth Sciences Data and Information Services Center Interactive Online Visualization and Analysis Infrastructure (Giovanni) internet site. The estimates are provided on a global 0.25° x 0.25° grid over the latitude band 50°N-S within about seven hours of observation time. The digital elevation model (DEM) used for catchment delineation in this study was a freely available DEM derived from NASA SRTM (Shuttle Radar Topography Mission), with a 90-m spatial resolution (Jarvis et al., 2008). Two ENSO indices, the Southern Oscillation Index (SOI; computed from fluctuations in the surface air pressure difference between Tahiti and Darwin), and the Multivariate ENSO Index (MEI; computed from six variables over the tropical Pacific including sea-level pressure, zonal and meridional components of the surface wind, sea surface temperature, surface air temperature, and total cloudiness fraction of the sky) were obtained from the National Oceanic and Atmospheric Administration website (NOAA, 2012a,b).

4.3 Model Setup and Calibration

We applied the HBV model with lumped input for rainfall-runoff modelling of the Mahakam sub-catchment upstream of Melak (25700 km^2). The latter region is the largest sub-catchment contributing to the Mahakam River, containing the headwaters of the main river. We chose to model this sub-catchment instead of the entire catchment, because the outlet is a tidal river where tidal discharges overwhelm the contribution by the river. The HBV model is a conceptual model that consists of different routines representing precipitation, soil water and

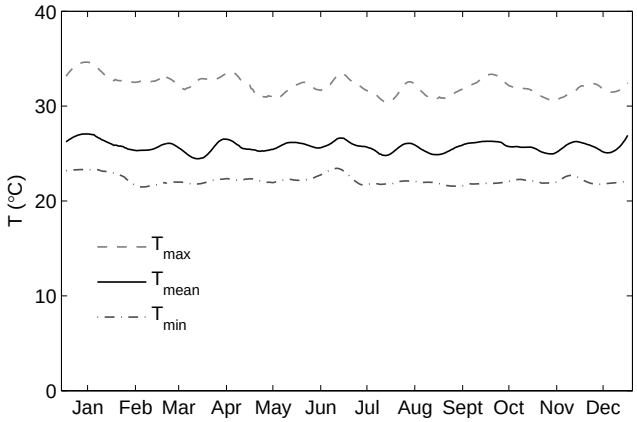

Figure 4.2: Daily mean, minimum, and maximum air temperature at Barong Tongkok (about 20 km upstream of Melak) for 2007.

evaporation, groundwater using three linear reservoir equations, and channel routing using a triangular weighting function (see e.g. Bergstrom, 1995; Seibert, 1997). The model used in this study is the HBV Light version (Seibert, 1997; Seibert et al., 2000; Seibert and McDonnell, 2010), which is a modification of the original HBV model described by Bergstrom (1995). This version of the model uses a warming-up period, a period during which rough estimates of the initial state values progress into their proper values according to the atmospheric forcing and model parameter values. All parameters in the model have a physical interpretation (see Table 4.1), but since they represent effective values at the catchment scale, they are not measurable and need calibration.

The time-series of discharge were interrupted twice, splitting the H-ADCP measurement period in three parts. Estimates between 16 October 2008 through 15 July 2009 were used for model calibration. The second, shorter continuous daily discharge data set covering the period between 1 May through 13 July 2008 served for validation. Discharge data between 19 March through 30 April 2008 were used to warm-up the model. The same setup was adopted to warm-up, calibrate and validate the rainfall-runoff model based on rating curve estimates of discharge, using the water levels at Melak in the corresponding periods.

Model performance was evaluated using the Nash-Sutcliffe (NSE) coefficient (Nash and Sutcliffe, 1970):

$$NSE = 1 - \frac{\Sigma_{t=1}^{n}[Q_{obs}(t) - Q_{sim}(t)]^2}{\Sigma_{t=1}^{n}[Q_{obs}(t) - \bar{Q}_{obs}]^2} \tag{4.1}$$

where $Q_{obs}(t)$ and $Q_{sim}(t)$ correspond to observed and calculated discharge at time t, $\bar{Q}_{obs}$ is the average observed discharge, and n is the total number of time steps.

The input data for the model were daily rainfall, and potential evaporation. Daily TMPA rainfall estimates over the Mahakam catchment upstream of Melak were averaged and were combined with temperature and measured discharge to force and evaluate the model. Estimates of evapotranspiration were provided as an average monthly reference evapotranspiration. The model was run in a standard model structure mode and calibrated by a Monte Carlo run of one million parameters sets generated using random numbers from a uniform distribution within

the range of possible minimum and maximum parameter values (Seibert, 1997; Seibert and McDonnell, 2010).

We follow the approach by Seibert and Beven (2009) in using ensemble means for discharge simulation using the HBV model. The NSE and fuzzy measures were used to choose the twenty best parameter sets. Using NSE as an objective function, the performance for the alternative parameter sets were ranked and the best 20 sets were selected for further analysis. The fuzzy measure was implemented following Seibert (1997), using fuzzy logic to handle the concept of a partial truth value, in between completely true and completely false. The fuzzy measure allows different objective functions to be joined and to compute the degree of truth of the best possible set statement, F, for each parameter set:

$$F = X_1 \cap ... \cap X_5 = \min(X_i) \quad i = 1, ..., 5, \tag{4.2}$$

where

$$X_i = \max\left(0, \frac{R_i - 0.8R_i, max}{0.2R_i, \max}\right) \quad i = 1, 2, 3, 4, 5, \tag{4.3}$$

with R_i being one of five computed efficiency factors, including NSE, log(NSE), coefficient of determination (R^2), mean absolute relative error (MARE), and Lindstrom measure (L_{meas}) (Lindstrom, 1997). A series of simulated runoff was computed as weighted ensemble mean based on the ensemble of 20 runoff simulations:

$$\left\langle Q_{(t)} \right\rangle = \sum_{i=1}^{20} w_i Q_i(t), \tag{4.4}$$

where the brackets denote an ensemble average. The weights w_i were taken from a linear decreasing function so that the best parameter set according to respectively the fuzzy measure or NSE criteria received a weight of 0.1 and the 20th parameter set received a weight of zero. The sum of weights is such that

$$\sum_{i=1}^{20} w_i = 1. \tag{4.5}$$

4.4 TRMM Data Analysis

TRMM multi satellite precipitation analysis (TMPA) is a precipitation product that combines observations from multiple satellites, as well as gauge analyses where available. A comprehensive description of the TMPA can be found in Huffman et al. (2007). The real time (RT) and retrospective (research) rainfall products have been available since 1998. Vernimmen et al. (2012) report on a comparison of the real-time TMPA RT product with other satellite rainfall estimates (the Climate Prediction Center morphing method CMORPH and the Precipitation Estimation from Remotely Sensed Information Using Neural Networks PERSIANN) with rain gauge records over Indonesia. Using data from 76 ground stations in Java, Sumatra, and Kalimantan, they found that generally the TRMM 3B42RT product is more accurate than the

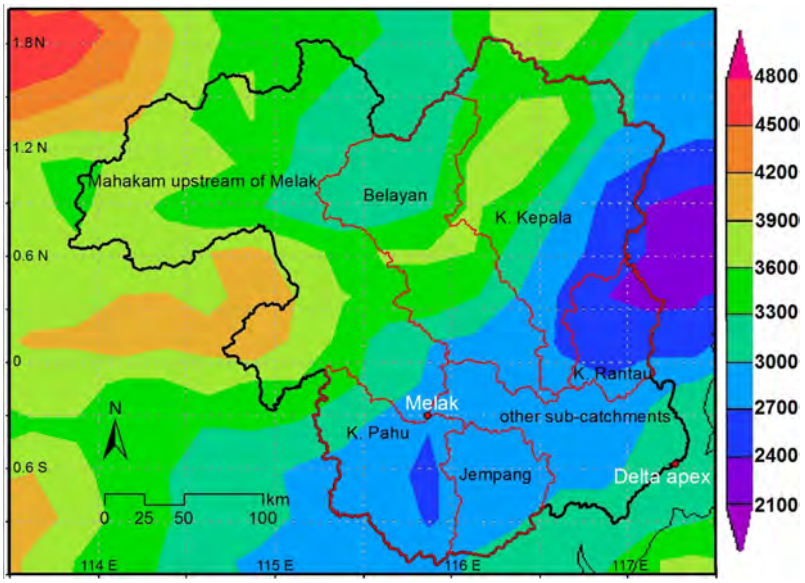

Figure 4.3: Spatial distribution of accumulated rainfall (mm) over the study area for 2008 derived from TMPA version 6 3B42 rainfall estimates. The bold black line indicates the Mahakam catchment boundary, red lines indicate boundaries of main sub-catchments.

other two products, and resembles patterns in ground stations closely. However, they also noted that the TRMM 3B42RT rainfall products consistently underestimate rainfall during the dry months and overestimate rainfall in wet months. Vernimmen et al. (2012) adopted a bias correction approach to improve the monthly TMPA 3B42RT precipitation estimates, but the improvement was found to be rather marginal. For the Banjar Baru ground stations in South Kalimantan, being closest to the Mahakam, the bias correction yielded a root mean square error reduction of 6% and a correlation coefficient increase of only 1%.

The research TMPA version 6 products 3B42 three-hourly, 3B42 daily, and 3B43 monthly were used in the analysis of rainfall over the Mahakam catchment. Figure 4.3 shows the spatial distribution of accumulated rainfall in the Mahakam catchment for 2008 based on the TMPA version 6 3B42 rainfall estimates. High rainfall depths occurred in the mountainous areas upstream of the River Mahakam. Relatively lower rainfall accumulations occurred in the lowlands of the middle Mahakam area.

We compared the TMPA rainfall estimates with rain gauge measurements available at seven locations along the Mahakam River. The rainfall estimates were evaluated at daily and monthly time scales for the periods between 1998-2002, when reliable rain gauge data were available. Comparing estimates from a single grid point of the daily TMPA with corresponding rain gauge data from Barong Tongkok weather station gave a low correlation (R^2=0.31). A higher correlation was obtained at 10-day (R^2=0.61) and monthly (R^2=0.66) time scales (Fig. 4.4). Figure 4.5 compares monthly accumulated TMPA estimates with corresponding rain gauge data from six locations between Melak and the Mahakam delta apex (Melak, Kotabangun, Tenggarong, Sebulu, Samarinda, and Telukdalam) for the period 1998–2002. The 3B43 monthly product features an underestimation of the rain rates for the six locations. Except for February, the monthly accumulated 3B42 daily product provides a better agreement with the rain gauges.

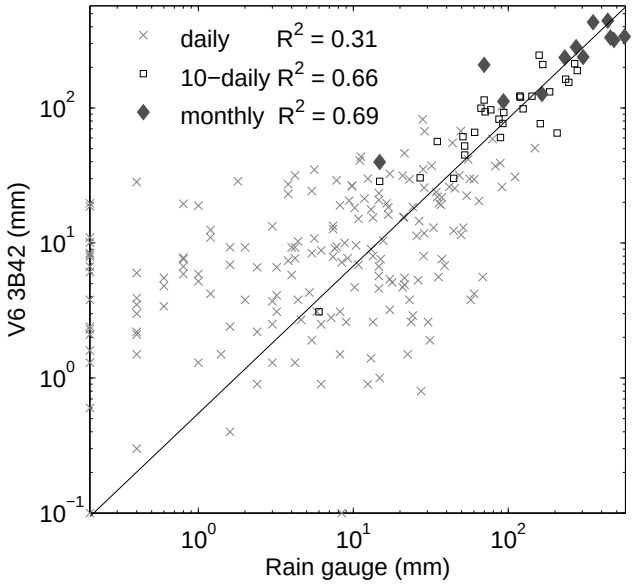

Figure 4.4: TMPA version 6 3B42 versus rain gauge records for daily, 10-daily, and monthly time averages at the Barong Tongkok weather station in 2001. The squares of the correlation coefficients for all aggregation periods are displayed as R^2 values in the upper left corner. The diagonal line indicates a 1:1 relation.

Therefore, the 3B42 rainfall estimates were chosen to evaluate rainfall patterns over the Mahakam sub-catchment upstream of Melak. The thirteen-year record of TRMM 3B42 rainfall estimates confirms the rainfall pattern over the Mahakam catchment area to be bimodal, with average annual rainfall sums of 3000 mm (Fig. 4.6, top panel). The rainfall peaks occur in November through December and in March through April.

Rainfall patterns in Kalimantan are highly influenced by ENSO and the Indo-Pacific air-sea interaction. Drought conditions during the dry season generally relate to the development of El-Niño in the Pacific, when anomalously cold Sea Surface Temperature (SST) surrounds Indonesia while warm anomalies develop in the eastern Pacific and western Indian Ocean (Hendon, 2003). On the contrary, increased rainfall during the dry season occurs during the development of a La Niña event, when SST anomalies opposite to those during an El-Niño event occur. The effect of ENSO, however, is not uniform throughout the seasons. Hendon (2003) found that rainfall anomalies in Indonesia tend to persist in the dry season but not in the wet season. Figure 4.6 (bottom panel) shows the correlation between SOI and TRMM 3B42 monthly accumulated rainfall from 1998 through 2010 over the Mahakam catchment section upstream of Melak. Generally, a higher (lower) correlation is obtained during the dry (wet) season. This result agrees with the conclusions drawn by Haylock and McBride (2001), based on the analysis of SOI and rainfall in 63 stations across Indonesia from 1950 to 1998. Haylock and McBride (2001) argue that the most predictable rainfall in the region is during the dry season, and vice versa. The effect of La Niña in enhancing rainfall is not as strong as that of El-Niño in reducing rainfall over the Mahakam catchment. Figure 4.7 illustrates ENSO impacts on rainfall over East Kalimantan for January 1998, 2000, 2002. Rainfall in January 1998, which corresponds to a strong El-Niño, is significantly lower than the rainfall in January 2000, characterized by a

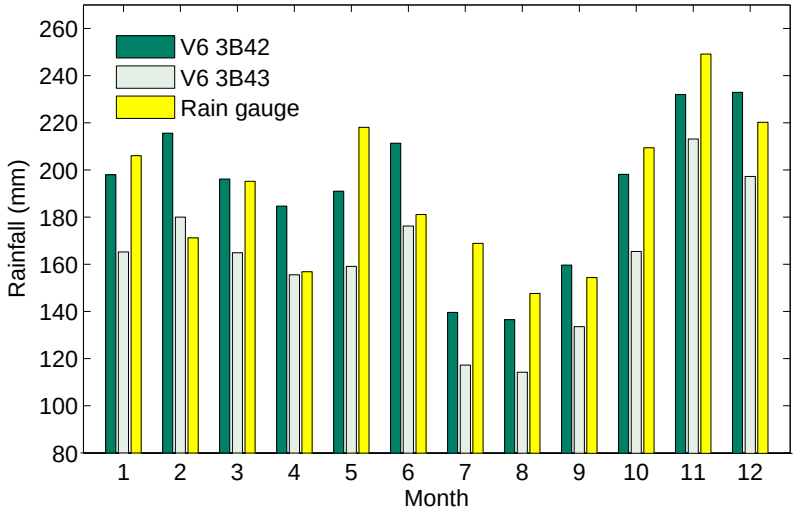

Figure 4.5: Comparison of TMPA rainfall estimates and ensemble mean of monthly rain rate of six rain gauges located between Melak and the Mahakam delta apex for 1998–2002.

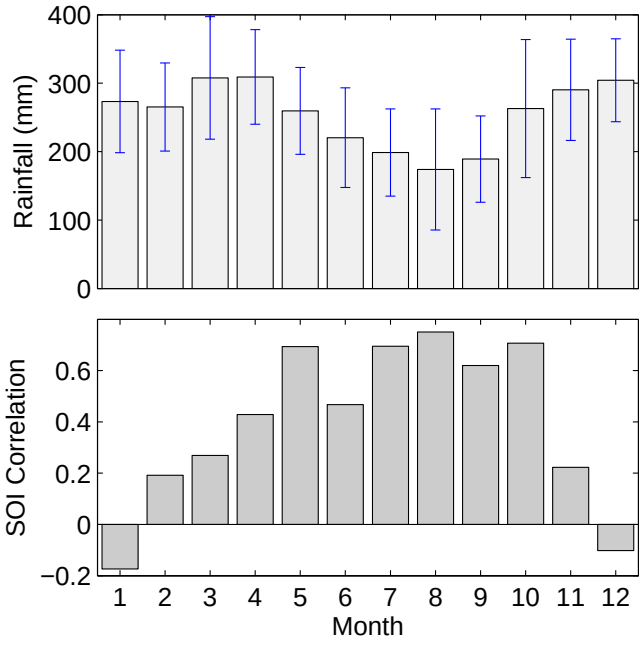

Figure 4.6: Accumulated monthly rainfall averaged over the sub-catchment of the Mahakam upstream of Melak from TRMM 3B42 for 1998–2010 (top) and the respective correlation with SOI (Southern Oscillation Index, bottom). Error bars on the top panel indicate one standard deviation above and below average.

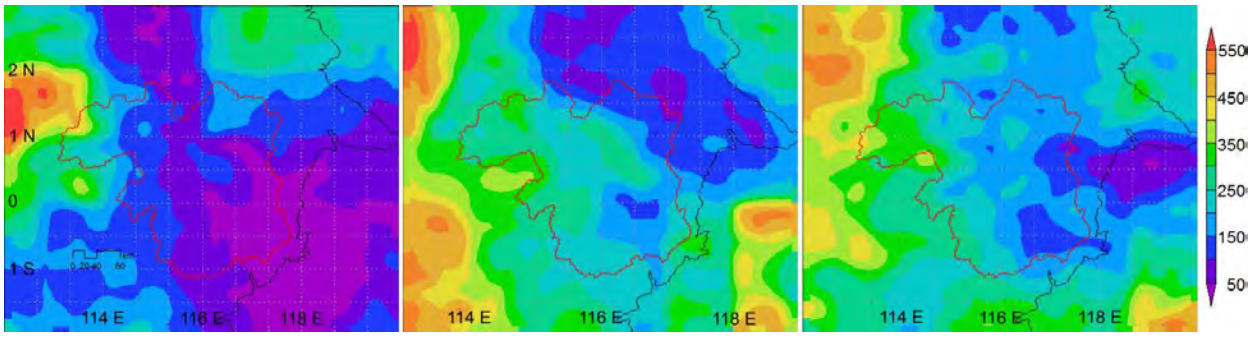

Figure 4.7: Rainfall estimates (mm) from TMPA 3B43 over East Kalimantan for January of 1998 (left), 2000 (middle), 2002 (right) that are respectively classified as El-Niño, La-Niña, and neutral periods. Black lines indicate the coast-line, red lines indicate the Mahakam catchment boundary.

strong La-Niña, and January 2002, which is in a period when the ENSO index is neutral. The latter two periods show a comparable rainfall intensity.

4.5 Results

4.5.1 Model Evaluation

The HBV model performed markedly different when daily discharge data from H-ADCP measurements were used for calibration, instead of estimates from the rating curve. Table 4.1 presents ranges of the HBV parameter values and the optimal parameter set. Overall, a higher model efficiency was obtained for the model calibrated using discharge data from the rating curve. Table 4.2 shows the evaluation of the model performance based on the 20 best NSE and fuzzy measures. Figure 4.8 shows dotty plots of the objective function used in the fuzzy measure as a function of the calibrated parameters, and the corresponding evaluation results F. Calibration with discharge data obtained from the rating curve method resulted in a large number of parameter sets with NSE>0. In the fuzzy measure evaluation, parameters are found to be well-defined. Discharge simulation from an ensemble mean of the model output using the 20 best parameter sets, selected based on the fuzzy measure, gives a consistent performance during both the calibration and the validation period, yielding NSEs of 0.61 and 0.62, respectively. This is more or less comparable with the result obtained by Su et al. (2007), who obtained an NSE of 0.45 for hydrologic prediction in the Iguazu catchment (62200 km^2) using a semi-distributed model forced by TRMM rainfall estimates. Cross-validation was carried out by validating the HBV model calibrated using H-ADCP discharge estimates by those obtained using the rating curve, and vice versa. The result shows that the model calibrated using the original discharge estimates based on the H-ADCP data had a higher coefficient of efficiency when it was validated using discharge series from the rating curve. This is mainly because the model calibrated using the original discharge estimates does not properly reproduce the low flow in the observed discharges from H-ADCP data, and the simulated discharge is closer to discharge estimates obtained using the rating curve.

Table 4.1: Calibrated HBV model parameters, their realistic ranges (Seibert, 1997) and range of the corresponding parameters for the 20 best simulations, based on the NSE, from calibration both with discharge estimates from H-ADCP data and with those from the rating curve.

Parameter	Possible range	$Range_{H-ADCP}$	$Range_{RC}$
Maximum of soil moisture storage: FC (mm)	50–500	331–499	353–486
Threshold for evaporation reduction: LP (-)	0.3–1	0.31–0.84	0.32–0.77
Shape coefficient: $BETA$ (-)	1–6	1.1–2.1	1–2
Recession coefficient (upper storage): K_0 (d^{-1})	0.05–0.5	0.06–0.46	0.05–0.5
Recession coefficient (upper storage): K_1 (d^{-1})	0.01–0.3	0.08–0.14	0.06–0.08
Recession coefficient (lower storage): K_2 (d^{-1})	0.001-0.1	0.001–0.01	0.009–0.1
Threshold for K_0-outflow : UZL (mm)	0–100	56–98.4	81.4–99.9
Maximum percolation: $PERC$ (mmd^{-1})	0–6	5.4–6	3.7–6
Routing parameter: $MAXBAS$ (d)	1–5	1.8–5	1.9–5

Table 4.2: Nash-Sutcliffe Efficiency (NSE) of the HBV model calibrated with different discharge data sources. The calculation is based on the ensemble mean of simulated discharges from the twenty best parameter sets from the evaluation using the NSE and the fuzzy measure (FM). 'Cross Val' stands for validation of the model calibrated using discharge series from H-ADCP data with those from the rating curve and vice versa.

Discharge data source	Cal_{NSE}	Val_{NSE}	$CrossVal_{NSE}$	Cal_{FM}	Val_{FM}	$CrossVal_{FM}$
H-ADCP	0.42	0.48	0.56	0.15	0.44	0.70
Rating curve	0.76	0.49	0.29	0.61	0.62	0.20

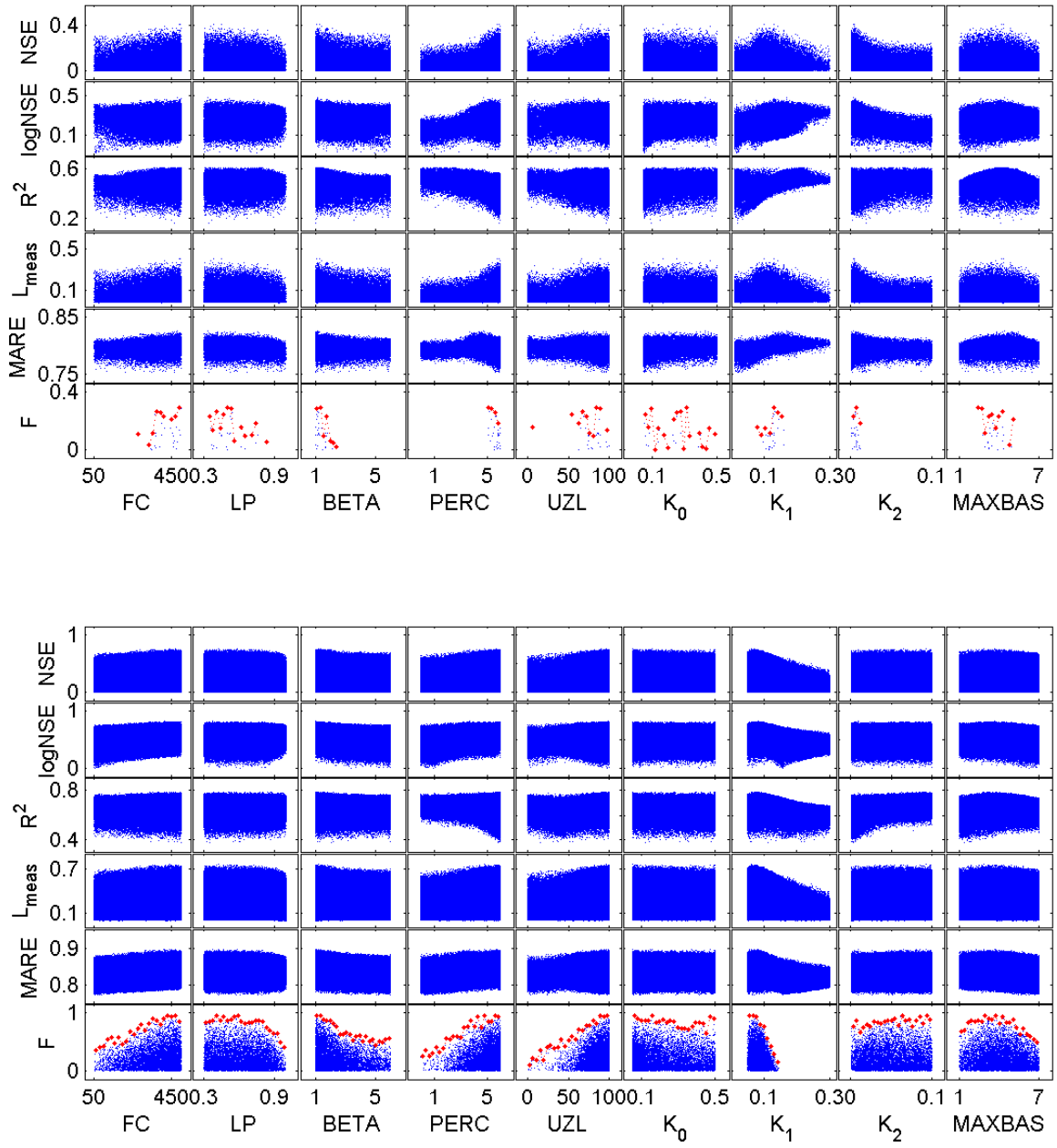

Figure 4.8: Dotty plots of different objective functions as a function of HBV model parameters calibrated using discharge series from H-ADCP data (top) and those obtained from the rating curve (bottom). The red upper boundaries on F-plots define the best parameter set obtained from the fuzzy measure.

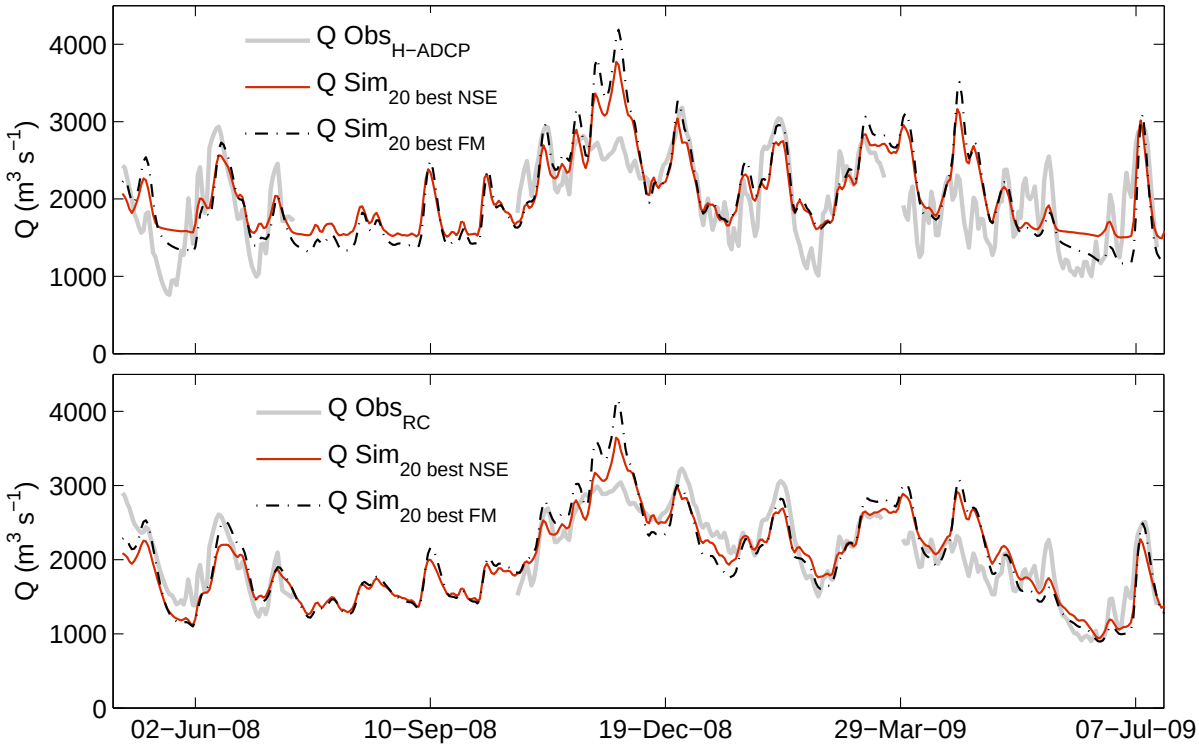

Figure 4.9: Discharge simulation for Melak as an ensemble mean discharge (based on NSE and fuzzy measure) obtained from the HBV model calibrated by discharge estimates from H-ADCP data (top) and those from the rating curve (bottom). The model was calibrated by discharge data between 16 October 2008 through 15 July 2009. Discharge data between 1 May through 13 July 2008 were used for validation.

Figure 4.9 shows time-series of the discharge simulations. The simulated discharge during the period from December 2008 through April 2009 agrees well with the observed discharges. The largest disagreement occurs in May 2009 and in November 2008. Huffman and Bolvin (2009) reported on an anomaly in the TRMM precipitation radar estimates in late May 2009, which may explain model overestimation in that period. There is no direct record of an anomaly in the TRMM dataset that could explain the discrepancy during the discharge peak in November 2008. From an evaluation of basin-averaged rain rates obtained from TMPA and rain gauge estimates over the La Plata basin, Su et al. (2007) pointed out that TMPA tends to overestimate most of the high rain rates at daily time scales, which seems to be confirmed by our results. Considering the spatial rainfall variability and the variation in land cover types, the overestimation may partly be due to a poor representation of the sub-catchment model.

4.5.2 Catchment Water Balance and Extreme Discharge Conditions

Using the twenty best parameter sets selected based on the fuzzy measure during the calibration period, we run the model for an extended period to gain insight into catchment behavior, and to investigate how the choice for one of the two calibration strategies, based on the original discharge series or estimates from a rating curve, exerts an influence on discharge hindcasts.

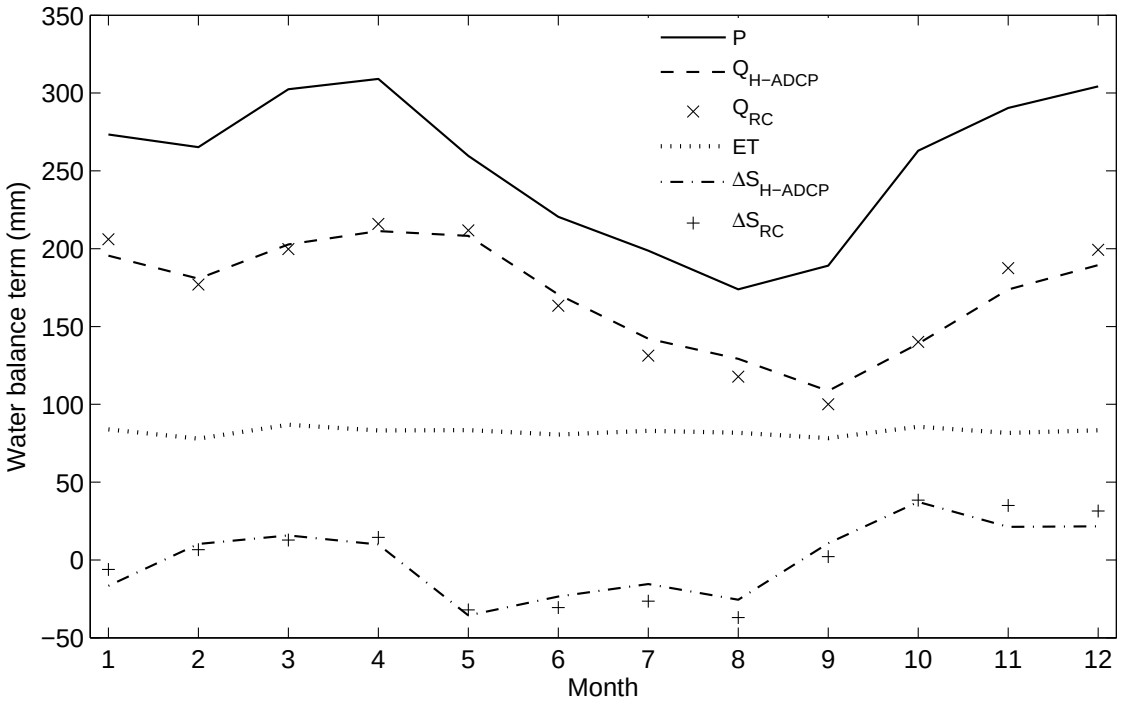

Figure 4.10: Seasonal water balance of the Mahakam upstream of Melak ($P = Q + ET + \Delta S$). Monthly sums of precipitation P, discharge Q, actual evapotranspiration ET, and storage change ΔS are averaged over the HBV model simulation period of January 1998 – December 2009. Subscripts indicate the two sets of discharge time series used to calibrate the model.

Figure 4.10 shows the seasonal water balance of the Mahakam catchment upstream of Melak averaged over a simulation period from January 1998 through December 2010, which is the period for which TRMM data was available. Since the Mahakam is a rain-fed river, the mean monthly discharge sums at Melak follow the bimodal trend in precipitation, with a time lag. The mean monthly actual evapotranspiration sums are nearly constant, which is a typical feature in the humid tropics where temperature is almost constant over the year. The storage change term, which oscillates within the range between plus or minus half the value of the evaporation term, represents the ground water storage change. During the dry season, the storage change term is negative, which means that part of the water from the soil is being extracted for evapotranspiration. The severe drought during the early 1998 ENSO event contributes strongly to the negative sums of storage change in January.

Figure 4.11 presents the continuous hindcast series of discharge, exploring the relation between river flow and two ENSO indices. Using the rating curve based model estimates, the correlation coefficient for discharge and SOI is 0.3. The highest discharges of the Mahakam generally occur during the cold phase of ENSO, when SOI is positive, while low discharges generally occur during the warm phase of ENSO when SOI is negative. The opposite trend with a negative correlation (r = -0.3) is obtained from a direct correlation between discharge and MEI. During the strong El Niño event in the first half of 1998, the model shows a long lasting low-flow event. Towards the end of 2002, which is classified by Wolter and Timlin (2011) as a moderate El Niño event, the discharge simulation shows a less severe low flow condition.

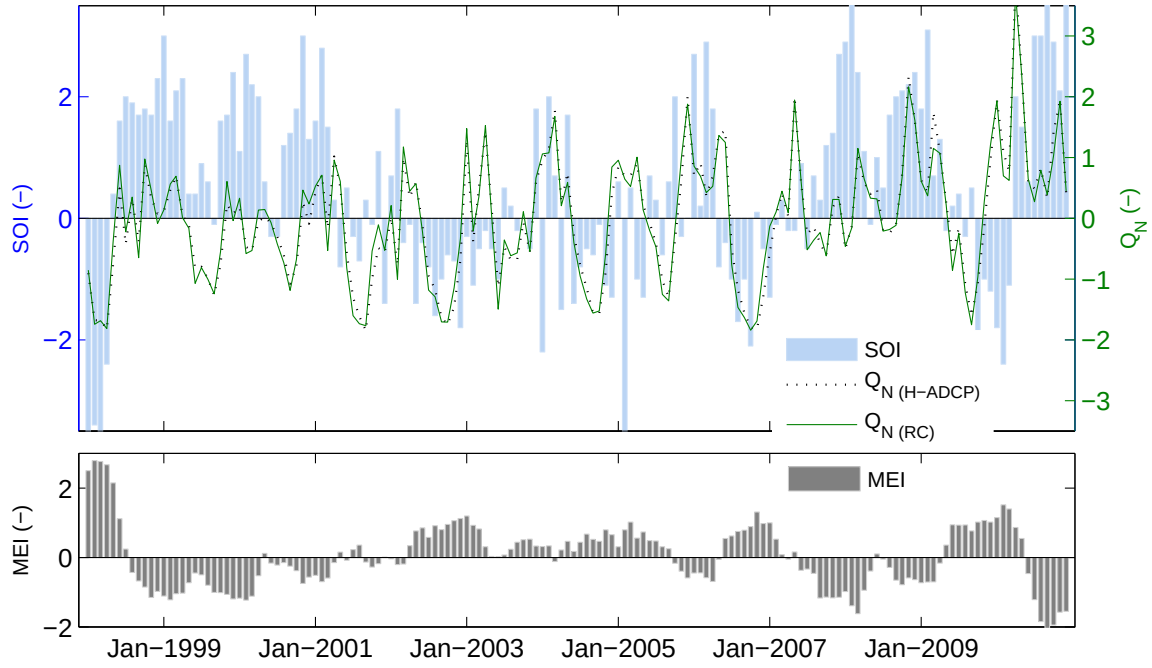

Figure 4.11: Normalized monthly averaged simulated discharge $Q_N = (Q - \bar{Q})/\sigma_Q$, where $\bar{Q}$ is mean and σ_Q is standard deviation, for Melak from the HBV model plotted along with the Southern Oscillation Index (top) and the Multivariate ENSO Index (bottom).

Not all low-flows, such as the ones in 2001 and 2004, can directly be linked to ENSO events. The late 2009 El Niño-induced low flow event was satisfactorily captured by the discharge simulations. From the study of terrestrial water storage in the Colorado River basin, Hurkmans et al. (2009) found that correlations between climatic indices and hydrological anomalies are stronger or weaker in some periods compared to others. Figure 4.11 also suggests an increasing magnitude of peak flows. This trend could be linked to environmental changes occurring in the catchment, such as land-use change and the development of water management infrastructure (Ward et al., 2008), or the variability of climatological forcings (Ward et al., 2010). This notion needs to be verified with a more elaborate study, using a longer time series of hydrological data that cannot easily be obtained in this region.

Figure 4.10 shows that, on a monthly time-scale, there is no large difference between output of models calibrated using original H-ADCP derived discharge data or the corresponding rating curve estimates. The normalized, monthly averaged simulated discharge occasionally shows a difference exceeding 50%, but the differences in the two calibration approaches do not result in a significant difference in correlation with the SOI.

4.6 Discussion

Considering the significant uncertainty in discharge estimation using rating curves (Di Baldassarre and Montanari, 2009; McMillan et al., 2010), it is counterintuitive that the highest HBV model efficiency was obtained when the rating curve derived discharge estimates were used

for calibration, instead of the original discharge data. The comparatively low model efficiency obtained by using the original discharge estimates can be understood from the downstream controls on the discharge, which make the discharge different from the runoff calculated by the rainfall-runoff model. The geographic conditions of the Melak discharge station result in multiple backwater effects from lakes and tributaries, floodplain impacts as well as effects of river-tide interaction that limit the advantage of using discharge estimated from H-ADCP data for calibrating and evaluating a rainfall-runoff model in this particular area. To some degree, rating curves better reflect the discharge dynamics that can be potentially reproduced by the rainfall-runoff model. It is important to note, however, that the manner in which the rating curve was established plays an important role.

The effect of choosing either the original continuous discharge estimates or the corresponding rating curve discharges when calibrating the HBV model is found to be time-scale dependent. The absence of any appreciable effect in the seasonal water balance, obtained by averaging simulations over a 12-year period, can be attributed to the absence of a systematic backwater effect throughout the season. The impacts of lakes, ponds and interaction between tributaries on the river discharge feature the same periodicities as the individual discharge events, which is in the order of weeks. These discharge events occur irregularly throughout the year, and overwhelm the seasonal pattern which emerges only after averaging over a large number of years. This renders the HBV model particularly appropriate to model trends and anomalies in seasonal behavior, aiming to relate those for example to ENSO variation, but less applicable to investigate peak discharge behavior, which cannot be accomplished without considering the downstream controls.

The higher model efficiency obtained by using the rating curve discharges in the calibration does not necessarily limit the merits of continuous discharge observations. The added value of obtaining a continuous discharge series, as opposed to a limited number of discharge estimates from boat surveys, is to allow for the development of an improved rating curve. Especially in lowland areas where downstream controls are strong, a continuous time-series of discharge is indispensable. Hidayat et al. (2011b) show that for the Melak station, the water level remains nearly constant at six meters, while the discharge can range over 2000 $m^3\ s^{-1}$, which is more than half the maximum discharge observed within the entire observation period. With such severe backwater effects, the traditional approach to develop a rating curve is likely to fail, unless an extremely large number of boat surveys are being carried out.

The present study highlights the merits and shortcomings of TRMM data in the development of a rainfall-runoff model in a poorly gauged catchment, confirming previous studies (Wilk et al., 2006; Huffman et al., 2007; Su et al., 2007; Villarini and Krajewski, 2007; Collischonn et al., 2008). From seven rain gauge stations it was established that the correlation between TRMM-based rainfall estimates and corresponding rain gauge heights increases strongly when a 10-day time-window is applied to the daily data, and increases slightly further when one-month averages are considered. The improvement obtained by applying a 10-day averaging procedure can mainly be attributed to the fact that the TRMM data represent an average over a 0.25 x 0.25 degree area. Although we found that the correlation for data with a resolution of one day was low, the quality of the daily rainfall products may be similarly high as the 10-day averages, which would leave the option open to simulate individual discharge events void of backwater effects. Moreover, with the Global Precipitation Measurement (GPM) mission,

which is planned to be launched in 2014 (Tapiador et al., 2012; Islam et al., 2012) the coverage and the quality of satellite precipitation estimates are expected to be improved.

4.7 Conclusions

An HBV model forced by TRMM rainfall estimates has been set up to simulate runoff from the Mahakam catchment in East Kalimantan, Indonesia. A principal characteristic of the catchment is that backwater effects from lakes extend far inland, beyond the fringe of the rainforest of central part of Kalimantan, where a continuous discharge monitoring station was installed. Two sets of discharge time-series, one derived from measurements with an H-ADCP and another from a rating curve based on the same discharge estimates (respectively), were used to calibrate the model. A higher model efficiency was obtained for the model calibrated using discharge data from the rating curve. The comparatively low model efficiency obtained by using the original discharge estimates can be understood from the downstream controls on the discharge, which are not captured in the rainfall-runoff model. To some degree, the rating curve filters out the discharge dynamics due to backwater effects, and therefore offers a better representation of the net catchment response to hydrological forcing.

Rainfall-runoff modeling based on discharge data in an outlet affected by backwaters may be practically impossible without a continuous series of river discharge estimates. Such data series are needed to establish a robust rating curve, which would require a very large number of traditional boat surveys of discharge. Using a continuous discharge series, model parameters can be estimated from a relatively short training period that captures several flood waves.

Results from model simulations over an extended period for which TRMM data were available show that the effect of choosing discharge estimates from a rating curve instead of the original discharge series on the modeled seasonality of river discharge is small. The absence of any appreciable effect in the seasonal water balance, obtained by averaging simulation results over a 12-year period, can be attributed to the absence of a systematic backwater effect throughout the season. Our results suggest that in a backwater affected catchment outlet, the calibrated HBV model is particularly appropriate to model trends and anomalies in seasonal behavior, such as effects of ENSO variations, but less applicable to investigate peak discharge behavior, which cannot be accomplished without considering the downstream controls.

This study confirms TRMM rainfall estimates have an added value to modeling the discharge dynamics of meso- to large-scale poorly gauged catchments. The impact of El Niño Southern Oscillation on the Mahakam River discharge was established, through correlation of the TRMM-derived discharge estimates with SOI (r=0.3) and with MEI (r=-0.3).

Chapter 5

Radar imagery and field water level measurements for flood mapping

Abstract: Radar imagery is potentially useful for the identification, mapping, and measurement of streams, lakes, and wetlands. Many studies showed that comparison of two consecutive radar images is useful for determining flood extent. However, the use of radar data series for flood mapping is still rarely reported. The purpose of this study is to explore the use of Phased Array L-band Synthetic Aperture Radar (PALSAR) imagery for observing the dynamics of the Mahakam River floodplain in Kalimantan, Indonesia, by incorporating field water level measurements. Water level measurements were carried out along the river, lakes and at two peatland locations, using arrays of pressure transducers. The first peatland (P1) is part of the Mahakam floodplain, representing open peat area dominated by shrub and reed. The second peatland (P2) represents a forest covered peatland. A series of PALSAR imagery (polarity: HH; pixel spacing: 50 m) covering the middle and lower Mahakam area in the years 2007 and 2008 was collected. A land use/land cover map was available from a previous analysis of PALSAR imagery. To analyze Radar backscatter behavior for different land cover types, several regions of interest were selected, based on the land cover classes. A number of land cover classes (medium shrub, high shrub, fern/grass, and secondary forest) were found to be sensitive to flooding, whereas in some other classes (peat forest, riverine forest and tree plantation) backscatter signatures remained almost unchanged with flood inundation. Correlations between water level and radar backscatter of the regions of interest were used to distinguish between three types of flooding signal, viz. flooding of low vegetation, flooding of high vegetation, and the boundary shift of lakes. An analysis of the relationship between radar backscatter and water levels was carried out in each of the regions of interest. For lakes and shrub covered peatland in P1, where the range of water level variation was high, a good water level-backscatter correlation was obtained. In peat forest covered peatland in P2, subject to a small range of water level variation, water level-backscatter correlations were poor.

This chapter is a slightly modified version of: Hidayat, H, Hoekman, D.H., Vissers, M.A.M., and Hoitink, A.J.F.: Combining ALOS-PALSAR imagery with field water level measurements for flood mapping of a tropical floodplain, Proc. SPIE 8286, Eds.: X. He, J. Xu, V. G. Ferreira, International Symposium on Lidar and Radar Mapping: Technologies and Applications, doi:10.1117/12.912735, 2011.

5.1 Introduction

Remote sensing is considered to be a solution to many problems in hydrology, considering the ever increasing data availability. Radar remote sensing has a special role in this issue as it is unconstrained by cloud cover and 24 hours per day functioning. Radar imagery is potentially useful for the identification, mapping, and measurement of streams, lakes, and wetlands. The advantages of using space-borne radar in environmental monitoring in peat swamp forests are that radar measurements can remotely sense water levels in poorly accessible areas, and to a certain extent, that radar can penetrate vegetation cover. The latter allows to observe flooding under a closed forest canopy. Most surface water features are detectable on radar imagery because of the contrast in return between the smooth water surface and the rough land surface (Lewis, 1998).

The Phased Array L-band Synthetic Aperture Radar (PALSAR) is one of the remote sensing instruments on-board of the Advanced Land Observing Satellite (ALOS). PALSAR is a polarimetric instrument operating at a centre frequency of 1270 MHz (23.6 cm) with a systematic observation strategy during 46-day satellite cycles for global environmental monitoring (Rosenqvist et al., 2007). The modes of observation include Fine Beam Single Polarization (FBS), Fine Beam Dual Polarization (FBD), Polarimetric (POL), and ScanSAR. FBS and FBD are designed for land cover changes and forest monitoring. POL is dedicated for research related to polarimetry and polarimetric interferometry. ScanSAR is intended for seasonal phenomena studies such as inundation extent monitoring and rice-field mapping. All land areas on the globe are covered at least once every year by the FBS, FBD, and ScanSAR modes. The typical repetition frequency for most areas is three to five times per year. The regions with the highest frequency of data acquiring are Asia, Australia, Eastern Europe, and Africa (Rosenqvist et al., 2007).

Hoekman et al. (2010) used multi-temporal (dry and wet season) PALSAR images of 2007, which covered the whole of Borneo, for land use/land cover mapping based on the classification of FBS and FBD polarization (path) image pairs. The classification was performed with 18 land cover classes including seven forest types, two woodland types, two shrubland types, two grassland types and three anthropogenic vegetation types. They obtained good results for a sub-continental high resolution map, except for grassland, cropland and shrubland. Based on the confusion matrix analysis, the obtained land use/land cover (LULC) map was for 85.5 % fully in agreement with the independent reference dataset, for 7.8 % in partial agreement, while 6.7 % was in disagreement. Herein, partial agreement is defined as confusion with an adjacent class along a continuum with a fairly similar biophysical characterization, which may be related to the dynamic behaviour of low biomass areas (Hoekman et al., 2010). For a wide coverage area of about 750 000 km^2 and a relatively detailed classification, the overall result is promising. Application of longer or denser time series were expected to improve results significantly.

This study explores the use of PALSAR imagery for floodplain dynamics mapping of the Middle Mahakam Area (MMA). The MMA is characterized by low relief (Fig. 5.1) with around 40 shallow lakes on both side of the river. Lakes Semayang, Melintang, and Jempang are the three largest lakes in this region. Lakes in the MMA play a vital role in discharge regulation for the lower Mahakam area. They have a function as a buffer to store water during the high flow condition and release it during low flow. The MMA is also surrounded by peatland. The peat

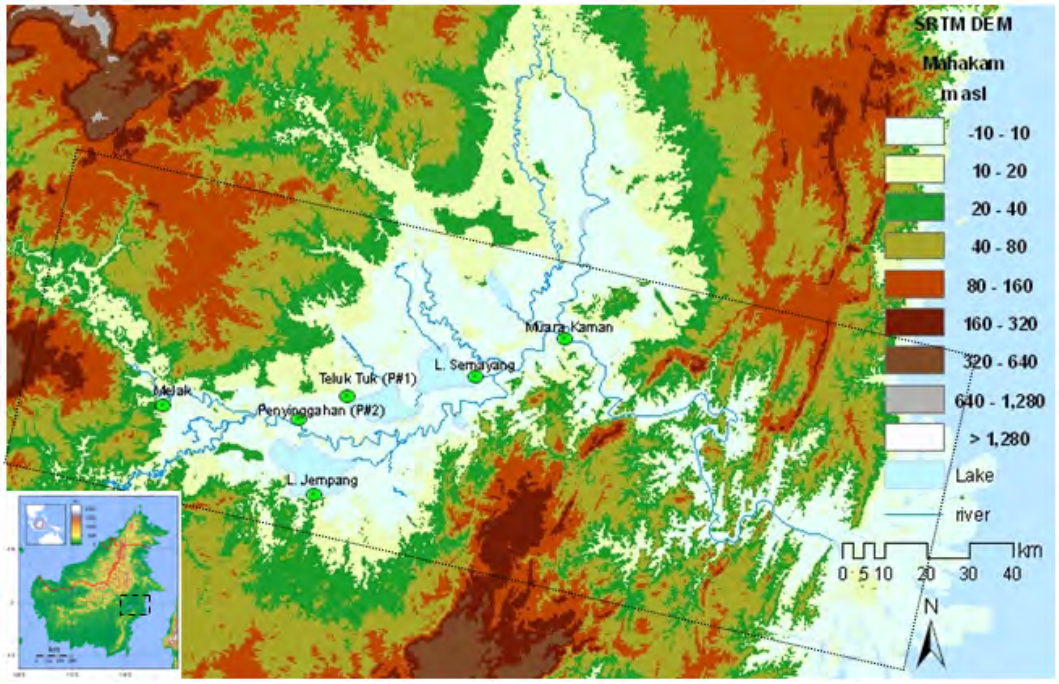

Figure 5.1: Study area in the Middle Mahakam Area, East Kalimantan, Indonesia. The box indicates the coverage of PALSAR WB1 dataset used in this study.

in Kalimantan is of ombrogenous type (Jaenicke et al., 2010; Page et al., 2004). This type of land potentially stores more water than any other type of land because of the spongey nature of its pores.

The remainder of this chapter is structured as follows. Section 5.2 describes a brief hydrological background of the middle Mahakam area. Descriptions of field site, data collection, and data processing are presented in Section 5.3. Section 5.4 presents the results discussion and finally Section 5.5 presents the conclusions.

5.2 Methodology

5.2.1 ALOS-PALSAR image collection and analysis

A series of PALSAR imagery (polarity: HH; pixel spacing: 50 m) for the year 2007 and 2008 have been collected on the following days: 4 may 2007, 4 August 2007, 19 September 2007, 4 November 2007, 20 December 2007, 4 February 2008, 21 March 2008, 6 May 2008, 21 June 2008, 6 August 2008, 21 September 2008, 22 December 2008 (Fig. 2). This dataset (referred to as WB1) was used in most of the discussions in this chapter. It mainly covers the middle and lower Mahakam areas. To extend the analysis of the water level - radar backscatter relationship, an additional dataset from far range PALSAR images that are coincided with some of the field water level measurements used in this study was collected, which will be referred to as WB91 and WB88. WB91 data stack consists of PALSAR images from 6 February 2007, 27 December

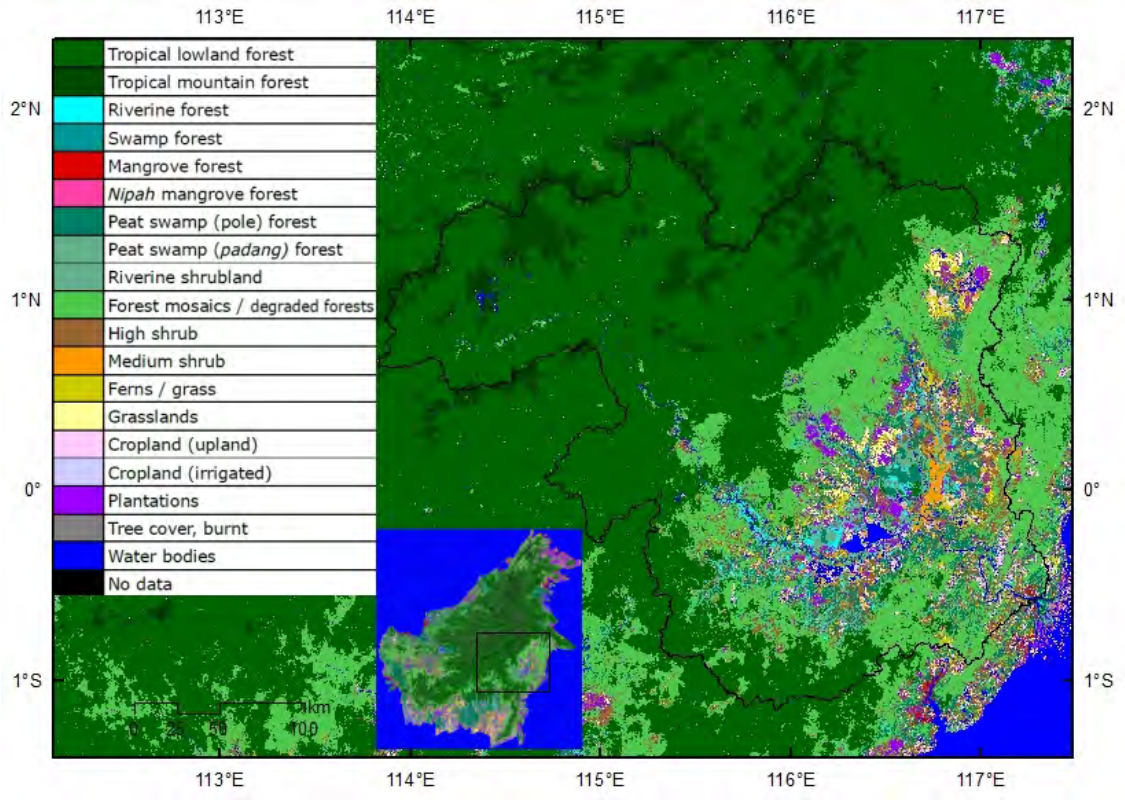

Figure 5.2: Land use/land cover map of the Mahakam river basin based on PALSAR images of 2007 (Hoekman et al., 2010). The black line indicates the catchment boundary.

2008, 29 March 2009, and 29 June 2009. WB88 data stack consists of PALSAR images from 4 November 2007, 20 December 2007, 22 December 2008, and 9 May 2009.

PALSAR images were first radiometrically calibrated. Each individual image was converted to ground range by means of registration to the SRTM elevation data set at a 90 m resolution. Speckle filtering was applied to improve flood mapping results. PALSAR images were calibrated by subtracting backscatters of each images with backscatter of the dry forest located in the North-West of the MMA. These images with relative radar backscatter values are then used in the analysis of relationship between water level and radar backscatter of regions of interest.

Radar backscatters behave differently when the land cover type is different. A good land use - land cover (LULC) map is required as background information in the interpretation of the radar signature. The LULC mapping of Kalimantan based on PALSAR images of 2007 has resulted in 19 classes of land cover types (Hoekman et al., 2010). The middle Mahakam region has a complex land cover mosaic that mainly consists of secondary/degraded forest, riverine forest, shrub, agriculture area, swamp and peat forest, which is strongly related to the inundation pattern of this lowland area and anthropogenic disturbance (Fig. 5.2).

5.2.2 Field data collection

Water level measurements using pressure transducers were installed in two peatland locations. The first location (P1), coinciding with a peatland in Penyinggahan, represents a peat area

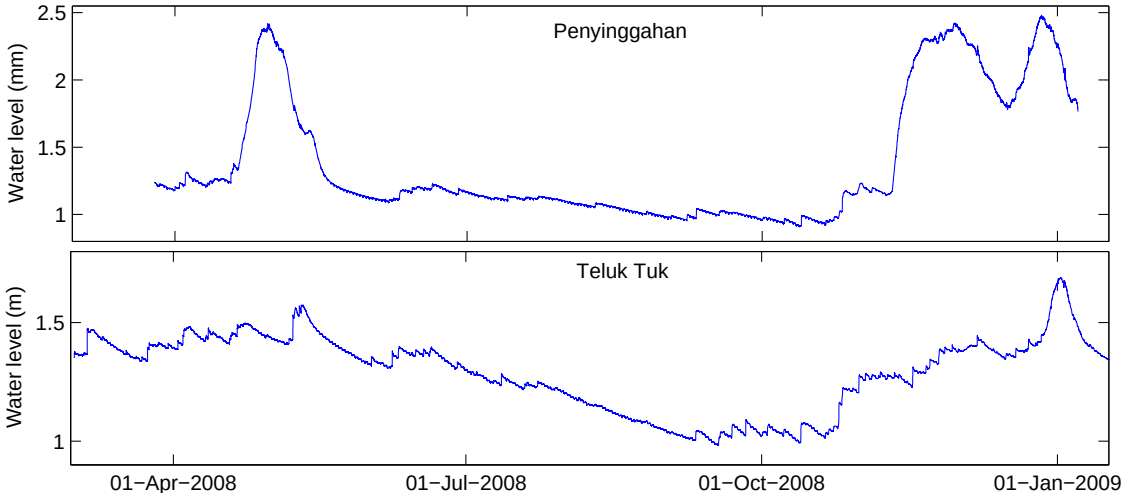

Figure 5.3: Water level measurement in the middle Mahakam area. Top: water level at Penyinggahan floodplain area (P1), bottom: water level at peat forest near Lake Melintang (P2).

opened as a result of forest fire, which is currently dominated by shrub/reed. The second location (P2) in Teluk Tuk near Lake Melintang represents peatland covered by forest. Water levels were also measured in locations along the river in Melak (upstream of MMA) and in Muara Kaman (downstream of MMA) and main lakes (Jempang, Semayang). Figure 5.3 shows water levels at P1 and P2.

The flooding regime in the MMA is generally characterised by long duration floods during the peak of the rainy season in December through January and in May, with some short duration high water evens in between. Water levels in the upstream stations are highly fluctuating in response to rainfall in the catchment, while more downstream they are also influenced by tidal waves. Bank overtopping occurred during a flooding situation in Penyinggahan. During this period, P1 was flooded and water flows through the floodplain to Lake Melintang, then to Lake Semayang, and finally meets the Mahakam again through a channel to the river.

5.3 Results and discussion

5.3.1 Water level and radar backscatter relationship

To analyze Radar backscatter behaviour of different land cover types, some regions of interest were selected based on the LULC classes. Figure 5.4 shows that medium shrub, high shrub, fern/grass, and secondary forest are sensitive to flooding, while peat forest, riverine forest and tree plantation signatures are almost unchanged with flood inundation. This result indicates that PALSAR images cannot be directly used to map flooding under forest canopy in the MMA. However, a slight increase of the relative backscatter occurred in the peat forest and the riverine forest during flooding periods, indicating the specular double bounce effect between water surface and tree trunks. This effect can be used to distinguish between flooded and non-flooded forest.

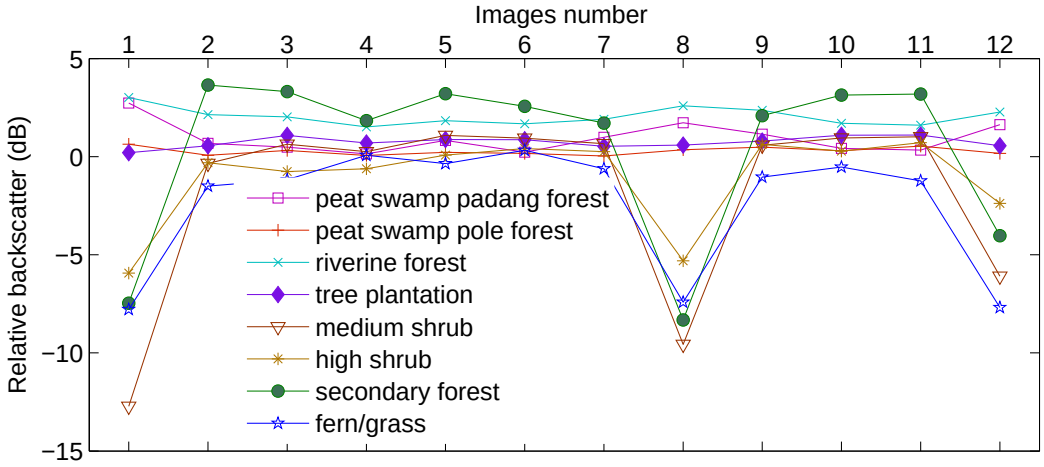

Figure 5.4: Radar backscatter of land cover classes in the Mahakam lake area. The image sequence is based on the PALSAR image acquisition date (1: 4 may 2007, 2: 4 August 2007, 3: 19 September 2007, 4: 4 November 2007, 5: 20 December 2007, 6: 4 February 2008, 7: 21 March 2008, 8: 6 May 2008, 9: 21 June 2008, 10: 6 August 2008, 11: 21 September 2008, 12: 22 December 2008).

Correlation analysis between water level data and radar backscatter of the region of interest can be used to distinguish three types of flooding signal in the different situations, i.e. flooding of low vegetation, flooding of high vegetation, and a boundary shift of a lake. Lakes and shrub covered peatland at P1, subject to a high range of water level variation, resulted in a good water level-backscatter correlation. Peat forest covered peatland at P2, subject to a low range of water level variation, gave a poor water level-backscatter correlation (5.5). This result is inline with the analysis from radar backscatter behaviour on different land cover types. Analysis using the additional WB91 and WB88 datasets (not shown) also resulted in similar trends.

The peatland in Penyinggahan is a floodplain next to River Mahakam. This area is covered by reed and high shrub during a non inundated period. When the water level rises, the area is completely inundated and becomes the extension of Lake Melintang. When the inundation period ends, the reeds have fallen so that the area appears to become a grass covered area. This results in inconsistency in the radar backscatter relationship, being different before and after inundation. Nevertheless, relatively good water level-radar backscatter correlation is found in this area. Teluk Tuk peatland is a forest-covered area next to Lake Melintang. We obtained a poor correlation between water level and Radar backscatter for this area, which could be related to the limitation of PALSAR over certain thresholds of biomass on the forest canopy.

5.3.2 Flood mapping

The effect of flooding on radar backscatter depends on the amount and the height of vegetation (Hoekman, 2009). A fully inundated region can be easily recognized on radar images from the dark signature. However, it requires more effort to map flooding under forest canopy, considering the poor correlation between radar backscatter and water level. We constructed an image by combining the minimum, mean, and maximum backscatter values of 20 PALSAR

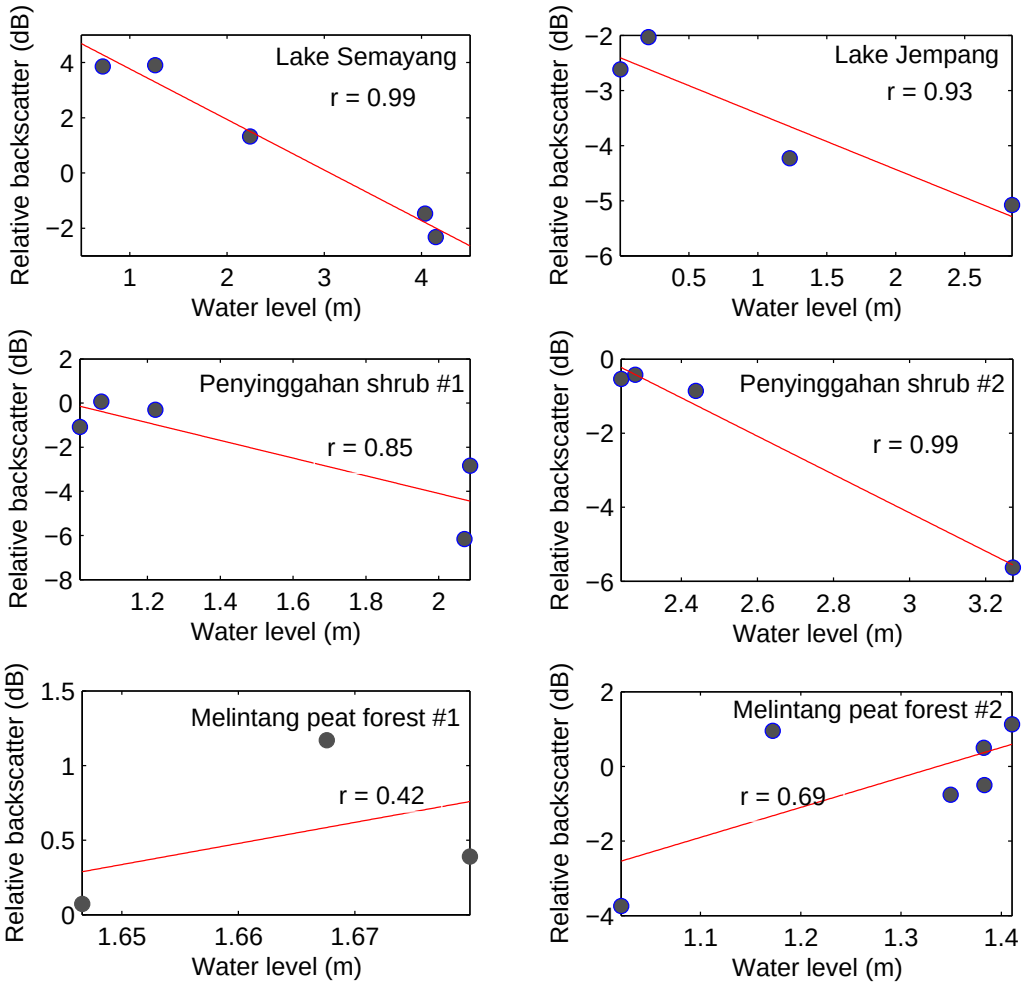

Figure 5.5: Radar backscatter variation as a function of water level.

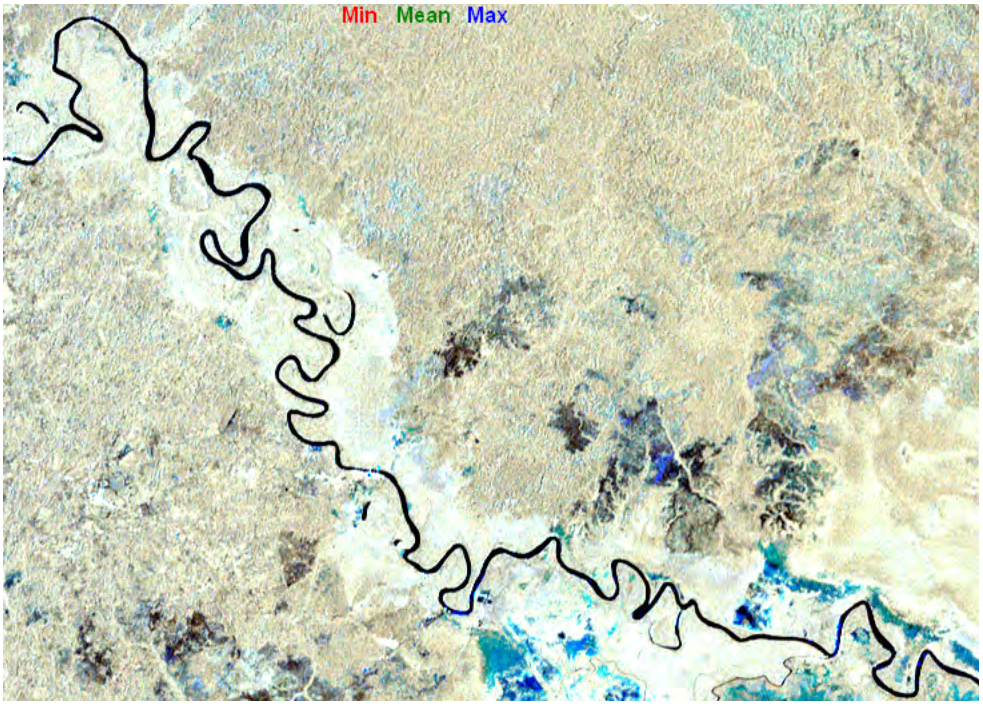

Figure 5.6: Combination of minimum-mean-maximum backscatter values of 20 images as RGB colour combination showing the floodplain upstream of the Mahakam lakes area.

images from 2007 to 2010, which shows a clear signature of flooding under forest canopy in the Mahakam floodplain upstream of the MMA (Fig. 5.6). Spectral analysis of this floodplain area reveals a consistent backscatter values around -5.5 dB. We use this value as the threshold for colour mapping of flooding under forest canopy. From the mean of three images representing the wettest conditions, we obtained a map with the maximum inundation extent of the MMA, covering inundated areas in both open water and in vegetated areas. Figure 5.7 shows that a vast area of the MMA is inundated during the flood conditions, including villages along the Mahakam river and floodplain area, which appear as open water. The open water inundation extent was indicated by dark radar returns, whereas, flooding under vegetation showed bright radar returns.

5.4 Conclusions

We used a series of PALSAR images to investigate the relation between radar backscatter and flooding in the middle Mahakam Area, East Kalimantan. Relative radar backscatter sampled in regions of interest based on a land use/land cover map showed that different land cover types yield different backscatter returns in relation with flooding. Medium shrub, high shrub, fern/grass, and secondary forest were sensitive to flooding, while peat forest, riverine forest and tree plantation signatures remained almost unchanged with flood inundation. Analysis of the radar backscatter-water level relationship shows that lakes and shrub covered peatland subject to a high range of water level variation gave a good water level-backscatter correlation.

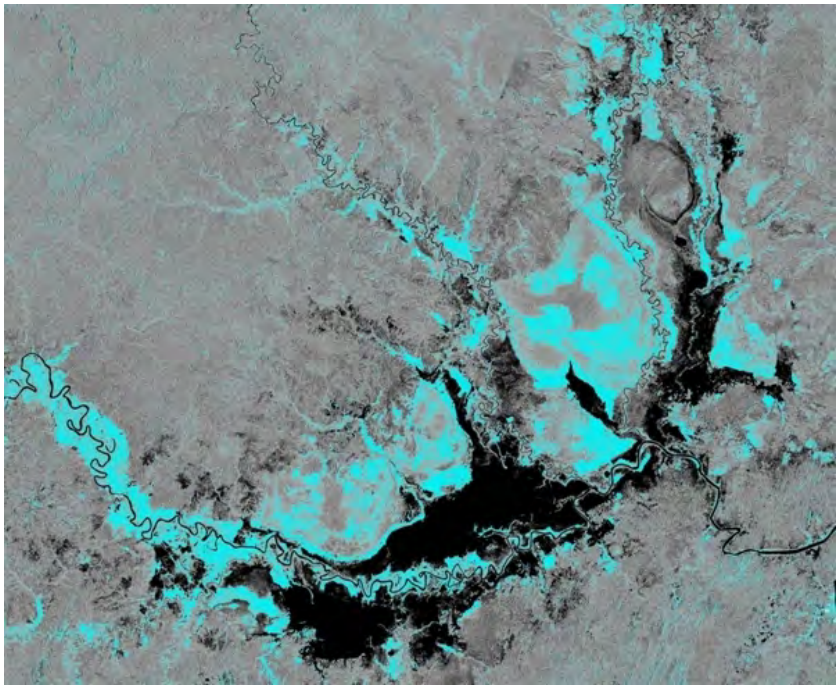

Figure 5.7: Inundation extent obtained by averaging three images in wet periods (4 May 2007, 22 December 2008, and 9 February 2010). Dark areas indicate open water inundation extent, cyan indicates flooding under vegetation.

Forest covered peatland subject to a low range of water level variation yielded a poor water level-backscatter correlation.

A clear signature of flooding under vegetation was obtained from combining images produced by taking the minimum, mean, and maximum backscatter values of PALSAR images. Floodplain delineation can be carried out from this image. In a subsequent stage, the average radar backscatter value of the floodplain area will be used as a threshold to map flooding under forest canopy in the Middle Mahakam Area.

Chapter 6

Flood occurrence mapping using satellite radar

Abstract: Floodplain lakes and peatlands in the middle Mahakam lowland area are considered as ecologically important wetland in East Kalimantan, Indonesia. However, due to a lack of data, the hydrological functioning of the region is still poorly understood. Among remote sensing techniques that can increase data availability, radar is well-suitable for the identification, mapping, and measurement of tropical wetlands, for its cloud unimpeded sensing and night and day operation. Here we aim to extract flood extent and flood occurrence information from a series of radar images of the middle Mahakam lowland area. We explore the use of Phased Array L-band Synthetic Aperture Radar (PALSAR) imagery for observing flood inundation dynamics by incorporating field water level measurements. Water level measurements were carried out along the river, in lakes and in peatlands, using pressure transducers. For validation of the open water flood occurrence map, bathymetry measurements were carried out in the main lakes. A series of PALSAR images covering the middle and lower Mahakam area in the years 2007 through 2010 were collected. A fully inundated region can be easily recognized on radar images from a dark signature. Open water flood occurrence was mapped using a threshold value taken from radar backscatter of the permanently inundated river and lakes areas. Radar backscatter intensity analysis of the vegetated floodplain area revealed consistently high backscatter values, indicating flood inundation under forest canopy. We used those values as the threshold for flood occurrence mapping in the vegetated area.

This chapter is a slightly modified version of: Hidayat, H, Hoekman, D.H., Vissers, M.A.M., and Hoitink, A.J.F.: Flood occurrence mapping of the middle Mahakam lowland area using satellite radar, Hydrol. Earth Syst. Sci., 16, 1805–1816, doi:10.5194/hess-16-1805-2012, 2012.

6.1 Introduction

The application of remote sensing and GIS plays an important role in filling the gaps in wetland inventory and could reduce uncertainties due to data availability constraints (Rebelo et al., 2009). Radar data sets are gradually obtaining a more prominent role in wetland mapping, not only in scientific projects but also in operational practices that require information on wetlands' presence, extent, and conditions (Henderson and Lewis, 2008). SAR technology has been used for remote monitoring of inundation patterns, duration of hydroperiods and computation of surface water level changes in the Everglades wetlands in Florida (Bourgeau-Chavez et al., 2005; Wdowinski et al., 2008). Rosenqvist and Birkett (2002) investigate the use of JERS-1 SAR mosaics in the Congo river basin for hydrological application. They proposed that SAR mapping missions need at least three repetitive observations within one year to describe the hydrology in such a complex region. Recently, Salvia et al. (2011) used Envisat ASAR and AMSR-E data to estimate flooded area extent and mean water level in the wetlands of the Parana River Delta floodplain. They found that both active and passive microwaves data can be used to estimate water level in flooded vegetation.

The suitability of radar techniques for spatial characterization of floods (e.g. Hess et al., 1990; Oberstadler et al., 1997) draws researchers' interest to explore and apply methods for extracting flood information from satellite radar images. Based on backscattering coefficients of the L-band JERS-1 SAR images, Hess et al. (2003) used a pixel-based classifier to map wetland vegetation and flooding state for the central Amazon basin. They delineated wetlands and classified the masked area into "cover states" that consisted of vegetation cover classes and inundation states for high- and low-water conditions. They obtained a cover-state map for large regions with an accuracy of 78–91 % for open water, nonflooded forest, and flooded forest cover-state classes. Lower accuracies were reported for aquatic macrophytes and for flooded woodland. Hostache et al. (2009) proposed a SAR image analysis method for spatiotemporal characterization of flood events that includes extracting flood extent limit, estimating water level, and constraining water level estimates using hydraulic coherence concepts. The method was applied to an ENVISAT SAR image during the January 2003 flood of the Alzette river. They showed that SAR imagery offers the possibilities to obtain distributed remote-sensing-derived water levels over a large area with sufficient accuracy for calibration of a hydraulic model. Matgen et al. (2011) proposed a hybrid approach to automatically extract flood extent from SAR images by estimating the statistical distribution of open water backscatter values from SAR images of floods, radiometric thresholding to extract the core of the water bodies, and region growing to extract all water bodies. They proposed a change detection procedure using pre- or post-flood SAR reference images to remove over-detection of inundated areas. The methods were evaluated through the 2007 flood of the Severn river (using ENVISAT SAR images) and the 1997 flood of the Red river (using RADARSAT-1 images). Their study showed that the automated method that includes a change detection procedure yields the same performance as optimized manual approaches.

This study explores the use of PALSAR imagery for floodplain dynamics mapping of the Mahakam River Basin (MRB). The MRB is located in Kalimantan, the Indonesian part of Borneo, between 2°N to 1°S and 113°E to 118°E. It represents a poorly gauged meso-scale river basin with a complex land cover mosaic. Figure 5.2 shows the LULC map of Borneo,

zoomed in on the MRB area. The middle Mahakam region has a complex land cover mosaic that mainly consists of degraded forest, riverine forest, shrub, agriculture area, swamp and peat forest, which is strongly related to the inundation pattern and anthropogenic disturbances.

Part of the runoff that feeds the Mahakam is derived from peat domes, which are difficult to monitor. In studies at the plot scale, piezometers are commonly used to analyze water levels in peat, which are labour intensive to maintain (Devito et al., 1996; Baird et al., 2004; Fraser et al., 2001). SRTM data, time series of radar images and field measurement can be combined to study the temporal dynamics of lake water mixtures, and fluxes between the river and the floodplain adjacent to the river (Bonnet et al., 2008). Using the difference in mean brightness levels from SIR-B L-band radar images of coastal lowlands in East Kalimantan, Ford and Casey (1988) characterized three classes of forest canopy (swamp, coastal lowland forest and tidal forest) and two classes of open land cover (wetland and clear cuts). Ford and Casey (1988) also noted the enhanced backscatter returns from the inundated area covered by mangrove and nipah swamps. Time series of L-band radar data such as the JERS-1 SAR, the predecessor of PALSAR, have been applied to acquire information on the hydrology in Central Kalimantan peat swamps (Hoekman, 2007).

In this study we aim to extract flood extent and flood occurrence information from a series of radar images of the middle Mahakam lowland area, including both open water and areas under vegetation. We mapped the flood occurrence as counts of flood marks obtained from the evaluation of radar backscatter from PALSAR data series against flooding thresholds. The remainder of this chapter is structured as follows. Section 6.2 describes the study area and a brief hydrological background of the middle Mahakam area. Descriptions of data collection and data processing are presented in Sect. 6.3. Section 6.4 presents the results discussion and finally Sect. 6.5 presents the conclusions.

6.2 Study area

The Middle Mahakam Area (MMA) is characterized by low relief (Fig. 6.1) with around 40 shallow lakes on both sides of the river. Lakes Semayang, Melintang, and Jempang are the three largest lakes in this region. Lakes in the MMA regulate the discharge in the lower Mahakam area. They have a function as a buffer by storing water during the high flow conditions, and releasing it during low flows. Lake filling and emptying mechanisms play a role to shave water level peaks downstream of the Mahakam lakes area (Hidayat et al., 2011b). The MMA is also surrounded by peatland, as part of the Kutai lowland spreading over an area of 35 km NW–SE by 130 km SW–NE, with elevations of around sea level in the Mahakam River to ca. 24 m a.s.l. (Hope et al., 2005).

The climate in Kalimantan is strongly influenced by the Indo-Australian Monsoon driven by the Inter-tropical Convergence Zone, and El Nino-Southern Oscillation (Meehl and Arblaster, 1998). A record from a meteorological station in Kotabangun in the central part of the MMA showed that in general, the mean daily temperature varies between 24 and 29 °C, relative humidity between 73–99 % and the mean annual precipitation is approximately 2300 mm. During El Niño-Southern Oscillation (ENSO) years such as in 1997, precipitation can be as low as nearly half the mean annual value. Due to the global air circulation and the regional climate,

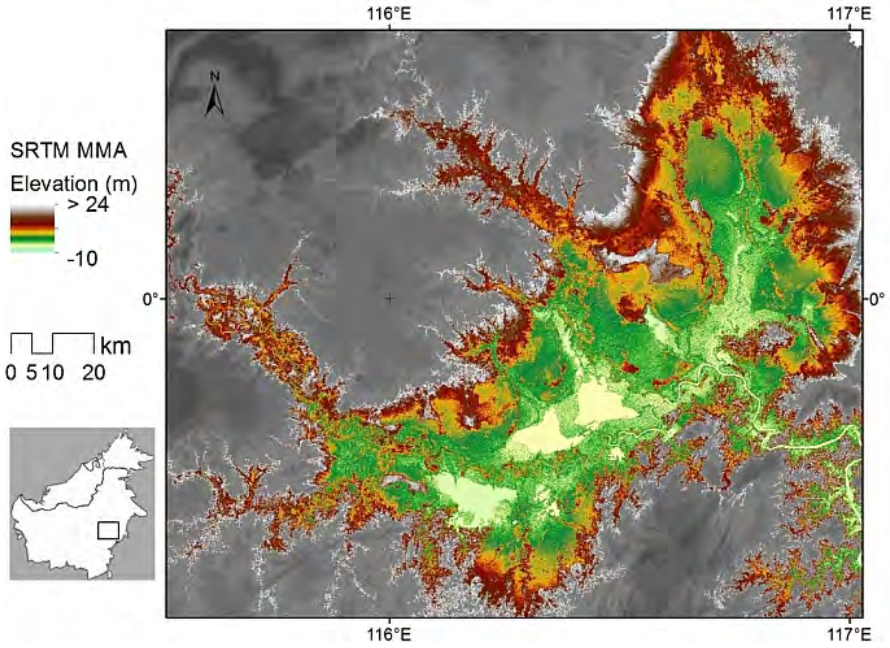

Figure 6.1: Study area in East Kalimantan with a colour coded SRTM digital elevation model for the middle Mahakam lowland area.

the Mahakam catchment has a bimodal rainfall pattern with two peaks of rainfall, which generally occur in December and in May. The normal dry season lasts from June to September. However, it may begin as early as March and last until November, as was the case during the ENSO event in 1997.

The flooding regime in the MMA is generally characterised by long duration floods during the peak of the rainy season in December through January and in May, with several short duration high water events in between. Water levels at the upstream stations are fluctuating primarily in response to rainfall in the catchment, while more downstream they are also influenced by the tidal motion. Bank overtopping occurs during a flood situation in Penyinggahan (Fig. 6.2). During this period, the Penyinggahan floodplain is flooded and water flows through the floodplain to Lake Melintang, then to Lake Semayang, and finally meets the Mahakam again through a tie-channel. Downstream of the middle Mahakam area, water level fluctuation is relatively low. Beside the lakes, the vast area of the Kutai wetland is believed to also control the River Mahakam water level and discharges downstream. The information on flood duration and inundation extent obtained in the context of the present study will be used in a future stage to model the hydrological functioning of the area, which has not been quantified to date.

6.3 Methodology

A series of PALSAR images with HH polarization and a pixel spacing of 75 m was provided by the Japan Aerospace Exploration Agency (JAXA), covering the middle and lower Mahakam areas for the years 2007 through 2010 (Table 6.1). The PALSAR images were radiometrically calibrated, orthorectified using 3″ SRTM data and corrected for slope illumination effects.

Figure 6.2: (left) River bank overtopping in Penyinggahan during the high water event in March 2009. The red line indicates water level marks on trees, from a previous flood event. (right) A view to the floodplain upstream of the MMA during low water event in August 2009. Flood marks on trees (red rectangle) indicate the height of the previous inundation in the vegetated floodplain area.

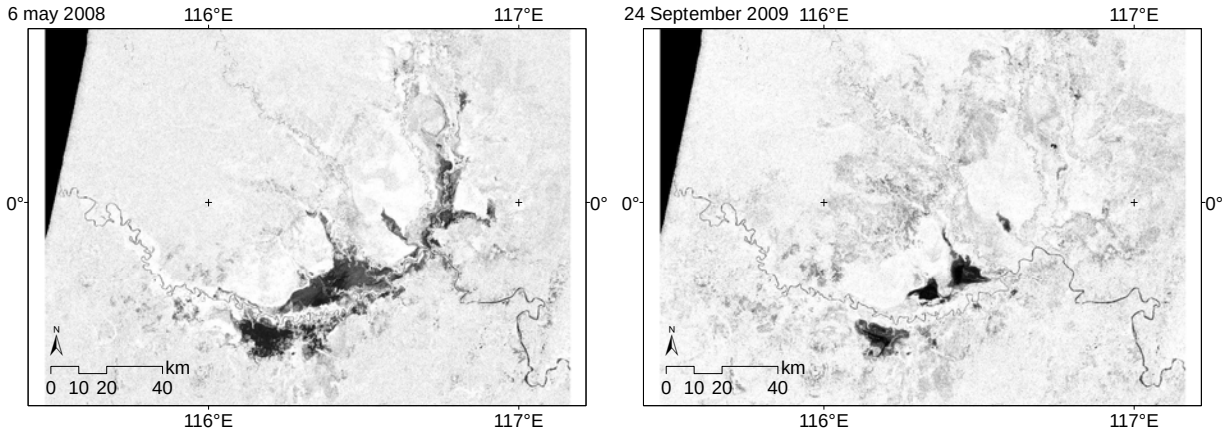

Figure 6.3: PALSAR images of the middle Mahakam area during a wet season (left) and a dry season (right). Dark areas indicate open water extent, bright areas indicate inundation under vegetation cover.

Table 6.1: PALSAR images used in this study.

Image No.	PALSAR data dates	—	Image No.	PALSAR data dates
1	19 March 2007	—	11	6 August 2008
2	4 May 2007	—	12	21 September 2008
3	4 August 2007	—	13	22 December 2008
4	19 September 2007	—	14	9 May 2009
5	4 November 2007	—	15	24 September 2009
6	20 December 2007	—	16	9 February 2010
7	4 February 2008	—	17	27 March 2010
8	21 March 2008	—	18	12 May 2010
9	6 May 2008	—	19	27 June 2010
10	21 June 2008	—	20	27 September 2010

Next, these geocoded data were chronologically stacked into a layered multi-temporal radar image suitable for time-series analysis. Figure 6.3 shows the spatial and temporal dynamics of radar backscatter from PALSAR images of the study area during wet and dry seasons. These dynamics are related to flood conditions and soil moisture.

The flood occurrence was determined by evaluating pixels in the images used as input against the lower and the upper threshold values. The pixel was flagged as flooded if its backscatter value falls within the range between the lower and upper thresholds. An image with pixel values of counts of the flooded flag was obtained, which was then colour mapped. As radar returns for flooding in open areas and for flooding under vegetation result in contrasting behavior (dark for the former and bright for the latter), the two types of flooding were mapped separately. The crucial part in the thresholding step is to determine the upper threshold value for open water and the lower threshold value for flooding under vegetation cover. From the input images we acquired radar backscatter statistics in regions covering the main river and lakes that are known to be permanently inundated, to determine threshold values for open water flood occurrence mapping. The minimum was taken as the lower threshold, and mean plus one standard deviation was taken as the upper threshold. From the statistics of the region of interest, we obtained the threshold value of -25.1 to -11.2 dB for open water flooding detection. During the field campaign, we carried out an extensive bathymetry survey in the Mahakam River, yielding cross-river depth profiles with an interspacing of about 200 m. We used these bathymetry data for the assessment of flood occurrence threshold values. We also carried out a stream reconnaissance, which has provided a qualitative confirmation of the results presented. Since the river width is about 300 m and the pixel size is 75 m, continuous river bank lines should occur in the flood occurrence map, along the boundaries of river areas with maximum flood counts. This is indeed the case. Figure 6.4 shows flood occurrence maps obtained using different threshold values, illustrating that the threshold we chose results in a good correspondence between the river banks lines from bathymetry mapping and those apparent in the flood occurrence map.

It is generally accepted in the SAR literature that flooded vegetation results in enhanced backscatter returns (e.g. Ford and Casey, 1988; Hess et al., 1990; Townsend, 2002). Our field observations confirmed that floodplain areas in Penyinggahan showing bright returns are indeed

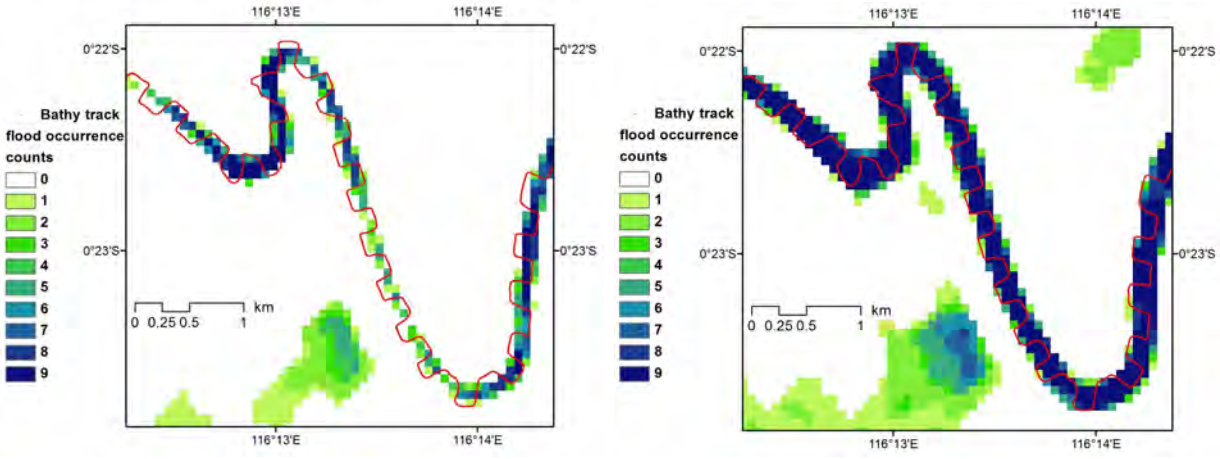

Figure 6.4: Bathymetry measurement tracks in the Mahakam River plotted on open water flood occurrence maps using the upper threshold values of −14.9 dB (left) and −11.2 dB (right).

flooded during high water conditions (Fig. 6.2 top panel). During our stream reconnaissance survey further upstream of the MMA, we also noted several flood marks on trees that provide an indication of the maximum height of the previous inundation in the vegetated floodplain area (Fig. 6.2 bottom panel). The latter inundation event resulted in a consistently enhanced radar backscatter, as further discussed in Sect. 4.2. For flooding under vegetation cover, we determined the threshold from backscatter statistics obtained from about 7900 pixels sampled from the floodplain region upstream of the MMA that was mainly covered by riverine forest, riverine shrubland, and cropland classes. Taking the mean as the lower threshold and the maximum as the upper threshold, we obtained the threshold values −7.52 and −2.26 dB for detection of flooding under vegetation cover. Based on Hope et al. (2005), the upstream boundary of the flood occurrence maps are at 24 m a.s.l. (see Fig. 6.1), which is considered to be the highest elevation in the MMA. The downstream end of the mapped area is the region of Senoni village, where the relief shifts to a steeper terrain that marks the transition to a different geological setting in the downstream region.

Speckle filtering was applied prior to flood occurrence mapping. In a preliminary flood occurrence map derived from unfiltered images, contours of the river and lake extent, which coincide with the circumferences of the areas with maximum flood occurrence, were rather noisy. The enhanced Lee filter was used to reduce speckle in the radar images while preserving texture information. We applied the filter using a 3 by 3 pixel window. The enhanced Lee filter uses coefficients of variation within an individual filter window. All pixels are divided into three classes: homogeneous, heterogeneous, or point target. Each class type is treated differently. The pixel value is replaced by the average of the filter window, replaced by the weighted average, or is not changed for homogeneous, heterogeneous, and point target classes, respectively (Lopes et al., 1990).

Pressure transducers to measure water levels were installed in the peat forest near Lake Melintang, at the shrub-covered peat swamp floodplain in Penyinggahan, along the river in Melak (upstream of MMA) and in Muara Kaman (downstream of MMA), and in the main lakes (Jempang, Semayang, Melintang). Local flood levels at the water level gauge locations

were determined by evaluating the relative position of the pressure transducers and water levels to the ground surface. Bathymetry data of lakes were collected using a single beam echosounder.

6.4 Results and discussion

6.4.1 Water level and radar backscatter relationship

An analysis of the relationship between radar backscatter and water levels is reported in Hidayat et al. (2011a). For lakes and shrub covered floodplain peatland, where the range of water level variations was large, high water level-backscatter correlations of 0.93–0.99 for the lakes and 0.85–0.99 for the floodplain peatland were obtained. In forest covered peatland subject to a small range of water level variation, water level-backscatter correlations were poor ($r = 0.42$–0.69). This poor correlation between water level and radar backscatter for this area could be related to the limitation of PALSAR over certain thresholds of biomass on the forest canopy. The backscatter changes induced by water level variation at locations of water level gauges are likely due to vegetation succession related to inundation dynamics in the study area. This is reflected by high correlations at gauges located in the lakes and floodplain areas with seasonal cycle shrub-type vegetation, and low correlations at gauges located in the peat forest.

Radar backscatter intensity depends on land cover type. The land use/land cover map by Hoekman et al. (2010) identified 19 classes of land cover types including water bodies. Figure 6.5 shows time series of radar backscatter intensity for several key land cover types in the middle Mahakam area, revealing a markedly diverging response to flooding. Regularly inundated medium shrub and high shrub were very sensitive to flooding, yielding low backscatter returns when fully inundated. Other land cover classes representing vegetated areas generally feature a moderate increase of radar backscatter intensity with flood inundation.

6.4.2 Temporal analysis of PALSAR data

A temporal analysis of radar backscatter was carried out based on the statistics from 20 images. A standard deviation image captures the backscatter intensity standard deviation for all pixels in the image. From the maximum and minimum value of radar backscatter we obtained the range image. The average absolute difference of consecutive images resulted in the mean change image. The color composite of the latter three images (Fig. 6.6) reveals a zoning that provides details in an area that was poorly classified in the work of Hoekman et al. (2010), for its complexity. The map shows land cover types that are related to the dynamics of inundation, i.e. the regularly inundated shrubland, reeds/sedges growing during dry season and floating vegetation, such as water hyacinth in lake areas, and rice growing in lake areas in years when flood levels are not too high.

6.4.3 Flood occurrence mapping of open water extent

Nine images from 2008 through 2009 were used to make a flood occurrence map, and served as the basis for accuracy assessment using field measurements taken in the corresponding period.

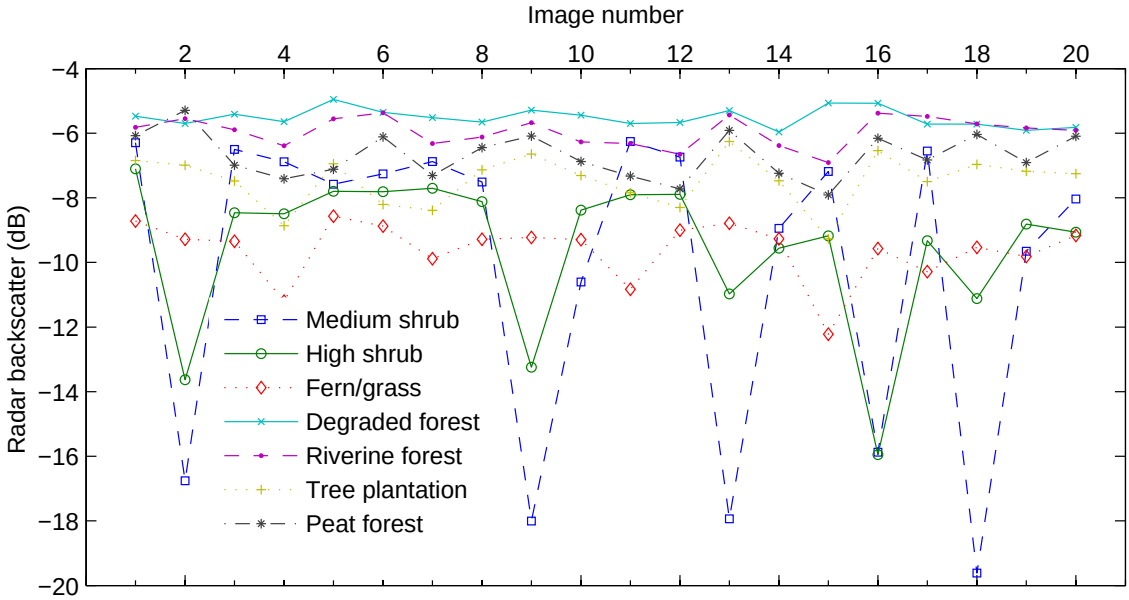

Figure 6.5: Radar backscatter mean values of land cover classes in the Mahakam lakes area. Image numbers correspond with image acquisition dates in Table 6.1.

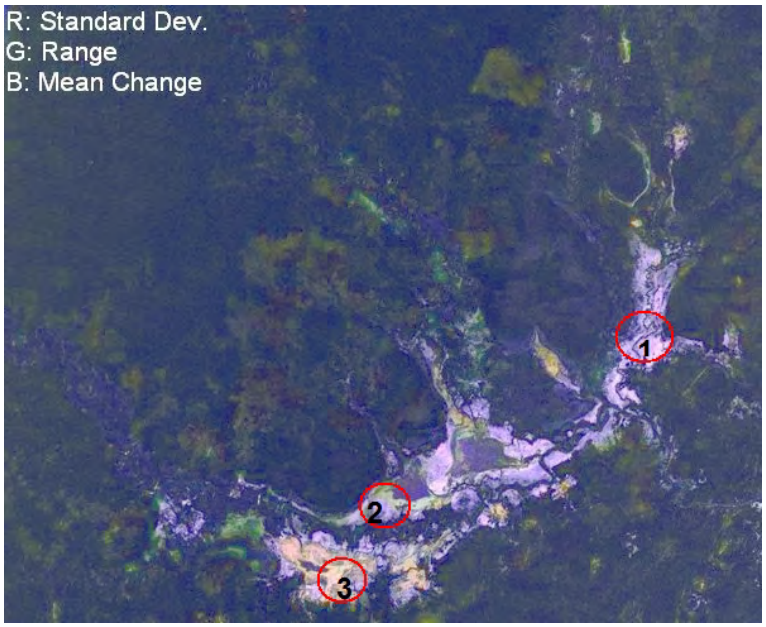

Figure 6.6: Results of a temporal analysis of 20 PALSAR images collected in the period between 19 March 2007 and 27 September 2010. Light purple indicates the regularly inundated shrubland (1), green indicates reeds/sedges (2), yellow at the southern lake indicates rice growing areas in years when flooding is not too high (3).

Table 6.2: Correlation between lake depth and flood occurrence mapped using different periods of PALSAR images for lake sections depicted in Fig. 6.8.

Period of images	# images	r_{A-B}	r_{C-D}	r_{E-F}	r_{G-H}
2008–2009	9	0.85	0.84	0.83	0.83
2007–2010	20	0.39	0.41	0.54	0.82

Figure 6.7 shows the open water flood occurrence map of the MMA from nine filtered PALSAR images using backscatter statistics from the permanently inundated main river and lakes, by taking the minimum as the lower threshold and mean plus one standard deviation as the upper threshold. Permanently inundated lake areas and main river sections were well-mapped with the maximum probability of flood occurrence. During the peak flooding events in the rainy seasons in May 2008 and December 2008, a vast area of the MMA was inundated, including villages and cities along the river. These radar-inferred flood events were qualitatively confirmed by flood marks on houses and trees in the study area, besides water level records from pressure sensors. Quantitatively, the open water flood occurrence was validated using data from bathymetry measurements of lakes (Fig. 6.8) taken during the high water period in March 2009. Sums of flood occurrence were sampled from the flood occurrence map along the bathymetric track, by extracting values on the map at the respective depth sampling point. Overall, flooding occurrence was well-correlated with lake depth (Fig. 6.9) resulting in r values of 0.83–0.85, deeper areas were more frequently flooded than shallower areas at the shores and near islands. At some places, emergent and floating plants could occupy large and patchy parts of the lakes, especially in the shallower area, creating abrupt changes in flooding occurrence between neighboring cells.

To investigate the occurrence of floods in the MMA over a longer time period, open water flood occurrence maps were produced further using 20 images from the period between 2007 and 2010, adopting the threshold values described in the previous sections. Flooding extents are generally similar between the two flood occurrence maps. However, significant differences can be observed when zooming into the lakes area (Figs. 6.10 and 6.8). Table 6.2 shows the correlations between lake depth and flooding occurrence for the two maps. Depth-occurrence correlations remained relatively high for Lake Melintang ($r = 0.82$) but dropped for all bathymetry sections in Lake Jempang ($r = 0.39$–0.54). This may be attributed to the stronger influence of human activity in Lake Jempang relative to Lake Melintang. During the dry season, large parts of Lake Jempang are used by local farmers to grow rice. This agricultural activity is not suitable in Lake Melintang due to the low pH values of water derived from peat forest. Compared to 2007, 2008 was a wet year and continued to remain wet in the first half of 2009, which resulted in relatively high lake water levels so that rice growth was not possible. In the second half of 2009, however, a relatively long dry period occurred. In addition, floating and emergent aquatic vegetation has been growing fast during the dry season and, to some extent, was maintained by local fishermen in Lake Jempang as nesting grounds for fish. During the lake emptying period following the end of the flood event, large parts of the floating plants were flushed downstream as a drifting bulk of biomass (Fig. 6.11). These vegetation dynamics and anthropogenic factors hindered validation of flood occurrence maps using lake bathymetry data.

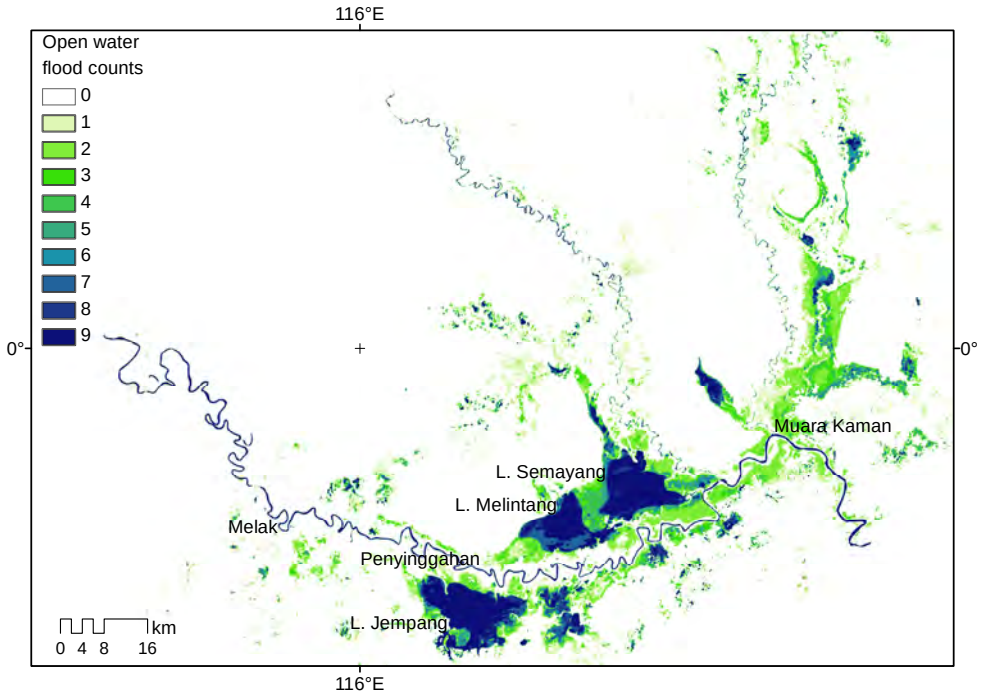

Figure 6.7: Flood occurrence map of the middle Mahakam area obtained from the filtered (enhanced Lee) PALSAR images collected in 2008 and 2009.

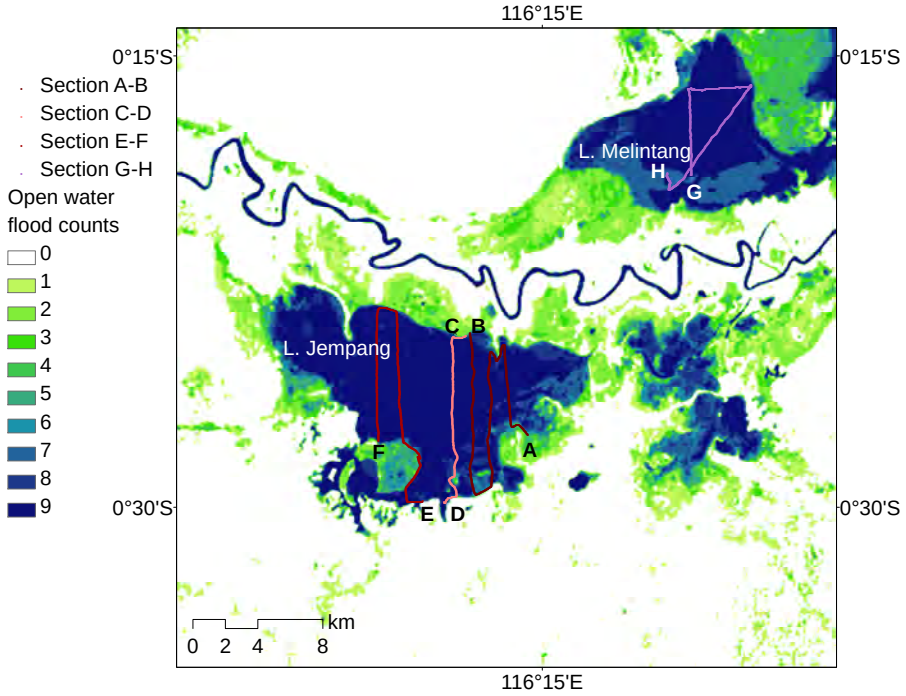

Figure 6.8: Bathymetry measurement track in Lake Jempang and Lake Melintang plotted on the flood occurrence map from nine PALSAR images in 2008 and 2009.

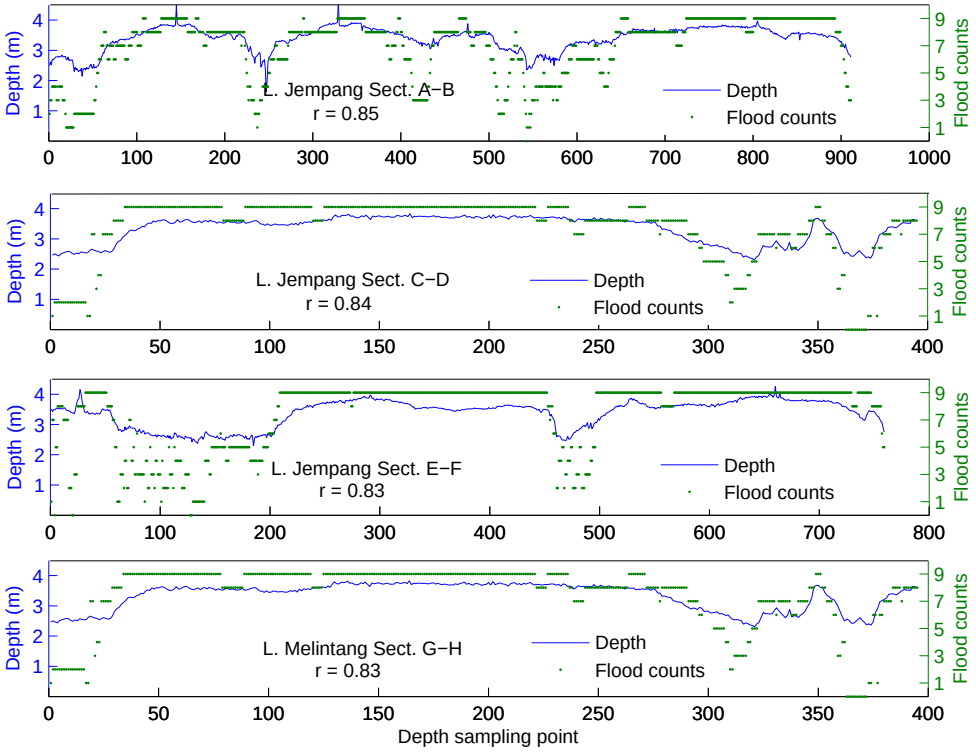

Figure 6.9: Lake depth vs. flood occurrence from nine PALSAR images collected in 2008 and 2009, r values indicate correlation coefficients.

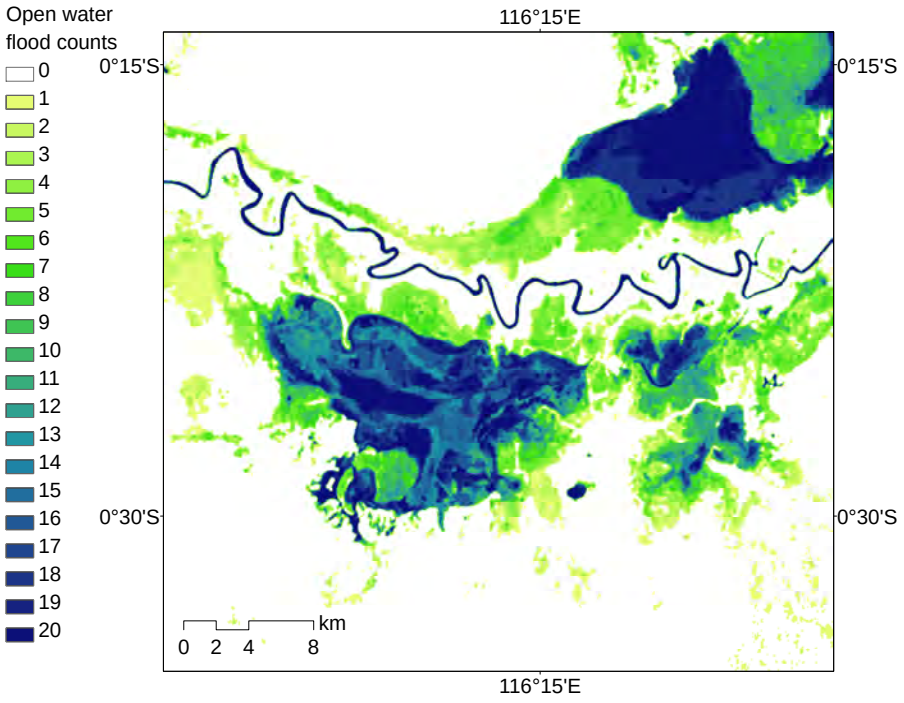

Figure 6.10: Flood occurrence map from 20 PALSAR images collected in 2007 through 2010, zoomed into the lakes area.

Figure 6.11: Bulks of floating vegetation flushed off Lake Jempang, drifting downstream during a lake emptying period.

6.4.4 Flood occurrence mapping of area under vegetation

It requires a large effort to map flooding under forest canopy, considering the poor correlation between radar backscatter and water level under such circumstances. An image obtained from combining the minimum, mean, and maximum backscatter values of 20 PALSAR images from 2007 to 2010 shows a clear signature of flooding under vegetation in the Mahakam floodplain, upstream of the MMA. The flooding occurrence under vegetation was obtained by evaluating pixels in the filtered images against the lower and the upper threshold values taken from the mean and maximum of backscatter values of the regularly inundated floodplain upstream of the MMA. Figure 6.12 shows (ground) water level records at the peat forest near Lake Melintang, plotted along with radar backscatter values, which shows enhanced radar backscatter in this flooded forest. Backscatter values are relatively high during the wet period and relatively low during the dry period, except for the image acquired on 21 September 2008, which coincided with the dry period. For the latter image, backscatter values at the water gauging points were high for low water level conditions. This may relate to the relatively high soil moisture of the peat forest compared to the rest of the area, which could lead to a false detection of flood under vegetation. Flood detection in the shrub covered peat swamp is more problematic due to the dynamics in water levels and vegetation cover. On the one hand, shrub vegetation that are mainly reed and sedges grow and cover this area during the dry season. On the other hand, this area is fully inundated during the high water period, such that it becomes an extension of the lakes. When the flood recedes, shrub vegetation falls down and the vegetation succession starts again. Consequently, some of the underestimation or overestimation of the extent of the inundated areas cannot be avoided, as noted previously by Romshoo (2006). Figure 6.13 shows the composite flood occurrence map of the MMA, overlaying results for open water and for inundation under vegetation. The flood occurrence of the peat swamps in Fig. 6.13 was mapped using the open water results, which neglects flooding of the peat swamp areas under vegetation. This problem was solved by using a simple procedure to count the total number of flood cases per pixel, which represents open water and flooding under vegetation canopy (Fig. 6.14). From Fig. 6.14, it can be inferred that at least 91 % of the mapped area was

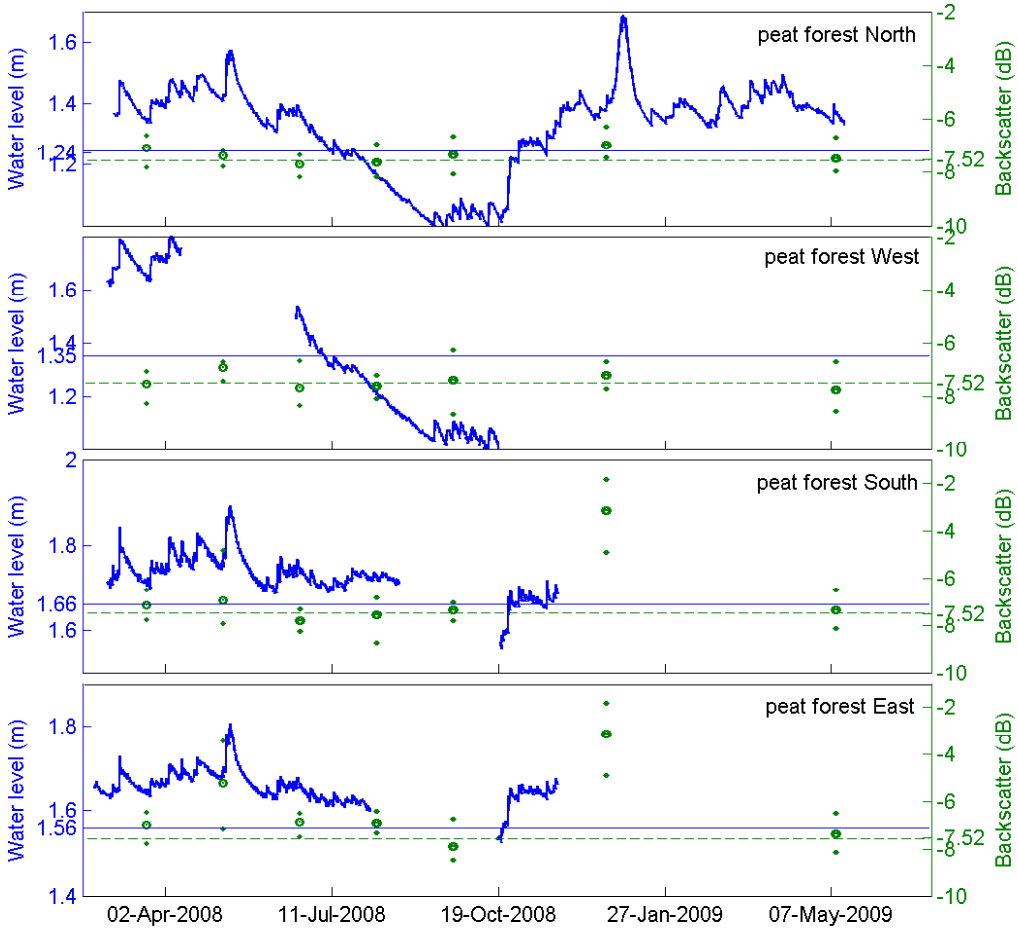

Figure 6.12: Water level and radar backscatter return values obtained from a block of nine pixels at the water level gauge locations in the peat forest near Lake Melintang. Blue lines indicate ground levels at the gauge locations. Water levels are with respect to the subterrain position of each pressure sensor. Green circles, upper and lower dots indicate mean, maximum and minimum backscatter values, respectively. The dashed green line indicates the ground level for the radar backscatter return.

inundated during the wettest period, and only about 12 % of the mapped area was inundated during the driest period.

The flooding occurrence under vegetation estimates were validated using water level measurement taken in the peat forest near Lake Melintang, by checking if the radar-based assessments could be confirmed from the level gauges. The local gauge location is assumed to represent the complete pixel area, which features local topographic irregularities. Consequently, the gauge location may better represent one of the eight pixels surrounding the pixel in which the gauge is located. Figure 6.12 therefore shows the mean, minimum and maximum backscatter return values within a block of nine pixels at the gauge location, relative to the flooding under vegetation threshold line, and compares those values with the water level relative to the local ground level. In 78 % of the cases, radar-based assessments from one or more of the nine pixels correctly indicated the water level to be above or below the ground level. This gives

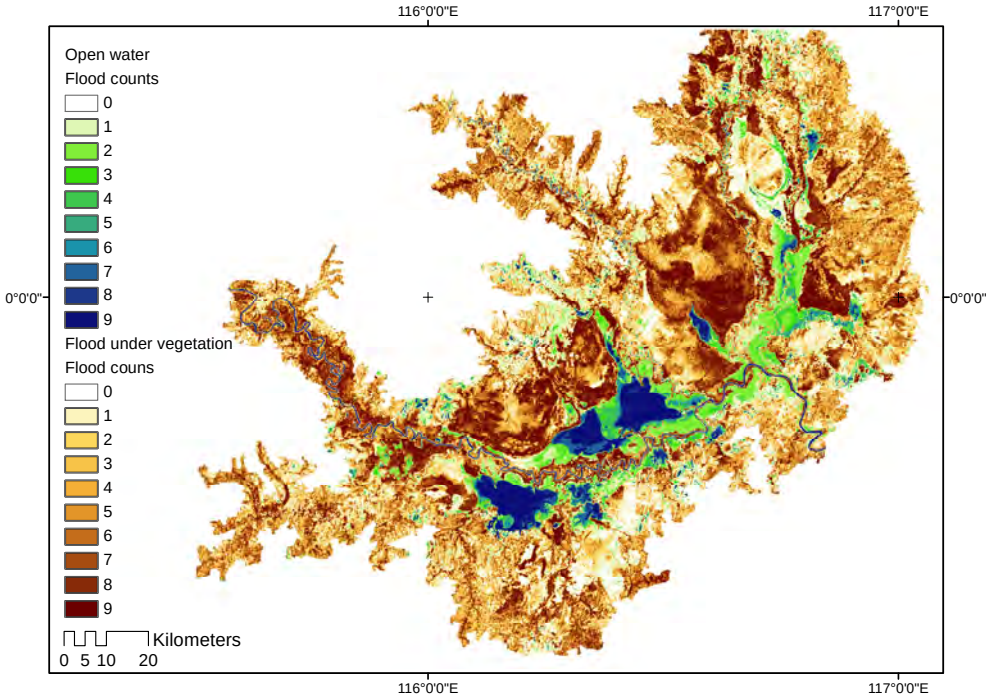

Figure 6.13: Composite flood occurrence map of the Kutai wetlands from nine PALSAR images collected in 2008 and 2009 as an overlay of results for open water and for inundation under vegetation cover.

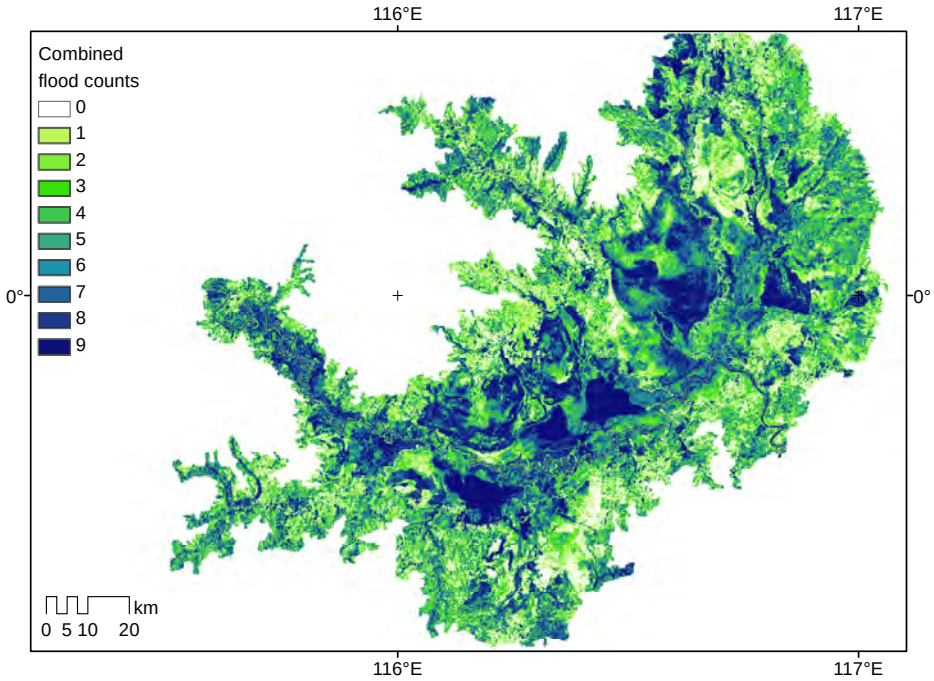

Figure 6.14: Combined flood occurrence map of the Kutai wetlands from nine PALSAR images collected in 2008 and 2009, counting the total number of flood cases per pixel, which represents both open water and flooding under vegetation.

merely a rough indication of the quality of the map produced, at least showing radar backscatter to offer a promising means of monitoring flooding under vegetation. A much larger suite of level gauges and detailed information about the micro topography would be required to achieve a more quantitative accuracy assessment.

6.5 Conclusions

Image statistics of the river and main lakes areas were used to determine thresholds to map open water flood occurrence. The minimum was taken as the lower threshold, and the mean plus a standard deviation was taken as the upper threshold. The bathymetry of lakes obtained during a high water period served as validation data for the open water flood occurrence map. High correlations between lake depth and flooding occurrence were obtained for the map derived for the wet year of 2008–2009, which is the period when field surveys were carried out. For the map derived from input images of 2007–2010, covering a longer dry period, the correlation between lake depth and flooding occurrence dropped for one particular lake, which was subject to high vegetation dynamics and rice growing activity. In a separate procedure, the average radar backscatter value of the floodplain area was used as a threshold to map flooding under forest canopy. Validation with water level data gave an indication that the flood occurrence map under vegetation cover is fairly accurate.

The flood occurrence map obtained from a newly developed algorithm offers a detailed insight into the hydroperiod and flood extent of the Mahakam lowland area, illustrating the added value of radar remote sensing to wetland hydrological studies. As a side effect, we found that simple statistics of the radar backscatter maps such as mean, total range and mean change can be used to improve land classification maps. This may help future efforts to classify flat and complex wetland areas such as the one under study, where existing classification methods fall short.

Chapter 7

Synthesis

This thesis addresses the hydrology of a tropical catchment in Kalimantan, Indonesia, focusing particularly runoff, discharge and flood occurrence. Chapters 2 through 6 advance the fields of river discharge monitoring, streamflow predictions, rainfall-runoff modelling, and flood mapping in lowland areas. In this chapter, the previous chapters are summarized and discussed by answering research questions posed in the introduction. It is concluded by an outlook.

7.1 Answers to research questions

7.1.1 Discharge estimation in the middle Mahakam area

Which are the main factors influencing discharge in the middle Mahakam area?
The geographical complexity of the middle Mahakam area controls the discharge characteristics of the discharge monitoring site in Melak. The middle Mahakam is an extremely flat area, known as the Kutai lowlands, with a series of large shallow lakes and seasonally inundated floodplains. The lowland is 35 km NW–SE by 130 km SW–NE, rising northwest from its lowest point on the Mahakam River, which roughly coincides with mean sealevel, to about 24 m above mean sealevel (Hope et al., 2005). Radar images show that vast areas of the Kutai lowlands are inundated during the wet period, and only a small part of the lake area is inundated during the dry period (Chapter 6). Four major tributaries, viz. Kedang Pahu, Kedang Kepala, Kedang Rantau, and Belayan Rivers, meet the Mahakam in this region.

The tidal influence also contributes to the complexity of discharge characteristics. Sassi et al. (2010) showed that the fortnightly tidal component reaches the middle Mahakam lakes area and further upstream. During discharge peaks, the fortnightly oscillations are damped due to increased river discharge, which attenuate the tidal motion. Numerical simulations show that tides are attenuated even for low flows when entering the lakes, whereas the fortnightly tidal constituent forces the water level of the lake despite the absence of a diurnal and semidiurnal tidal motion. The mechanism of river-tide interaction creates oscillatory and steady gradients in subtidal water level that can induce a modulation of the river flow (Sassi and Hoitink, 2013).

The dynamics of the variable backwater is linked to the storage of the lakes, which is very much related to the lakes' geometry and the connectivity to other parts of the basin. Multiple backwater effects, resulting from tributaries, lakes, floodplain ponding, and the tides influence

water level profile and discharge in Melak station.

How do factors controlling discharge dynamics affect the stage-discharge relation for Melak station?
H-ADCP measurements at Melak station revealed a complex stage-discharge relation that was highly hysteretic. Hysteresis is generally related to flood wave propagation. For the same water level, discharge is typically higher than average during the rising stage and lower than average during the falling stage, resulting in distinctive loops in stage-discharge relations (Petersen-Overleir, 2006). In Chapter 2 it was shown that a discharge range of about $2000\,m^3\,s^{-1}$ can occur for a given stage in the recorded discharge series in Melak. This is about 60% of the peak discharge and therefore exceptionally large. The large range of discharge occurring for a given stage was attributed to the multiple backwater effects from lakes and tributaries, floodplain impacts and effects of river-tide interaction. These effects render the option to predict river discharge in Melak using rating curves infeasible.

A stage-discharge model based on Jones's formula captured only a small portion of the discharge dynamics, which was attributed to the invalidity of the kinematic wave assumption due to backwater effects. The key assumption used to derive the Jones formula is the applicability of the kinematic wave equation to deal with the surface gradient term in the non-inertial wave equation. Although this approach can be successful under certain bed slope and flow conditions (Pearson, 1989; Perumal et al., 2004; Dottori et al., 2009), the kinematic wave equation cannot capture discharge dynamics in backwater affected river reaches (e.g. Tsai, 2005).

How does the interaction among factors controlling discharge dynamics affect the downstream region?
Lake emptying and filling processes contribute to retarding and accelerating the river flow velocity. At the start of lake emptying, when the lake level was still high, water stage in Melak was relatively high for a relatively low discharge. When the lake level dropped, the backwater effect was reduced and the discharge increased while the water stage kept decreasing until the point that discharge was sufficiently high to cause the water stage to follow the trend in the discharge time-series. The opposite mechanism took place during lake filling. These lake filling and emptying mechanisms play an important role in flow regulation downstream.

Water stage records downstream of the Mahakam lake area (Muara Kaman) indicate that some peaks of water level were shaved by the lake filling and emptying mechanism (see Fig. 2.13). The lowland wetlands in the middle Mahakam area form an enormous storage for water that eliminates sudden and large variations in river discharge in the lower reaches of the river. The moderation of water level (and discharge) fluctuation by the lake filling and emptying, as shown by water level record in Muara Kaman (Hidayat et al., 2011b), as well as the river-tide interaction (Sassi and Hoitink, 2013), results in limited discharge variation in the downstream region.

7.1.2 Discharge prediction in the lower Mahakam area

What is the benefit of adding water level data from upstream locations and tidal predictions to establishing a hindcast discharge prediction?

Discharge in the lower Mahakam area can be predicted from water stage and tidal water level amplitudes. In Chapter 3 it was shown that a relatively good prediction of discharge in Samarinda can be achieved by an artificial neural network (ANN) model, using upstream water level records in Tenggarong and astronomical tidal elevation predictions at sea. Both the upstream water level data in Muara Kaman and predicted tide level in the outer delta significantly contributed to the model performance. Alternative ANN models can be run without the inclusion of at-site water level or discharge as part of input variable. The ANN model can be used as a tool for data gap filling in a disrupted discharge time-series, for example based on H-ADCP data, or even for deriving discharge estimates solely from water level data and readily available astronomical tidal predictions at sea, after calibration with data from a representative period of discharge monitoring.

What is the forecast lead time for discharge predictions in a tide-dominated region? Adverse impacts of hydrological extremes such as flood and drought situations have led to a growing interest in more accurate forecasting systems. High flow forecasts, on the one hand, are necessary to provide warning systems against flooding, preventing loss of life and minimizing damage to properties. On the other hand, low flow forecasts are valuable in water supply management, navigation and other water-related issues. A successful multi-step ahead discharge prediction in Samarinda has been performed by an hourly ANN model using at-site historical discharge, upstream water level data, and astronomical tidal predictions at sea as input variables (Chapter 3). The results show that discharge can be well-predicted 1 day and 2 days in advance, with a relatively high model performance. A fairly good prediction still can be obtained in a 3-day ahead prediction, but in predicting 4 days ahead, the model output is more scattered, especially during low discharge conditions. The results show the added value of data from field measurement stations for performing discharge predictions.

7.1.3 Rainfall-runoff modelling

How can a discharge dataset from a rating curve and discharge estimates from H-ADCP measurements improve the performance of a rainfall-runoff model? Continuous series of river discharge are crucial for calibration and validation of rainfall-runoff models. In Chapter 4 it was shown that the HBV model performed markedly different when daily discharge data from H-ADCP measurements were used for calibration, instead of estimates from the rating curve. Overall, a higher model efficiency was obtained for the model calibrated using discharge data from the rating curve. The comparatively low model efficiency obtained by using the discharge estimates derived from H-ADCP data can be understood from the downstream controls on the discharge, which cause the discharge to be very much different from the runoff predicted by the rainfall-runoff model. The geographic conditions of the Melak discharge station result in multiple backwater effects from lakes and tributaries, floodplain impacts as well as effects of river-tide interaction. These effects limit the direct advantage of using discharge estimated from H-ADCP data for calibrating and evaluating a rainfall-runoff model in this particular area. To some degree, rating curves better reflect the discharge dynamics that can be potentially reproduced by the rainfall-runoff model.

How do quality differences in discharge estimation methods affect water balance estimation and long-term hydrological simulations?
The effect of choosing either the original continuous discharge estimates or the corresponding rating curve discharges when calibrating an HBV model is found to be time-scale dependent. The absence of any appreciable effect on the seasonal water balance, obtained by averaging simulations over a 12-year period, can be attributed to the absence of a systematic backwater effect throughout the season. The impacts of lakes, ponds and interaction between tributaries on the river discharge feature the same periodicities as the individual discharge events, which are in the order of weeks. These discharge events occur irregularly throughout the year, and overwhelm the seasonal pattern that emerges only after averaging over a large number of years. Results from model simulations over an extended period for which TRMM data were available show that the effect of choosing discharge estimates from a rating curve instead of the original discharge series on the modelled seasonality of river discharge is small. The absence of any appreciable effect in the seasonal water balance can be attributed to the absence of a systematic backwater effect throughout the season. Our results suggest that in a backwater-affected catchment outlet, the calibrated HBV model is particularly appropriate to model trends and anomalies in seasonal behaviour, such as effects of ENSO variations, but less applicable to investigate peak discharge behaviour, which cannot be accomplished without considering the downstream controls.

7.1.4 Flood extent and occurrence

How are different land cover types represented in radar images and how does this representation relate to inundation?
Relative radar backscatter levels, sampled in regions of interest and a land use/land cover map, showed that different land cover types yield markedly different backscatter returns in response to flooding. A fully inundated region can be easily recognized on radar images from a dark signature, due to low backscatter returns. Regularly inundated medium shrub and high shrub are very sensitive to flooding, yielding low backscatter returns when fully inundated. Other land cover classes representing vegetated areas generally feature a moderate increase of radar backscatter intensity with flood inundation. Flooded vegetation generally results in enhanced backscatter returns (e.g. Ford and Casey, 1988; Hess et al., 1990; Townsend, 2002). The field observations confirm that floodplain areas showing bright returns are indeed flooded during high water conditions. Radar returns under conditions of flooding in open areas and under flooding under vegetation result in contrasting behaviour (dark for the former and bright for the latter). This ambiguity can be dealt with by mapping the two types of flooding with different radar backscatter threshold values.

What is the spatio-temporal pattern of inundation in the Mahakam lowland area?
The middle Mahakam lowlands include vast areas of wetlands with shallow lakes, peat swamps, and peat forests. The spatio-temporal pattern of inundation events in this lowland area can be clearly identified from the spatio-temporal dynamics of radar backscatter during wet, average, and dry seasons. Image statistics of the river and main lakes areas were used to determine thresholds to map open water flood occurrence. In a separate procedure, the average radar

backscatter value of the floodplain area was used as a threshold to map flooding under forest canopy. Relative frequency of flood occurrence for each grid cell of the mapped area to the number of images used to construct the map provides new detailed information on the hydroperiod, i.e. the period in which a soil area is waterlogged, in the Mahakam lowland area. From the combination of flood occurrence maps of the open water and the one under vegetation, it can be inferred that at least 91 % of Kutai lowland is inundated during the wettest period, and only about 12 % of the area is inundated during the driest period. The dynamics of inundation in this area contributes to variable backwater effects upstream in the River Mahakam, as well as discharge modulation downstream in the downstream reaches and in the delta.

7.2 Outlook

7.2.1 Discharge estimation and prediction

In large rivers, discharge estimates are conventionally obtained from a rating curve model, using water level data as input, and a limited number of discharge measurements for calibration. Rating curve models, however, are prone to uncertainties related to interpolation and extrapolation errors and seasonal variations of the state of the vegetation (Di Baldassarre and Montanari, 2009). Changes in stage-discharge relations frequently occur due to variable backwater effects, rapidly changing discharge, overbank flow, and ponding in areas surrounding the channel (Herschy, 2009). All these factors are found in the H-ADCP discharge monitoring station in Melak in the middle Mahakam area. H-ADCPs offer a promising alternative to measure discharge. Using H-ADCP data, discharge can be estimated by continuous monitoring of flow velocity, which bears a much stronger relation to flow velocity than to the water surface (Chapter 2).

Due to circumstances such as a technical failure, or maintenance of the instrument, discharge data series can be interrupted for several days or weeks. Using an artificial neural network (ANN) model, data gap filling of this series can be performed even without the inclusion of at-site water level or discharge as input variable. With this approach, the ANN model can also be used as a tool to derive discharge estimates solely from water level monitoring stations and tide predictions after a representative period of discharge monitoring. Discharge predictions several days ahead can be useful for water management issues such as mitigation of disasters (floods, droughts) and water allocations (e.g. drinking water, irrigation). Using an ANN model that includes at-site historical data, discharge can be predicted well two days in advance (Chapter 3), allowing water managers to take necessary measures such as providing an early warning to the general public, based on forecasts.

7.2.2 Calibration of rainfall-runoff models

Considering the significant uncertainty in discharge estimation using rating curves (Di Baldassarre and Montanari, 2009; McMillan et al., 2010), it is counterintuitive that the highest rainfall-runoff model efficiency was obtained when the rating curve-derived discharge estimates were used for calibration, instead of the discharge derived from H-ADCP data. The comparatively low model efficiency obtained by using the more accurate discharge estimates derived

from H-ADCP data can be understood from the downstream controls on the discharge, which make the discharge different from the runoff calculated by the rainfall-runoff model. The geographic conditions of the Melak discharge station result in multiple backwater effects from lakes and tributaries, floodplain impacts as well as effects of river-tide interaction, which limit the advantage of using discharge estimated from H-ADCP data for calibrating and evaluating a rainfall-runoff model in this particular area.

To some degree, rating curves better reflect the discharge dynamics that can be potentially reproduced by the rainfall-runoff model (Chapter 4). The higher model efficiency obtained by using the rating curve discharges in the calibration, however, does not necessarily limit the merits of continuous discharge observations. The added value of obtaining a continuous discharge series, as opposed to a limited number of discharge estimates from boat surveys, is to allow for the development of an improved rating curve. Especially in lowland areas where downstream controls are strong, as observed in the H-ADCP station in Melak, a continuous time-series of discharge is indispensable. With such severe backwater effects, the traditional approach to develop a rating curve is likely to fail, unless an extremely large number of boat surveys are being carried out. To simulate the overall discharge dynamics in the middle Mahakam area, coupled rainfall-runoff and hydrodynamic models will be required.

7.2.3 Radar remote sensing in hydrology

Regular acquisition of remotely sensed inundation extents allows for mapping flood occurrences over large areas. In areas with little cloud cover, data from optical sensors such as Landsat imagery can be used for this purpose (e.g. Qi et al., 2009; Ran and Lu, 2012). However, for the humid tropics, the preferred limit of cloud cover is hard to be satisfied. Radar remote sensing technology offers a suitable alternative, as radar is unconstrained by cloud cover. A fully inundated region is easily recognized from a dark signature on radar images. A clear signature of flooding under vegetation was obtained from combining images produced by taking the minimum, mean, and maximum backscatter values of radar images. Floodplain delineation can be carried out from such images (Chapter 5).

The simple statistics of radar backscatter such as mean, total range and mean change can also be used to improve land cover classification maps that may help future efforts to classify flat and complex wetland areas, such as the one under study, where existing classification methods fall short. Flood extent and flood occurrence information of both open water flooding and flooding under vegetation cover can be inferred from a series of radar images (Chapter 6).

The results presented in this thesis contribute to a better understanding of the buffering role of inland wetlands such as the middle Mahakam area, in regulating the discharge towards the downstream coastal regions. In future work, radar-based floodplain observations may serve to calibrate hydrodynamic models simulating the processes of flooding and emptying of the lakes area.

Bibliography

Abrahart, R. J. and See, L. M.: Neural network modelling of non-linear hydrological relationships, Hydrol. Earth Syst. Sci ., 11, 1563–1579, 2007.

Aldrian, E. and Susanto, R. D.: Identification of three dominant rainfall regions within Indonesia and their relationship to sea surface temperature, Int. J. Climatol., 23, 1435–1452, doi:DOI: 10.1002/joc.950, 2003.

Allen, G. P., Laurier, D., and Thouvenin, J.: Sediment distribution patterns in the modern Mahakam delta, in: Proceedings Indonesian Petroleum Association, vol. 5, pp. 159–178, 1977.

Amarasekera, K. N., Lee, R. F., Williams, E. R., and Eltahir, E. A.: ENSO and the natural variability in the flow of tropical rivers, J. Hydrol., 200, 24–39, 1997.

Baird, A. J., Surridge, B. W. J., and Money, R. P.: An assessment of the piezometer method for measuring the hydraulic conductivity of a Cladium mariscus–Phragmites australis root mat in a Norfolk (UK) fen, Hydrol. Process, 18, 275–291, 2004.

Bates, P. D.: Remote sensing and flood inundation modelling, Hydrol. Process., 18, 2593–2597, 2004.

Bechle, A. J., Wu, C. H., Liu, W.-C., and Kimura, N.: Development and application of an automated river-estuary discharge imaging system, J. Hydraul. Eng., 138, 327–339, 2012.

Bergstrom, S.: Computer models of watershed hydrology, chap. The HBV model, pp. 443–476, Water Resources Publication, Highland Ranch, Colorado, 1995.

Beven, K.: Robert E. Hortons perceptual model of infiltration processes, Hydrol. Process., 18, 3447–3460, 2004.

Beven, K. J.: Rainfall-runoff modelling: the primer, John Wiley & Sons, Chichester, England, 2nd edn., 2012.

Bhattacharya, B. and Solomatine, D. P.: Neural networks and M5 model trees in modelling water level–discharge relationship, Neurocomputing, 63, 381–396., 2005.

Bonnet, M. P., Barroux, G., Martinez, J. M., Seyler, F., Moreira-Turcq, P., Cochonneau, G., Melack, J. M., Boaventura, G., Maurice-Bourgoin, L., Leon, J. G., Roux, E., Calmant, S.,

Kosuth, P., Guyot, J. L., and Seyler, P.: Floodplain hydrology in an Amazon floodplain lake (Lago Grande de Curuai), J. of Hydrol., 349, 18–30, 2008.

Bourgeau-Chavez, L. L., Smith, K. B., Brunzell, S. M., Kasischke, E. S., Romanowicz, E. A., and Richardson, C. J.: Remote monitoring of regional inundation patterns and hydroperiod in the Greater Everglades using Synthetic Aperture Radar, Wetlands, 25 (1), 176–191, 2005.

Buschman, F. A., Hoitink, A. J. F., van der Vegt, M., and Hoekstra, P.: Subtidal water level variation controlled by river flow and tides, Water Resour. Res, 45, 1–12, doi: 10.1029/2009WR008167, 2009.

Chen, J. and Adams, B. J.: Integration of artificial neural networks with conceptual models in rainfall-runoff modeling, J. Hydrol., 318, 232–249, 2006.

Chen, W.-B., Liu, W.-C., and Hsu, M.-H.: Comparison of ANN approach with 2D and 3D hydrodynamic models for simulating estuary water stage, Adv. Eng. Soft., 45, 69–79, doi: 10.1016/j.advengsoft.2011.09.018, 2012.

Chiang, Y.-M., Chang, L.-C., Tsai, M.-J., Wang, Y.-F., and Chang, F.-J.: Dynamic neural networks for real-time water level predictions of sewerage systems-covering gauged and ungauged sites, Hydrol. Earth Syst. Sci., 14, 1309–1319, doi:10.5194/hess-14-1309-2010, 2010.

Chokkalingam, U., Kurniawan, I., and Ruchiat, Y.: Fire, livelihoods, and environmental change in the Middle Mahakam peatlands, East Kalimantan, Ecology Society, 10(1), 1–17, 2005.

Cole, C. A., Brooks, R. R., and Wardrop, D. H.: Wetland hydrology as function of hydrogeomorphic (HGM) subclass, Wetlands, 17(4), 456–467, 1997.

Collischonn, B., Collischonn, W., and Tucci, C.: Daily hydrological modeling in the Amazon basin using TRMM rainfall estimates, J. Hydrol., 360, 207–216, 2008.

Corzo, G. A., Solomatine, D. P., Hidayat, de Wit, M., Werner, M., Uhlenbrook, S., and Price, R. K.: Combining semi-distributed process-based and data-driven models in flow simulation: a case study of the Meuse river basin, Hydrol. Earth Syst. Sci ., 13, 1619–1634, 2009.

Devito, K. J., Hill, A. R., and Roulet, N.: Groundwater-surface water interactions in headwater forested wetlands of the Canadian Shield, J. of Hydrology, 181, 127–147, 1996.

Di Baldassarre, G. and Montanari, A.: Uncertainty in river discharge observations: a quantitative analysis, Hydrol. Earth Syst. Sci., 13, 913–921, 2009.

Di Silvio, G.: Flood wave modifications along prismatic channels, J. Hydraul. Div. ASCE, 95, 1589–1614, 1969.

Dottori, F. and Todini, E.: Reply to Comment on 'A dynamic rating curve approach to indirect discharge measurement by Dottori et al. (2009)' by Koussis (2009), Hydr. Earth Syst. Sc., 14, 1099–1107, doi:10.5194/hess-14-1099-2010, 2010.

Dottori, F., Martina, M. L. V., and Todini, E.: A dynamic rating curve approach to indirect discharge measurement, Hydrol. Earth Syst. Sci., 13, 847–863, 2009.

Driessen, T. L. A., Hurkmans, R. T. W. L., Terink, W., Hazenberg, P., Torfs, P. J. J. F., and Uijlenhoet, R.: The hydrological response of the Ourthe catchment to climate change as modelled by the HBV model, Hydrol. Earth Syst. Sci., 14, 651–665, 2010.

Egbert, G. D. and Erofeeva, S. Y.: Efficient inverse modeling of barotropic ocean tides, J. Atmos. Ocean. Tech., 19, 183–204, 2002.

El-Shafie, A., Noureldin, A., Taha, M., Hussain, A., and Mukhlisin, M.: Dynamic versus static neural network model for rainfall forecasting at Klang River Basin, Malaysia, Hydrol. Earth Syst. Sci., 16, 1151–1169, 2012.

Ford, J. P. and Casey, D. J.: Shuttle radar mapping with diverse incidence angles in the rainforest of Borneo, Int. J. Remote Sensing, 5, 927–943, 1988.

Fraser, C. J. D., Roulet, N. T., and Lafleur, M.: Groundwater flow patterns in a large peatland, J. of Hydrology, 246, 142–154, 2001.

Fread, D. L.: Computation of stage-discharge relationship affected by unsteady flow, Water Resour. Bull., 12, 429–442, 1975.

Godin, G. and Martínez, A.: Numerical experiments to investigate the effects of quadratic friction on the propagation of tides in a channel, Cont. Shelf Res., 14, 723–748, 1994.

Gordon, R. L.: Acoustic measurement of river discharge, J. Hydraul. Eng., 115, 925–936, 1989.

Gore, J. A.: Methods in Stream Ecology, chap. Discharge measurements and streamflow analysis, pp. 51–77, Academic Press, 2006.

Govindaraju, R. S.: Artificial Neural Networks in hydrology. II: Hydrologic applications, J. Hydrol. Eng., 5, 124–137, 2000.

Hauet, A., Kruger, A., Krajewski, W., Bradley, A., Muste, M., Creutin, J. D., and Wilson, M.: Experimental system for real-time discharge estimation using an image-based method., J. Hydr. Eng., 13, 105–110, 2008.

Haylock, M. and McBride, J.: Spatial coherence and predictability of Indonesian wet season rainfall, J. Clim., 14, 3882–3887, 2001.

Hazenberg, P., Leijnse, H., and Uijlenhoet, R.: Radar rainfall estimation of stratiform winter precipitation in the Belgian Ardennes, Water Resour. Res., 47(2), 1–15, doi: 10.1029/2010WR009068, 2011.

Henderson, F. M.: Open channel flow, Prentice Hall, 544 pp, 1966.

Henderson, F. M. and Lewis, A. J.: Radar detection of wetland ecosystems: a review, Int. J. Remote Sens., 29, 5809–5835, doi:doi:10.1080/01431160801958405, 2008.

Hendon, H. H.: Indonesian rainfall variability: impacts of ENSO and local air–sea interaction, J. Climate, 16, 1775–1790, 2003.

Herschy, R. W.: Streamflow Measurement, Taylor & Francis, London and New York, third edn., 2009.

Hess, L. L., Melack, J. M., and Simonett, D. D. S.: Radar detection of flooding beneath the forest canopy: a review, Int. J. Remote Sensing, II(7), 1313–1325, 1990.

Hess, L. L., Melack, J. M., Novo, M., E. M. L., Barbosa, C. C. F., and Gastila, M.: Dual-season mapping of wetland inundation and vegetation for the central Amazon basin, Remote Sens. Env., 87, 404–428, doi:10.1016/j.rse.2003.04.001, 2003.

Hidayat, Hoekman, D. H., Vissers, M. A. M., and Hoitink, A. J. F.: Combining ALOS-PALSAR imagery with field water level measurements for flood mapping of a tropical floodplain, Proc. SPIE 8286, Eds.: X. He, J. Xu, V. G. Ferreira, International Symposium on LIDAR and Radar Mapping: Technologies and Applications, Nanjing, China, doi:10.1117/12.912735, 2011a.

Hidayat, H., Vermeulen, B., Sassi, M. G., Torfs, P. J. J. F., and Hoitink, A. J. F.: Discharge estimation in a backwater affected meandering river, Hydrol. Earth Syst. Sci., 15, 2717–2728, doi:10.5194/hess-15-2717-2011, 2011b.

Hidayat, H., Hoekman, D. H., Vissers, M. A. M., and Hoitink, A. J. F.: Flood occurrence mapping of the middle Mahakam lowland area using satellite radar, Hydrol. Earth Syst. Sci., 16, 1805–1816, doi:10.5194/hess-16-1805-2012, 2012.

Hoekman, D.: Satellite radar observation of tropical peat swamp forest as a tool for hydrological modelling and environmental protection, Marine & Freshwater Ecosystem, 17, 265–275, 2007.

Hoekman, D. H.: Geoscience and Remote Sensing, chap. Monitoring tropical peat swamp deforestation and hydrological dynamics by ASAR and PALSAR, pp. 257–275, In-Tech, Vienna, Austria, 2009.

Hoekman, D. H., Vissers, M. A. M., and Wielaard, N.: PALSAR Wide-area mapping of Borneo: methodology and validation, IEEE J. Select. Topics Appl. Earth Obs. Remote Sensing, 3(4), 605–617, 2010.

Hoitink, A. J. F.: Comment on The origin of neap-spring tidal cycles by Erik P. Kvale [Marine Geology 235 (2006) 5-18], Mar. Geol., 248 (1–2), 122–125, doi:10.1016/j.margeo.2007.04.001, 2008.

Hoitink, A. J. F., Buschman, F. A., and Vermeulen, B.: Continuous measurements of discharge from a horizontal acoustic Doppler current profiler in a tidal river, Water Resour. Res, 45, 1–13, doi:10.1029/2009WR007791, 2009.

Hope, G., Chokkalingam, U., and Anwar, S.: The stratigraphy and fire history of the Kutai Peatlands, Kalimantan, Indonesia, Quaternary Research, 64, 407–417, 2005.

Hostache, R., Matgen, P., Schumann, G., Puech, C., Hoffmann, L., and Pfister, L.: Water level estimation and reduction of hydraulic model calibration uncertainties using satellite SAR images of floods, IEEE T. Geosci. Remote, 47 (2), 431–441, 2009.

Huffman, G. and Bolvin, D.: TRMM and other data precipitation data set documentation, NASA ftp site, URL $ftp://meso-a.gsfc.nasa.gov/pub/trmmdocs/3B42\_3B43\_doc.pdf$, last accessed: 5 January 2011, 2009.

Huffman, G. J., Adler, R. F., Bolvin, D. T., Gu, G., Nelkin, E. J., Bowman, K. P., Yong, Y., Stocker, E. F., and Wolff, D. B.: The TRMM Multi-satellite Precipitation Analysis (TMPA): Quasi-global, multi-year, combined-sensor precipitation at fine scales, J. Hydrometeor., 8(1), 38–55, 2007.

Hurkmans, R., Troch, P. A., Uijlenhoet, R., Torfs, P., and Durcik, M.: Effects of climate variability on water storage in the Colorado River Basin, J. Hydrometeorol., 10 (5), 1257–2170, doi:10.1175/2009JHM1133.1, 2009.

Islam, T., Rico-Ramirez, M. A., Han, D., Srivastava, P. K., and Ishak, A. M.: Performance evaluation of the TRMM precipitation estimation using ground-based radars from the GPM validation network, J. Atmos. Sol-Terr. Phy., 77, 194–208, 2012.

Jaenicke, J., Rieley, J., Mott, C., Kimman, P., and Siegert, F.: Determination of the amount of carbon stored in Indonesian peatlands, Geoderma, 147, 151–158, doi: 10.1016/j.geoderma.2008.08.008, 2008.

Jaenicke, J., Wösten, H., Budiman, A., and Siegert, F.: Planning hydrological restoration of peatlands in Indonesia to mitigate carbon dioxide emissions, Mitig. Adapt. Strateg. Glob. Change, 15, 223–239, doi:10.1007/s11027-010-9214-5, 2010.

Jakeman, A. J. and Kokkonen, T. S.: A comparison of metric and conceptual approaches in rainfall-runoff modeling and its implications, Water Resour. Res., 37 (9), 2345–2352, 2001.

Jarvis, A., Reuter, H. I., Nelson, A., and Guevara, E.: Hole-filled seamless SRTM data V4, International Centre for Tropical Agriculture (CIAT), CGIAR website, URL $http://srtm.csi.cgiar.org$, 2008.

Jay, D. A. and Flinchem, E. P.: Interaction of fluctuating river flow with a barotropic tide: A demonstration of wavelet tidal analysis methods, J. Geophys. Res., 102, 5705–5720, 1997.

Jones, B. E.: A method of correcting river discharge for a changing stage, U.S. Geological Survey Water Supply Paper, 375-E, 117–130, 1916.

Kawanisi, K., Razaz, M., Ishikawa, K., Yano, J., and Soltaniasl, M.: Continuous measurements of flow rate in a shallow gravel-bed river by a new acoustic system, Water Resources Research, 48, 2012.

Koussis, A. D.: Comment on A praxis-oriented perspective of streamflow inference from stage observations – the method of Dottori et al. (2009) and the alternative of the Jones Formula, with the kinematic wave celerity computed on the looped rating curve by Koussis (2009), Hydrol. Earth Syst. Sci., 14, 1093–1097, doi:10.5194/hess-14-1093-2010, 2010.

Lamberti, P. and Pilati, S.: Quasi-kinematic flood wave propagation, Meccanica, 25, 107–114, 1990.

Latrubesse, E. M., Stevaux, J. C., and Sinha, R.: Tropical rivers, Geomorphology, 70, 187–206, 2005.

Le Coz, J., Pierrefeu, G., and Paquier, A.: Evaluation of river discharges monitored by a fixed side-looking Doppler profiler, Water Resour. Res., 44, 1–13, doi:10.1029/2008WR006967, 2008.

Lee, T.-L.: Back-propagation neural network for long-term tidal predictions, Ocean Engineering, 31, 225–238, 2004.

Levenberg, K.: A Method for the Solution of Certain Non-Linear Problems in Least Squares, Quarterly of Applied Mathematics, 2, 164–168., 1944.

Lewis, A. J.: Manual of Remote Sensing Vol 2, chap. Geomorphic and hydrologic applications of active microwave remote sensing in Principles and application of imaging Radar, pp. 567–618, John Wiley & Sons Inc., 1998.

Liang, S. X., Li, M. C., and Sun, Z. C.: Prediction models for tidal level including strong meteorologic effects using a neural network, Ocean Engineering, 35, 666–675, 2008.

Lindstrom, G.: A simple automatic calibration routine for the HBV model, Nord. Hydrol., 28, 153–168, 1997.

Lopes, A., Touzi, R., and Nezry, E.: Adaptive speckle filters and scene heterogeneity, IEEE Trans. Geosci. Rem. Sens., 28 (6), 992–1000, 1990.

Maier, H. R., Jain, A., Dandy, G. C., and Sudheer, K.: Methods used for the development of neural networks for the prediction of water resource variables in river systems: Current status and future directions, Environ. Modell. Softw., 25, 891–909, 2010.

Marquardt, D.: An algorithm for least-squares estimation of nonlinear parameters, SIAM J. Appl. Math., 11(2), 431–441, doi:doi:10.1137/0111030, 1963.

Matgen, P., Hostache, R., Schumann, G., Pfister, L., Hoffmann, L., and Savenije, H.: Towards an automated SAR-based flood monitoring system: lessons learned from two case studies, Phys. Chem. Earth, 36(7-8), 241–252, 2011.

McGlynn, B. L., Blöschl, G., Borga, M., Bormann, H., Hurkmans, R., Komma, J., Nandagiri, L., Uijlenhoet, R., and Wagener, T.: Run-off Prediction in Ungauged Basins: Synthesis Across Processes, Places and Scales, chap. A data acquisition framework for predictions of runoff in ungauged basins, pp. 29–51, Cambridge Univ. Press, 2013.

McMillan, H., Freer, J., Pappenberger, F., Krueger, T., and Clark, M.: Impacts of uncertain river flow data on rainfall-runoff model calibration and discharge predictions, Hydrol. Process., 24, 1270–1284, doi:10.1002/hyp.7587, 2010.

Meehl, G. and Arblaster, J.: The Asian-Australian Monsoon and El Niño-Southern Oscillation in the NCAR Climate System Model, J. Clim., 11, 1356–1385, 1998.

Milliman, J. D. and Syvitski, J. P. M.: Geomorphic–tectonic control of sediment discharge to the ocean: the importance of small mountainous rivers, J. Geol., 100, 525–5441, 1992.

Minns, A. W. and Hall, M. J.: Artificial neural networks as rainfall-runoff models, Hydrol. Sci. J., 41:3, 399–417, doi:10.1080/02626669609491511, 1996.

Moore, S., Le Coz, J., Hurther, D., and Paquier, A.: Backscattered intensity profiles from horizontal acoustic Doppler current profilers, in: River Flow 2010, pp. 1693–1700, Bundesanstalt fur Wasserbau, Braunschweig, Germany, 2010.

Nash, J. and Sutcliffe, J.: River flow forecasting through conceptual model. Part I: A discussion of principles, J. Hydrol., 10, 282–290, 1970.

Nihei, Y. and Kimizu, A.: A new monitoring system for river discharge with horizontal acoustic Doppler current profiler measurements and river flow simulation, Water Resour. Res., 44, 1–15, doi:10.1029/2008WR006970, 2008.

NOAA: (Stand Tahiti - Stand Darwin) Sea Level Press Anomaly, URL *http* : *//www.cpc.ncep.noaa.gov/data/indices/soi*, last accessed: 4 January 2012, 2012a.

NOAA: Multivariate ENSO Index (MEI), URL *http* : *//www.esrl.noaa.gov/psd/enso/mei*, last accessed: 4 January 2012, 2012b.

Oberstadler, R., Honsch, H., and Huth, D.: Asessment of the mapping capabilities of ERS-1 SAR data for flood mappig: a case study in Germany, Hydrol. Proc., 11, 1415–1425, 1997.

Page, S. E., Wust, R. A. J., Weiss, D., Rieley, J. O., Shotyk, W., and Limin, S. H.: A record of Late Pleistocene and Holocene carbon accumulation and climate change from an equatorial peat bog (Kalimantan, Indonesia): implications for past, present and future carbon dynamics, J. Quarter. Sci., 19(7), 625–635, doi:10.1002/jqs.884, 2004.

Parkin, G., Birkinshaw, S., Younger, P., Rao, Z., and Kirk, S.: A numerical modelling and neural network approach to estimate the impact of groundwater abstractions on river flows, J. Hydrol.., 339, 15–28, 2007.

Pearson, C. P.: One-dimensional flow over a plane: Criteria for kinematic wave modelling, J. Hydrol., 111, 39–48, 1989.

Peel, M. C., Finlayson, B. L., and McMahon, T. A.: Updated world map of the Köppen-Geiger climate classification, Hydrol. Earth Syst. Sci., 11, 1633–1644, 2007.

Perumal, M. and Ranga Raju, K. G.: Approximate convection–diffusion equations, J. Hydrol. Eng., 4, 160–164, 1999.

Perumal, M., Shrestha, K. B., and Chaube, U. C.: Reproduction of hysteresis in rating curves, J. Hydrol. Eng.-ASCE, 130, 870–878, 2004.

Petersen-Overleir, A.: Modelling stage-discharge relationships affected by hysteresis using the Jones formula and nonlinear regression, Hydrol. Sci. J., 51, 365–388, 2006.

Petersen-Overleir, A. and Reitan, T.: Bayesian analysis of stage-fall-discharge models for gauging stations affected by variable backwater, Hydrol. Process., 23, 3057–3074, doi: 10.1002/hyp.7417, 2009.

Qi, S., Brown, D. G., Tian, Q., Jiang, L., Zhao, T., and Bergen, K. M.: Inundation extent and flood frequency mapping using LANDSAT imagery and digital elevation models, GISci. Remote Sens., 46(1), 101–127, doi:10.2747/1548-1603.46.1.101, 2009.

Ran, L. and Lu, X. X.: Delineation of reservoirs using remote sensing and their storage estimate: an example of the Yellow River Basin, China, Hydrol. Proc., 26, 1215–1229, doi: 10.1002/hyp.8224, 2012.

Rebelo, L. M., Finlayson, C. M., and Nagabhatla, N.: Remote sensing and GIS for wetland inventory, mapping and change analysis, J. Environm. Manag., 90, 2144–2153, 2009.

Romshoo, S. A.: Radar remote sensing for monitoring of dynamic ecosystem processes related to biogeochemical exchanges in tropical peatlands, Vis. Geosci., 9, 9–28, doi:10.1007/s10069-003-0015-9, 2006.

Rosenqvist, A. and Birkett, C. M.: Evaluation of JERS-1 SAR mosaics for hydrological applications in the Congo river basin, Int. J. Remote Sens., 23 (7), 1283–1302, 2002.

Rosenqvist, A., Shimada, M., Ito, N., and Watanabe, M.: ALOS PALSAR: a pathfinder mission for global-scale monitoring of the environment, IEEE Trans. Geosci. Rem. Sens., 45,11, 3307–3316, 2007.

Salvia, M., Grings, F., Ferrazzoli, P., Barraza, V., Douna, V., Perna, P., and Karszenbaum, H.: Estimating flooded area and mean water level using active and passive microwaves: the example of Parana River Delta floodplain, Hydrol. Earth Syst. Sci., 15, 2679–2692, doi: 0.5194/hess-15-2679-2011, 2011.

Sassi, M. G. and Hoitink, A. J. F.: River flow controls on tides and tide-mean water level profiles in a tidal freshwater river, J. Geophys. Res.-Oceans, 118, doi:10.1002/jgrc.20297, 2013.

Sassi, M. G., Schellen, S., Vermeulen, B., Hidayat, Deleersnijder, E., and Hoitink, A. J. F.: Tidal impact on river discharge in the Mahakam River and distributary channels, East Kalimantan, Indonesia, in: Physics of Estuaries and Coastal Seas (PECS) conference, Colombo, Sri Lanka, 2010.

Sassi, M. G., Hoitink, A. J. F., Vermeulen, B., and Hidayat: Discharge estimation from H-ADCP measurements in a tidal river subject to sidewall effects and a mobile bed, Water Resour. Res., 47, 1–14, doi:10.1029/2010WR009972, 2011.

Schmalz, B., Tavares, F., and Fohrer, N.: Modelling hydrological processes in mesoscale lowland river basins with SWAT – capabilities and challenges, Hydrol. Sci. J., 53(5), 989–1000, 2008.

Schmidt, A. R.: Analysis of stage-discharge relations for open-channel flows and their associated uncertainties, Ph.D. thesis, University of Illinois, URL *https* : *//netfiles.uiuc.edu/aschmidt/www/ARS_Thesis/ARS_Thesis.htm*, 2002.

Seibert, J.: Estimation of parameter uncertainty in the HBV model, Nord. Hydrol., 28, 247–262, 1997.

Seibert, J. and Beven, K.: Gauging the ungauged basin: how many discharge measurements are needed?, Hydrol. Earth Syst. Sci., 13, 883–892, 2009.

Seibert, J. and McDonnell, J. J.: Land-cover impacts on streamflow: a change-detection modelling approach that incorporates parameter uncertainty, Hydrol. Sci. J., 55(3), 316–332, 2010.

Seibert, J., Uhlenbrook, S., Leibundgut, C., and Halldin, S.: Multiscale calibration and validation of a conceptual rainfall-runoff model, Phys. Chem. Earth, 25(1), 59–64, 2000.

Seidel, D. J., Fu, Q., Randel, W. J., and Reichler, T. J.: Widening of the tropical belt in a changing climate, Nature Geosci., 1, 21–24, doi:10.1038/ngeo.2007.38, 2008.

Simpson, M. R. and Bland, R.: Methods for accurate estimation of net discharge in a tidal channel, IEEE J. Oceanic Eng, 25, 437–445, 2000.

Singh, V. P. and Woolhiser, D. A.: Mathematical modeling of watershed hydrology, J. Hydrol. Eng., 7(4), 270–292, 2002.

Sivapalan, M., Takeuchi, K., Franks, S. W., Gupta, V. K., Karambiri, H., Lakshmi, V., Liang, X., Mcdonnell, J. J., Mendiondo, E. M., O'connell, P. E., Oki, T., Pomeroy, J. W., Schertzer, D., Uhlenbrook, S., and Zehe, E.: IAHS decade on Predictions in Ungauged Basins (PUB), 2003-2012: Shaping an exciting future for the hydrological sciences, Hydrol. Sci. J., 48(6), 857–880, 2003.

Solomatine, D. P. and Ostfeld, A.: Data-driven modelling: some past experiences and new approaches, J. Hydroinformatics, 10(1), 3–22, 2008.

Stephenson, D.: Stormwater Hydrology and Drainage, Elsevier Scientific Publ. Co., 1981.

Su, F., Hong, Y., and Lettenmaier, D. P.: Evaluation of TRMM multiscale precipitation analysis (TMPA) and its utility in hydrologic prediction in the La Plata basin, J. Hydrometeor., 9, 622–640, 2007.

Sudheer, K. P. and Jain, S. K.: Radial basis function neural network for modeling rating curves, J. Hydrol. Eng., 8, 161–164, 2003.

Supharatid, S.: Application of a neural network model in establishing a stage–discharge relationship for a tidal river, Hydrol. Process., 17, 3085–3099, 2003.

Tapiador, F. J., Turk, F., Petersen, W., Hou, A. Y., Garcia-Ortega, E., Machado, L. A., Angelis, C. F., Salio, P., Kidd, C., Huffman, G. J., and de Castro, M.: Global precipitation measurement: Methods, datasets and applications, Atmos. Res., 104–105, 70–97, 2012.

Todini, E.: Hydrological catchment modelling: past, present and future, Hydrol. Earth Syst. Sci., 11(1), 468–482, 2007.

Toth, E. and Brath, A.: Multistep ahead streamflow forecasting: Role of calibration data in conceptual and neural network modeling,, Water Resour. Res., 43, W11405, 1–11, doi: 10.1029/2006WR005383, 2007.

Townsend, P. A.: Relationships between forest structure and the detection of flood inundation in forested wetlands using C-band SAR, Int. J. Remote Sens., 23, 443–460, 2002.

Tsai, C. W.: Flood routing in mild-sloped rivers - wave characteristics and downstream backwater effect, J. Hydrol., 308, 151–167, doi:10.1016/j.jhydrol.2004.10.027, 2005.

van Bemmelen, R. W.: The Geology of Indonesia, vol. I A, Government Printing Office, The Hague, 1949.

van Gerven, L. P. A. and Hoitink, A. J. F.: Analysis of river planform geometry with wavelets: application to the Mahakam River reveals geographical zoning, in: Proceedings of RCEM, 2009.

Ventura, F., Spano, D., Duce, P., and Snyder, R. L.: An evaluation of common evapotranspiration equations, Irrig Sci, 18, 163–170, 1999.

Vernimmen, R. R. E., Hooijer, A., Mamenun, and Aldrian, E.: Evaluation and bias correction of satellite rainfall data for drought monitoring in Indonesia, Hydrol. Earth Syst. Sci., 16, 133–146, 2012.

Villarini, G. and Krajewski, W. F.: Evaluation of the research version TMPA three-hourly 0.25° x 0.25° rainfall estimates over Oklahoma, Geophys. Res. Lett., 34, 1–5, doi: 10.1029/2006GL029147, 2007.

Vörösmarty, C.: Global water assessment and potential contributions from Earth Systems Science, Aquat. Sci., 64, 328–351, 2002.

Vulpiani, G., Marzano, F. S., Chandrasekar, V., and Uijlenhoet, R.: Polarimetric weather radar retrieval of raindrop size distribution by means of a regularized artificial neural network, IEEE Trans. Geosci. Rem. Sens., 44 (11), 3262–3275, 2006.

Wagener, T., Sivapalan, M., McDonnell, J., Hooper, R., Lakshmi, V., Liang, X., and Kumar, P.: Predictions in ungauged basins as a catalyst for multidisciplinary hydrology, Eos, 85 (44), 451–457, 2004a.

Wagener, T., Wheater, H. S., and Gupta, H. V.: Rainfall-runoff modelling in gauged and ungauged catchments, Imperial College Press, London, 2004b.

Ward, P. J., Renssen, H., Aerts, J. C. J. H., van Balen, R. T., and Vandenberghe, J.: Strong increases in flood frequency and discharge of the River Meuse over the late Holocene: Impacts of long-term anthropogenic land use change and climate variability, Hydrol. Earth Syst. Sci., 12, 159–175, doi:10.5194/hess-12-159-2008., 2008.

Ward, P. J., Beets, W., Bouwer, L. M., Aerts, J. C. J. H., and Renssen, H.: Sensitivity of river discharge to ENSO, Geophys. Res. Lett., 37, 1–6, doi:10.1029/2010GL043215, 2010.

Wdowinski, S., Kim, S.-W., Amelung, F., Dixon, T. H., Miralles-Wilhelm, F., and Sonenshein, R.: Space-based detection of wetlands' surface water level changes from L-band SAR interferometry, Remote Sens. Env., 112, 681–696, 2008.

Wilby, R. L., Abrahart, R. J., and Dawson, C. W.: Detection of conceptual model rainfall–runoff processes inside an artificial neural network, Hydrol. Sci. J., 48(2), 163–181, 2003.

Wilk, J., Kniveton, D., Andersson, L., Layberry, R., Todd, M. C., Hughes, D., Ringrose, S., and Vanderpost, C.: Estimating rainfall and water balance over the Okavango River Basin for hydrological applications, J. Hydrol., 331, 18–29, 2006.

Wolter, K. and Timlin, M. S.: El Niño/Southern Oscillation behaviour since 1871 as diagnosed in an extended multivariate ENSO index (MEI.ext), Int. J. Climatol, 31, 1074–1087, doi: 10.1002/joc.2336, 2011.

Wösten, H., Hooijer, A., Siderius, C., Rais, D. S., Idris, A., and Rieley, J.: Tropical peatland water management modelling of the Air Hitam Laut catchment in Indonesia, Int. J River Basin Manag., 4(4), 233– 244, doi:10.1080/15715124.2006.9635293, 2006a.

Wösten, J. H. M., Berg, J. V. D., Eijk, P. V., Gevers, G. J. M., Giesen, W. B. J. T., Hooijer, A., Idris, A., Leenman, P. H., Rais, D. P., C., C. S., Silvius, M. J., Suryadiputra, N., and Tricahyo, I. W.: Interrelationships between hydrology and ecology in fire degraded tropical peat swamp forests, Int. J. Water Resour. Develop., 22(1), 157–174, 2006b.

Wösten, J. H. M., Clymans, E., Page, S. E., Rieley, J. O., and Limin, S. H.: Peat–water interrelationships in a tropical peatland ecosystem in Southeast Asia, Catena, 73, 212–224, doi:10.1016/j.catena.2007.07.010., 2008.

Yen, B. C. and Tsai, C. W. S.: On noninertia wave versus diffusion wave in flood routing, J. Hydrol., 244, 97–104, 2001.

Yitian, L. and Gu, R. R.: Modeling flow and sediment transport in a river system using an artificial neural network, Environ. Manage., 31(1), 122–134, 2003.

Ringkasan

Sungai pasang surut dan lahan basah dataran rendah merupakan area transisi objek studi ahli hidrologi dan oseanografi fisik. Ahli oseanografi cenderung menyederhanakan hidrologi sungai, dengan mengasumsikan debit sungai yang konstan saat mempelajari dinamika muara sungai. Di lain pihak, ahli hidrologi umumnya mengabaikan pengaruh pasang surut baik lansung ataupun tak langsung terhadap Tinggi Muka Air (TMA) dan debit sungai. Tesis ini bertujuan untuk mengembangkan metode memonitoring, pemodelan, dan peramalan dinamika debit pada sungai pasang surut dan lahan basah dataran rendah, dengan fokus studi di Daerah Aliran Sungai (DAS) bagian tengah dan hilir Sungai Mahakam (Kalimantan Timur, Indonesia). Sungai Mahakam dengan panjang sekitar 980 km dan DAS seluas 77.100 km^2 terletak pada koordinat geografis 2°LU - 1°LS dan 113°BT - 118°BT. Dengan kondisi tingkat kemiringan dasar sungai yang sangat kecil, pasang surut berpengaruh sangat nyata pada sungai ini. DAS Mahakam bagian tengah merupakan dataran rendah, sebagian wilayahnya lebih rendah dari muka air laut, dikelilingi rawa-rawa gambut dan danau-danau yang saling terhubung dengan sungai utama melalui saluran-saluran yang berfungsi sebagai inlet dan sekaligus sebagai outlet.

Di lokasi kajian pada bagian tengah DAS, sebuah instrumen pengukur arus berupa H-ADCP (*horizontally deployed acoustic Doppler current profiler*) dipasang di dekat kota Melak, sekitar 300 km dari muara sungai (Bab 2). Profil arus yang diperoleh dari H-ADCP kemudian dikonversi menjadi data debit. Data seri debit yang diperoleh menunjukkan sinyal pasang surut yang nyata selama periode aliran rendah rendah. Sealain itu, data debit juga menunjukkan efek arus air balik beragam (*variable backwater effects*) dari danau-danau, muara-muara anak sungai, dan penggenangan dataran banjir. Debit maksimum yang tercatat pada stasiun ini sekitar 3.250 m^3det^{-1} dengan histeresis. Akibat histeresis, rentang debit sungai yang diperoleh bisa mencapai 2.000 m^3det^{-1} untuk satu nilai TMA yang sama. Analisis *rating curve* mengindikasikan bahwa lebar rentang debit ini tidak dapat dijelaskan dengan teori dinamika gelombang kinematik. Selain efek arus air balik, variasi debit yang tinggi untuk satu nilai TMA dapat dijelaskan dengan adanya interaksi antara sungai dengan pasang surut, yang mempengaruhi variasi debit terutama pada frekuensi dua mingguan.

Pada bagian hilir DAS, stasiun H-ADCP dipasang dekat kota Samarinda, sekitar 15 km dari muara sungai. Hasil pengukuran menunjukkan besaran debit pasang surut lebih tinggi dari debit limpasan (Bab 3). Dengan kondisi pasang surut yang dominan, teknik *rating curve* konvensional tidak sesuai untuk estimasi debit sungai dari data TMA. Sebagai alternatif, sebuah model berbasis *Artificial Neural Network* (ANN) dikembangkan untuk meneliti sejauh mana debit sungai di stasiun Samarinda dapat diprediksi dari stasiun-stasiun pengukuran TMA di sepanjang sungai, dan dari prediksi tinggi pasang surut di laut. Model berbasis ANN tersebut menghasilkan estimasi debit yang baik, yang ditunjukkan oleh kinerja yang konsisten selama periode training dan validasi. Hal ini menunjukkan bahwa debit di lokasi ini dapat diprediksi dari TMA dengan model yang terkalibrasi. Model ANN yang dikembangkan juga berkinerja baik untuk memprediksi debit sungai hingga dua hari ke depan.

Bab 4 mendiskusikan pengaruh arus air balik terhadap data debit yang digunakan untuk mengkalibrasi model hujan-limpasan. Model HBV digunakan untuk memodelkan sub-DAS Mahakam bagian hulu dengan outlet DAS di stasiun Melak (25.700 km^2). Dua pendekatan digunakan untuk kalibrasi model: (1) H-ADCP dan (2) *rating curve*. Dengan pendekatan pertama, diperoleh efisiensi model yang rendah, berkaitan dengan efek arus air balik yang tidak terwakili oleh model hujan-limpasan. Pendekatan kedua menghasilkan efisiensi model yang lebih tinggi karena *rating curve* memfilter efek arus air balik dari data seri debit. Hasil kajian mengindikasikan bahwa arus air balik tidak memiliki efek musiman yang sistematis terhadap debit sungai. Variasi musiman komponen neraca air tidak terpengaruh oleh salah satu dari kedua pilihan strategi kalibrasi.

Untuk meneliti penyebab efek arus air balik, penginderaan jauh dengan Radar digunakan untuk memonitor TMA pada lahan basah Mahakam (Bab 5). Citra *Phased Array L-band Synthetic Aperture Radar* (PALSAR) digunakan untuk mengamati dinamika daerah paparan banjir. Analisis perilaku *backscatter* Radar dilakukan pada berbagai tipe tutupan lahan. Pada kelas lahan semak-semak, padang rumput, dan hutan sekunder, *backscatter* Radar sensitif terhadap genangan, sedangkan pada area hutan gambut, hutan riparian, dan perkebunan, *backscater* Radar hanya sedikit berubah karena pengaruh genangan. Analisis hubungan antara *bakscatter* Radar dengan TMA telah dilakukan. Pada area danau dan lahan gambut bersemak dengan variasi TMA yang tinggi, diperoleh korelasi TMA-*backscatter* yang baik. Pada hutan gambut dengan variasi TMA yang rendah, diperoleh korelasi TMA-*backscatter* yang rendah. Hal ini membatasi kemungkinan untuk memperoleh topografi permukaan air keseluruhan wilayah paparan banjir dari citra Radar.

Bab 6 memaparkan mengenai sejauh mana penginderaan jauh dengan Radar dapat digunakan untuk membedakan antara lahan kering dan lahan basah yang sulit dilakukan pada area tertutup vegetasi seperti pada kubah gambut (*peat domes*). Informasi luasan banjir dan frekuensi kejadian banjir berhasil diekstrak dari serangkaian citra Radar wilayah dataran rendah Mahakam bagian tengah. Wilayah yang sepenuhnya tergenang dapat dikenali dengan mudah sebagai area gelap pada citra Radar. Kejadian banjir pada lahan terbuka dipetakan dengan menggunakan nilai ambang yang diperoleh dari *backscatter* radar pada area yang tergenang secara permanen. Analisis intensitas *backscatter* radar pada area paparan banjir bervegetasi secara konsisten menunjukkan nilai *backscatter* yang tinggi, mengindikasikan genangan di bawah tutupan hutan. Pengamatan ini digunakan untuk memperoleh nilai ambang untuk pemetaan kejadian banjir pada area bervegetasi. Peta frekuensi kejadian banjir diperoleh dengan mengkombinasikan peta kejadian banjir pada area bervegetasi dan area terbuka.

Bab 7 mensintesis hasil-hasil dari bab-bab sebelumnya. Disimpulkan bahwa efek arus air balik dan pengaruh pasang surut menghilangkan opsi untuk mengestimasi debit sungai dengan metode *rating curve* yang dalam hal ini lebih tepat diinterpretasikan sebagai relasi TMA-limpasan. H-ADCP merupakan alternatif yang baik untuk memonitor debit sungai. Untuk sungai yang dipengaruhi pasang surut, model ANN dapat digunakan untuk mengisi data yang hilang pada data runtun waktu debit berbasis pengukuran dengan H-ADCP, bahkan untuk mengestimasi debit hanya menggunakan data dan prediksi TMA. Debit sungai dapat diprediksi beberapa saat ke depan yang memungkinkan instansi terkait pengelolaan air untuk mengambil langkah-langkah yang diperlukan berdasarkan hasil prediksi. Relasi TMA-limpasan yang diperoleh dari data debit kontinyu berbasis H-ADCP menghasilkan estimasi debit yang lebih akurat daripada *rating curve* yang dihasilkan dari hanya beberapa kali pengamatan debit. Peta frekuensi kejadian banjir yang diperoleh dari citra PALSAR memberikan informasi baru mengenai periode penggenangan lahan yang menggambarkan nilai tambah penginderaan jauh dengan Radar pada studi hidrologi lahan basah tropis. Di masa yang akan datang, observasi paparan banjir berbasis Radar dapat digunakan untuk mengkalibrasi model hidrodinamika untuk mensimulasikan proses-proses pengisian dan pengosongan danau-danau dataran rendah.

Acknowledgments

Many people have supported me to complete this PhD project. I would like to express my sincere thanks to each of you. In the first place, I would like to thank my promotor Remko Uijlenhoet and my co-promotor Ton Hoitink. Ton, thank you for being a great daily supervisor for me. Your passion for science has been a source of inspiration on how to plan, execute, and disseminate research activities. Your critical questions, constructive comments and suggestions have much enhanced my scientific writing. Remko, your inputs have been a great value for initializing my research project as well as for finalizing some of the chapters of this thesis. I am grateful for all your help in guiding me through each step towards my PhD.

Paul Torfs and Dirk Hoekman also provided great contributions to some parts of the work. Paul, you have contributed to the progress of my PhD since the very beginning of the project, thank you for your support. Dirk, thank you for supporting me with the radar work. To my co-workers, Bart and Maxi, thank you for your support during both the fieldwork period, among others with installing and reading instruments from the Mahakam delta up-to the hot-swampy peatlands in the middle Mahakam, and during the campus work period in Wageningen, among others on LaTeX and Matlab scripts. I feel lucky that I am a part of a solid team.

I am grateful to my home institute, Research Centre for Limnology - the Indonesian Institute of Sciences (LIPI), for providing me permission and support to pursue a higher education. Pak Jan Sopaheluwakan as the coordinator of ICOMAR, Ibu Gadis Sri Haryani as the Indonesian project leader and as the director of LIPI Limnology, who was later on succeeded by Pak Tri Widiyanto, Pak Fakhrudin as the head division of inland water computation system, who was later on succeeded by Pak Hendro Wibowo, are thanked for their full support throughout the course of my PhD study. All Bisikom staff have been very supportive, special thanks to Unggul and Fajar who have contributed to an extended part of the fieldwork. Administrative support from LIPI Limnology, BKPI, BUP, BOK as well as KBRI Den Haag is gratefully appreciated.

This research project was part of the East Kalimantan Programme (EKP), supported by WOTRO Science for Global Development, a subdivision of the Netherlands Organisation for Scientific Research (NWO). I wish to express my gratitude to Salomon Kroonenberg, Andrew Skidmore, Zoltan Vekerdy, and other EKP researchers for extensive discussions about many aspects of the work. Many thanks to all EKP colleagues for the experiences in the field and afterwards: Syarif, Duddy, Anas, Rikardo, Rory, Frans, and other EKP PhDs and post-docs. I thank all my past and present colleagues at HWM and SEG for an encouraging research environment. Thanks to Gerald, Ruud, and Hidde for their help in hydrological modelling and data processing. Ryan, thank you for facilitating the completion of the final part of my PhD.

The Japan Aerospace Exploration Agency (JAXA) is acknowledged for providing the PALSAR images used in this thesis. TRMM data used in this thesis were acquired using the GES-DISC Interactive Online Visualization ANd aNalysis Infrastructure (Giovanni) as part of the NASA's Goddard

Earth Sciences (GES) Data and Information Services Center (DISC). I am grateful to Rijkswaterstaat for lending some instruments for the field campaign. Johan Römelingh and Pieter Hazenberg (Wageningen University) are thanked for their technical support during the preparation of fieldwork campaigns and Roel Dijksma is thanked for his guidance during fieldwork initiation. A number of people are gratefully acknowledged for their help facilitating the fieldwork campaigns: Pak Wawan Kustiawan, Pak Budi Sulistioadi, Pak Wawan (Mulawarman University). Many thanks to several Dutch students (Sonja, Jan, David) and Indonesian students (Ulfah, Supri, Hesti and other students of Mulawarman University), who have contributed in data collection. Thank you for all friends of the Indonesian student association (PPI) for being my family in Wageningen.

Finally, I would like to extend my sincere gratitude to my family for all love, support and understanding that you have showed during the entire study. Indeed, this long journey has been both a rewarding and challenging period for us. To my beloved wife, Sumiati, thank you for all the encouragement, support, and love. There are no words that can express my gratitude for your understanding during my absence, for being a super-mom for the kids and for being a wonderful and caring daughter-in-law for my parents. To my beloved sons, Aris and Rafi, thank you so much for your love and understanding in your own ways despite missing Ayah. Thank you to my beloved mother, Umi, for your pray and care for me and my family. To almarhum my father, who had never seen this work completed, thank you for your pray for me even in the last moments of your life. To my mother-in-law, Emak, words cannot fully express how much I appreciate your parenting role to the kids during all my absence. Thank you to all my sisters and brothers for all the attention and help.

Hidayat

Wageningen, October 2013

List of publications

Peer-reviewed journal papers:

Hidayat, H., B. Vermeulen, M.G. Sassi, P.J.J.F. Torfs, and A.J.F. Hoitink (2011) Discharge estimation in a backwater affected meandering river. Hydrol. Earth Syst. Sci., 15, 2717–2728. doi:10.5194/hess-15-2717-2011.

Sassi, M.G., A.J.F. Hoitink, B. Vermeulen, and Hidayat (2011), Discharge estimation from H-ADCP measurements in a tidal river subject to sidewall effects and a mobile bed, Water Resour. Res., 47, W06504, doi:10.1029/2010WR009972.

Hidayat, H., D.H. Hoekman, M.A.M. Vissers and A.J.F. Hoitink. (2012) Flood occurrence mapping of the middle Mahakam lowland area using satellite radar. Hydrol. Earth Syst. Sci., 16, 1805–1816,doi:10.5194/hess-16-1805-2012.

Not directly related to this thesis:

Corzo G.A., D.P. Solomatine, Hidayat, M. de Wit, M. Werner, S. Uhlenbrook, and R.K. Price (2009) Combining semi-distributed process-based and data-driven models in flow simulation: a case study of the Meuse river basin. Hydrol. Earth Syst. Sci., 13(9):1619–1634. doi:10.5194/hess-13-1619-2009.

Buschman, F.A., A.J.F. Hoitink, S.M. de Jong, P. Hoekstra, H. Hidayat, and M.G. Sassi (2012) Suspended sediment load in the tidal zone of an Indonesian river. Hydrol. Earth Syst. Sci., 16, 4191-4204, doi:10.5194/hess-16-4191-2012.

Sassi, M.G., A.J.F. Hoitink, B. Vermeulen, and Hidayat (2013), Sediment discharge division at two tidally influenced river bifurcations. Water Resour. Res., doi:10.1002/wrcr.20216

Other papers:

Hidayat, H., A.J.F. Hoitink, M.G. Sassi, B. Vermeulen, P.J.J.F. Torfs, and R. Uijlenhoet: Rating curve for the Mahakam River relates river stage to runoff rather than to discharge. To be resubmitted to Water Resour. Res.

Hidayat, H., A.J.F. Hoitink, M.G. Sassi, P.J.J.F. Torfs: Prediction of discharge in a tidal river using artificial neural networks. Submitted to J. Hydrol. Eng.

Hidayat, D.H. Hoekman, M.A.M. Vissers, and A.J.F. Hoitink (2011) Combining ALOS-PALSAR imagery with field water level measurements for flood mapping of a tropical floodplain, SPIE 8286, Proc. Int. Symp. on LIDAR and Radar Mapping: Technologies and Applications, Nanjing, doi:10.1117/12.912735.

Pham, C.V., B. Spinewine, B.D. Bryne, E. Deleersnijder, S. Soares-Frazao, M.G. Sassi, H. Hidayat, and A.J.F. Hoitink (2011) Multiscale modeling of a tidal estuary with a finite-element shallow water

model: application to salinity intrusion into the Mahakam delta (Indonesia), in: RCEM2011: River, Coastal and Estuarine Morphodynamics, Beijing. Tsinghua University Press, pp. 1068–1081.

Sassi, M.G., S. Schellen, B. Vermeulen, Hidayat, E. Deleersnijder, and A.J.F. Hoitink (2011) Tidal impact on river discharge in the Mahakam River and distributary channels, East Kalimantan, Indonesia. Proc. 15th Physics of Estuaries and Coastal Seas Conference, Colombo.

Hidayat, F. Setiawan, U. Handoko, D.H. Hoekman, M.A.M. Vissers, A.J.F. Hoitink (2012) Inundation and water level dynamics of the Mahakam cascade lakes from satellite and on-ground observations. Proc. Seminar Nasional Limnologi VI Tahun 2012, Bogor. Pusat Penelitian Limnologi-LIPI, 307–317.

International conference abstracts:

Hidayat, A.J.F. Hoitink, R. Uijlenhoet, P.J.J.F. Torfs, M.G. Sassi, B. Vermeulen, R.T.W.L. Hurkmans. Dependence of rainfall-runoff model performance on discharge estimates from H-ADCP data and rating curves. EGU Leonardo topical conference series on the hydrological cycle. Luxembourg, November 2010.

Hidayat, H., A.J.F. Hoitink, M.G. Sassi, B. Vermeulen, R.T.W.L. Hurkmans, P.J.J.F. Torfs, R. Uijlenhoet. Added value of H-ADCP data in rainfall-runoff models driven by satellite rainfall input in a tropical basin. EGU general assembly, Vienna, April 2011.

Hidayat, H., B. Vermeulen, M.G. Sassi, P.J.J.F. Torfs, and A.J.F. Hoitink. Rating curve fails to model discharge in a backwater affected river reach. EGU general assembly, Vienna, April 2011.

Hoitink, A.J.F., B. Vermeulen, Hidayat, B.W.H. de Vries, S.W. van Berkum. Alluvial morphology in a subsiding lowland area: the Mahakam River. Int. conference on the status and future of the world's large rivers, Vienna, April 2011.

Hidayat, H., A.J.F. Hoitink, D.H. Hoekman, B. Vermeulen, M.G. Sassi, P.J.J.F. Torfs, and R. Uijlenhoet. Flood and droughts in the Mahakam lowlands: insights from radar data and a hydrological model. World Delta Summit, Jakarta, November 2011.

Sassi, M. , A.J.F. Hoitink, B. Vermeulen, Hidayat, H. Monitoring water and suspended sediment discharge in the Mahakam river and distributary channels. World Delta Summit, Jakarta, November 2011.

Vermeulen, B.; H. Hidayat, M. Sassi, M., A.J.F. Hoitink. Flow and morphodynamics in the Middle Mahakam River. World Delta Summit, Jakarta, November 2011.

Hidayat, D.H. Hoekman, M.A.M Vissers and A.J.F. Hoitink. Flood frequency mapping of the middle Mahakam lowland area using satellite radar. AGU fall meeting, San Francisco, December 2011.

Sassi, M., Hoitink, A.J.F., Vermeulen, B., Hidayat, H., Brye, B. de, Deleersnijder, E. Hydraulic geometry of a tidally influenced delta channel network: the Mahakam Delta, East Kalimantan, Indonesia. AGU fall meeting, San Francisco, December 2011.

Hoitink, A.J.F., Buschman, F.A., Sassi, M., Brye, B. de, Tarya, A., Hidayat, H., Vermeulen, B., Vegt, M. van der, Hoekstra, P., Deleersnijder, E. River-tide interactions observed from novel measurement methods and modelling: implications for pathways of sediment and delta morphology. AGU fall meeting, San Francisco, December 2011.

Vermeulen, B., A.J.F. Hoitink, M. Sassi, F.A. Buschman, and H. Hidayat. Methods to estimate river discharge from horizontally deployed acoustic Doppler current profilers. Hydraulic Measurements and Experimental Methods Conference, Utah, USA, August 2012.

Hidayat, M.G. Sassi, B. Vermeulen, and A.J.F. Hoitink. H-ADCP discharge monitoring of a large tropical river. AGU fall meeting, San Francisco, December 2012.

Netherlands Research School for the
Socio-Economic and Natural Sciences of the Environment

C E R T I F I C A T E

The Netherlands Research School for the
Socio-Economic and Natural Sciences of the Environment
(SENSE), declares that

Hidayat

born on 16 August 1970 in Bogor, Indonesia

has successfully fulfilled all requirements of the
Educational Programme of SENSE.

Wageningen, 23 October 2013

the Chairman of the SENSE board

Prof. dr. Rik Leemans

the SENSE Director of Education

Dr. Ad van Dommelen

The SENSE Research School has been accredited by the Royal Netherlands Academy of Arts and Sciences (KNAW)

KONINKLIJKE NEDERLANDSE
AKADEMIE VAN WETENSCHAPPEN

The SENSE Research School declares that **Mr. Hidayat** has successfully fulfilled all requirements of the Educational PhD Programme of SENSE with a work load of 43 ECTS, including the following activities:

SENSE PhD Courses

- Environmental Research in Context
- Research Context Activity: Designing and developing an informative Wikipedia reference source page on the Mahakam river basin in East Kalimantan, Indonesia
- Uncertainty Analysis
- Geostatistics

Other PhD Courses

- Research Methodology I: from topic to proposal
- Techniques for Writing and Presenting Scientific Papers - by Dr. Michael Grossman
- Scientific Writing
- Mobilizing your scientific network

Management Skills Training

- Co-organizing the workshop *Tropical Delta Master Class: Anthropogenic and Natural Processes*, 24 November 2011, Jakarta, Indonesia

Oral Presentations

- *Flood mapping of middle Mahakam area using PALSAR imagery*. The second Remote Sensing Symposium (RSS), SENSE, 19 May 2010, Delft, the Netherlands
- *Combining ALOS-PALSAR imagery with field water level measurements for flood mapping of a tropical floodplain*. International Symposium on LIDAR and Radar Mapping, 26-29 May 2011, Nanjing, China
- *Discharge estimation in a backwater affected meandering river.* NCR-DAYS 2011, 27-28 October 2011, Delft, the Netherlands
- *Flood and droughts in the Mahakam lowlands: insights from radar data and a hydrological model*. World Delta Summit, 21-24 November 2011, Jakarta, Indonesia

SENSE Coordinator PhD Education

Drs. Serge Stalpers